University of Alberta

Development of an Accelerometer Based Motion Analysis System for Measurement of Head and Jaw Kinematics during Rear-Impact

by

Isaac Nasir Ikram

A thesis submitted to the Faculty of Graduate Studies and Research in partial fulfillment of the requirements for the degree of Master of Science

Department of Mechanical Engineering

Edmonton, Alberta
Fall 2004

Library and
Archives Canada

Published Heritage
Branch

395 Wellington Street
Ottawa ON K1A 0N4
Canada

Bibliothèque et
Archives Canada

Direction du
Patrimoine de l'édition

395, rue Wellington
Ottawa ON K1A 0N4
Canada

Your file Votre référence
ISBN: 0-612-95774-8
Our file Notre référence
ISBN: 0-612-95774-8

The author has granted a non-exclusive license allowing the Library and Archives Canada to reproduce, loan, distribute or sell copies of this thesis in microform, paper or electronic formats.

The author retains ownership of the copyright in this thesis. Neither the thesis nor substantial extracts from it may be printed or otherwise reproduced without the author's permission.

L'auteur a accordé une licence non exclusive permettant à la Bibliothèque et Archives Canada de reproduire, prêter, distribuer ou vendre des copies de cette thèse sous la forme de microfiche/film, de reproduction sur papier ou sur format électronique.

L'auteur conserve la propriété du droit d'auteur qui protège cette thèse. Ni la thèse ni des extraits substantiels de celle-ci ne doivent être imprimés ou aturement reproduits sans son autorisation.

In compliance with the Canadian Privacy Act some supporting forms may have been removed from this thesis.

While these forms may be included in the document page count, their removal does not represent any loss of content from the thesis.

Conformément à la loi canadienne sur la protection de la vie privée, quelques formulaires secondaires ont été enlevés de cette thèse.

Bien que ces formulaires aient inclus dans la pagination, il n'y aura aucun contenu manquant.

Canada

Acknowledgements

There are many people I owe thanks to for their help and support during the course of this work. Firstly I want to express my gratitude to my parents, Muhammed and Zenith, as well as my family. You have always encouraged and aided me in the pursuit of my dreams which I am very grateful for. Thank you to my girlfriend, Jessica Gilbert, your belief in my abilities has been, and continues to be, a constant source of encouragement. To my supervisor, Dr. Ken Fyfe, from the Department of Mechanical Engineering at the University of Alberta, thanks for giving me this opportunity and for your guidance throughout this experience. Also, during the course of this project, I was fortunate to work along side many wonderful people; to Ross Stirling, Ivonne Hernandez, Dr. Paul Major and Michelle Adrian, it was a pleasure to have met you. One person I would like to say a special thank you to is Thomas Williams. Your work ethic and brilliance is a constant inspiration to me. I appreciate all the help you have given me, but more so your friendship. Finally, to my friends Jesse Lipscombe, Greg Roy, Eric Wong and Vince Lee, thanks for your participation and help with this study.

Contents

1 Introduction and Review 1
- 1.1 Motion Analysis Systems . . . 2
  - 1.1.1 Accelerometer Based Systems . . . 2
  - 1.1.2 Reduced Computation Approaches . . . 7
  - 1.1.3 High Speed Camera Systems . . . 7
  - 1.1.4 Non-Integrating Accelerometer Systems . . . 8
  - 1.1.5 Gyroscope Based Systems . . . 9
  - 1.1.6 Combined Measurement Systems . . . 10
- 1.2 Jaw Measurement Techniques . . . 12
  - 1.2.1 Transmitter/Receiver Systems . . . 13
  - 1.2.2 Accelerometer System . . . 14
  - 1.2.3 6 Degree of Freedom System . . . 15
- 1.3 Summary . . . 16
- 1.4 Proposed Solution . . . 17

2 Equipment and Theory 19
- 2.1 Accelerometer Theory . . . 19
  - 2.1.1 Calibration . . . 20
- 2.2 Sensor Kinematics . . . 21
  - 2.2.1 Angular Acceleration . . . 22
  - 2.2.2 Translational Acceleration . . . 24
  - 2.2.3 Coordinate Transformation . . . 25
- 2.3 Data Acquisition . . . 26
  - 2.3.1 National Instruments Data Acquisition . . . 26
  - 2.3.2 dspace Data Acquisition . . . 28

3 System Uncertainty 30
- 3.1 Accelerometer Output Uncertainty . . . 30
- 3.2 Static Angle Measurement . . . 34
- 3.3 Angular Uncertainty . . . 35
  - 3.3.1 Angular Acceleration . . . 35
  - 3.3.2 Angular Velocity and Displacement . . . 36
- 3.4 Translational Uncertainty . . . 39
  - 3.4.1 Translational Acceleration . . . 39
  - 3.4.2 Translational Velocity and Displacement . . . 41

3.5 Dynamic Uncertainty 42
3.6 High-Pass Filtering 43
3.7 Differentiated Position Data 52

4 Double Pendulum Analysis **54**
4.1 Experimental Set-Up 54
4.2 Discussion/Results 56
4.2.1 2 g Angular Measurements 57
4.2.2 2 g Translational Measurements 65
4.2.3 10 g Angular Measurements 71
4.2.4 10 g Translational Measurements 77
4.3 Conclusions 81

5 Translating Pendulum Analysis **83**
5.1 Experimental Design 83
5.2 Discussion/Results 86
5.2.1 2 g Angular Measurements 87
5.2.2 2 g Translational Measurements 91
5.2.3 10 g Angular Measurements 96
5.2.4 10 g Translational Measurements 99
5.3 Conclusions 103

6 Crash Test Analysis **104**
6.1 Experimental Set-Up 104
6.2 Discussion/Results 107
6.2.1 Head and Jaw Angular Kinematics 108
6.2.2 Head and Jaw Translational Kinematics 113
6.3 Conclusions 123

7 Conclusions and Recommendations **125**
7.1 Summary 125
7.2 Conclusions and Contributions 126
7.3 Improved Performance/Future Work 127

A Additional Equipment Theory **129**
A.1 Accelerometer Theory 129
A.2 Camera Theory 130
A.2.1 Camera System Set-Up 132
A.3 Potentiometer Theory 135
A.4 Encoder Theory 136

B Filter Cut-off Selection **138**
B.1 Frequency Cut-off Analysis 138

List of Figures

1.1 A disk moving in two dimensions with two bi-axes attached, adapted from [8] . . . 3
1.2 Anatomical planes, adapted from [15] . . . 4
1.3 Becker 3-2-1 configuration, adapted from [14] . . . 5
1.4 3-2-2-2 accelerometer configuration, adapted from [18] . . . 6
1.5 Willemson relative angle technique, adapted from [32] . . . 9
1.6 Proposed solution coordinate systems, adapted from [56] . . . 17

2.1 Diagram of accelerometer operation . . . 19
2.2 Sensor board used to gather kinematic information (black squares indicate accelerometers) . . . 20
2.3 First position for calibration procedure . . . 21
2.4 Sensor board in the fixed frame . . . 22
2.5 Sensor board fixed to a rigid body . . . 24
2.6 Coordinate transformation from body fixed to global reference frame . 25
2.7 National Instruments data acquisition set-up . . . 27
2.8 dspace data acquisition set-up . . . 28

3.1 Effects of sensitive axis misalignment on acceleration measurement. γ is considered a small angle. . . . 32
3.2 Relationship between sensitive axis' of a biaxial accelerometer and the gravity vector . . . 34
3.3 Error associated with single integration of a time dependent signal . . 38
3.4 Error associated with double integration of a time dependent signal . . 39
3.5 Frequency response of a 4th-order high-pass Butterworth filter with a 0.5Hz cut-off . . . 44
3.6 Integration of an error free signal . . . 46
3.7 Integration of a signal with a DC offset . . . 47
3.8 Frequency spectrum of an integrated signal with a DC offset. . . . 48
3.9 Result of high-pass filtering the drifting signal . . . 49
3.10 Frequency sprectrum after passing the integrated data through a high-pass filter. . . . 50
3.11 Uncertainty before and after high-pass filtering . . . 51

4.1 Instrumented double pendulum . . . 55
4.2 Global coordinate system for the double pendulum . . . 56

LIST OF FIGURES

4.3 2 g Parallel accelerometer signals from the upper-link during double pendulum motion. 58
4.4 Frequency components of the upper-link's angular acceleration (2 g) . 59
4.5 Frequency components of the lower-links angular acceleration (2 g) . . 60
4.6 Angular kinematic variable comparison for the upper-link (2 g) 61
4.7 Angular kinematic variable comparison for the lower link (2 g) 62
4.8 Peak matching between accelerometer and camera derived angles for the upper-link 63
4.9 Upper-link orientation with the addition of ficticious data 64
4.10 Translational X and Y accelerations of the pendulum joint (2 g) . . . 67
4.11 Translational X and Y velocities of the pendulum joint (2 g) 68
4.12 Translational X and Y displacements of the pendulum joint (2 g) . . . 69
4.13 Translational X and Y displacements with the addition of ficticious data 70
4.14 10 g parallel accelerometer signals from upper-link during double pendulum motion 72
4.15 Frequency components of the upper-link's angular acceleration (10 g) . 73
4.16 Frequency components of the lower-link's angular acceleration (10 g) . 74
4.17 Angular kinematic variable comparison for the upper-link (10 g) . . . 75
4.18 Angular kinematic variable comparison for the lower link (10 g) 76
4.19 Translational X and Y accelerations of the pendulum joint (10 g) . . . 78
4.20 Translational X and Y velocities of the pendulum joint (10 g) 79
4.21 Translational X and Y displacements of the pendulum joint (10 g) . . 80

5.1 Fully instrumented pendulum 84
5.2 Translating pendulum test set-up 85
5.3 Translating pendulum coordinate system 86
5.4 Frequency components of the translating pendulum's angular acceleration (2 g) 88
5.5 Translating pendulum angular kinematic variable comparison (2 g) . . 89
5.6 Comparison of high pass filtering full and partial data sets 90
5.7 Translational X and Y accelerations of the extension piece (2 g) 92
5.8 Translational X and Y accelerations of the extension piece during a longer duration test (2 g) 93
5.9 Translational X and Y velocities of the extension piece (2 g) 94
5.10 Translational X and Y displacements of the extension piece (2 g) . . . 95
5.11 Frequency spectrum of translating pendulum's angular acceleration (10 g) 97
5.12 Translating pendulum angular kinematic variable comparison (10 g) . 98
5.13 Translational X and Y accelerations of the extension piece (10 g) . . . 99
5.14 Translational X and Y velocities of the extension piece (10 g) 100
5.15 Translational X and Y displacements of the extension piece (10 g) . . 101
5.16 Comparison of camera and accelerometer derived Y-displacements passed through a 4th order high pass Butterworth filter with a 0.5 Hz cut-off 102

6.1 Mouth bracket for attachment of accelerometer board and reflective markers 105
6.2 Fully instrumented subject 106

LIST OF FIGURES

6.3 Test set-up including: seat, rolling track, high speed camera system and subject . . . 106
6.4 Coordinate system for crash test experiment . . . 108
6.5 Frequency components of the head's angular acceleration . . . 109
6.6 Frequency components of the jaw's angular acceleration . . . 110
6.7 Angular kinematics of the subject's head during impact . . . 111
6.8 Angular kinematics of the subject's jaw during impact . . . 112
6.9 Translational X and Y accelerations for the subject's head . . . 114
6.10 Translational X and Y accelerations of the subject's jaw . . . 115
6.11 Translational X and Y velocities of the subject's head (high-pass Butterworth filter with 0.5 Hz cut-off) . . . 116
6.12 Translational X and Y velocities of the subject's jaw (high-pass Butterworth filter with a 0.5 Hz cut-off) . . . 117
6.13 Translational X and Y velocities of the subject's head (Fast Fourier Transform filter) . . . 118
6.14 Translational X and Y velocities of the subject's jaw (Fast Fourier Transform filter) . . . 119
6.15 Translational X and Y displacements of the subject's head . . . 121
6.16 Translational X and Y displacements of the subject's jaw . . . 122

A.1 Simplified accelerometer model . . . 129
A.2 Differential capacitor . . . 130
A.3 ProReflex MCU 240 high speed camera . . . 132
A.4 High speed camera set-up . . . 133
A.5 Calibration frame . . . 134
A.6 Calibration wand . . . 135
A.7 Potentiometer diagram . . . 135
A.8 Encoder code disk pattern and output signals . . . 137

B.1 Frequency spectrum for a raw accelerometer signal. Amplitude is in Volts. . . . 139
B.2 Residual for an accelerometer signal based on a wide range of cut-off frequencies . . . 140
B.3 Frequency spectrum for high speed camera position data . . . 141
B.4 Residual for high speed camera displacement data based on a wide range of cut-off frequencies . . . 142

List of Tables

2.1 National Instruments 6024E data aquisition card specifications 27
2.2 dspace 1104 controller board specifications 29

3.1 Angular Uncertainty During Dynamic Measurement 43
3.2 Translational Uncertainty During Dynamic Measurement 43

4.1 R and RMSE angular coefficients for upper-link (2 g) 65
4.2 R and RMSE angular coefficients for lower-link (2 g) 65
4.3 R and RMSE translational coefficients for pendulum joint (2 g) 71
4.4 R and RMSE angular coefficients for upper link (10 g) 76
4.5 R and RMSE angular coefficients for lower link (10 g) 77
4.6 R and RMSE translational coefficients for pendulum joint (10 g) . . . 80

5.1 R and RMSE angular coefficients (2 g) 91
5.2 R and RMSE translational coefficients (2 g) 95
5.3 R and RMSE angular coefficients (10 g) 98
5.4 R and RMSE translational coefficients (10 g) 102

6.1 R and RMSE angular coefficients for head and jaw 113
6.2 R and RMSE translational coefficients for the head 122
6.3 R and RMSE Translational coefficients for the jaw 123

A.1 Camera accuracy from a distance of 1m 131
A.2 Camera accuracy from a distance of 5m 131

Chapter 1

Introduction and Review

The most common injury sustained during rear-impact car accidents is whiplash. During impact, the target vehicle is accelerated forward, while the occupant remains static due to inertia. Force is then applied to the occupant's torso and shoulders from the car seats, causing them to translate while the head remains static resulting in forced extension of the neck. Following extension, the head's inertia is overcome and is accelerated forward. The neck is then forced into flexion to increase the acceleration of the head and retain its initial position. This is referred to as the whiplash mechanism.

Whiplash is the number one soft tissue injury sustained during automobile accidents. A release by the Insurance Bureau of Canada (IBC) in 2000 stated that 70% of the auto insurance claims for Atlantic Canada were due to soft tissue injury [1]. A similar result was reported by Lubin et. al. [2] where the authors found that more than half of motor vehicle accident insurance claims in Canada resulted from whiplash injuries. Although whiplash related disorders can occur in frontal or rear impacts, 85% of these disorders occur in rear impact situations [3]. Also, 65% of whiplash claims occur after low velocity impacts, [4]. Low velocity impact is defined as changes in velocity under 9 km/hr. Based on these statistics, more than half of the reported cases of whiplash resulted from low-velocity rear-impacts. Whiplash injury to the neck is often considered a significant factor for development of temporomandibular disorders (TMD) [5]. It has been speculated that during impact, the immediate hyperextension of the cervical spine causes rotation of the cranium leading to a rapid, involuntary, inverted mouth opening as the mandible remains relatively fixed while the cranium and maxilla move away ([6],[7]).

To obtain a better understanding of whiplash and related disorders, researchers have investigated ways to measure the body's kinematic response during impact. Substantial research into the development and implementation of motion analysis systems

capable of determining kinematic variables has aided this effort. Many of these motion analysis systems have stemmed from biomechanics research such as aiding people with spinal cord injuries, improving sport performance, or monitoring a patient's rehabilitation. Although these systems were originally developed for a specific purpose, the principles they are based upon can be applied to other areas. For this reason many of these systems have found other applications after their conception.

Rear impact analysis systems have typically been focussed on monitoring the kinematics of the head and torso. However, the association between whiplash and TMD [5-9], has led to interest in measuring jaw movement. In this thesis, a motion analysis system for the purpose of measuring head and jaw kinematics during low-velocity rear-impact will be presented and tested. Because the principles of this system are not solely based on research from previous crash studies, but also from other applications, the literature review was not confined to impact research.

1.1 Motion Analysis Systems

A number of different approaches have been taken in the study of motion. However, the systems developed for this purpose can mostly be grouped into two categories: optic, or sensors. Since optical systems require an unobstructed view, and are limited to measuring a pre-described volume, their use in crash test analysis requires some restrictions. Typically studies that involve the use of high speed cameras also require modification of the vehicles used, which reduces the realism of the study. Also, these systems tend to be quite expensive. Therefore, the review will primarily focus on sensor based systems; their development will be presented chronologically.

1.1.1 Accelerometer Based Systems

One of the earliest studies of the motion associated with whiplash was done with a two-dimensional accelerometer based system by Mertz [10]. Mertz showed that through specific placement of four linear accelerometers angular acceleration, angular velocity and translational acceleration of a body, which is assumed to be rigid, could be found. The accelerometers were arranged in orthogonal pairs and attached to the subject so that two axes, one from each pair, were in-line, while the other two were parallel and separated by some distance. Angular acceleration was then found by subtracting the two parallel signals and dividing by the distance between them, while angular velocity was found through integration, and translational acceleration was found by applying

the point acceleration equation. Veltink et. al. [11] used this approach to infer knee joint acceleration and quadricep torque of a freely swinging leg. Nusholtz et. al. [12] used a similar accelerometer set-up, but different mathematical approach, to measure the force deflection of an anthropomorphic test device (crash dummy) interacting with a passenger airbag. By fixing a configuration of two orthogonal accelerometer pairs on a flat disk, as shown in Figure 1.1, to the subject, Nusholtz was able to measure angular velocity directly. The disk and subject were considered to be in the same fixed frame. This was done by first determining the tangential velocity along the disk surface, which involved short duration integration of tangential acceleration to find direction, and then applying the equation $\omega = \frac{v}{r}$, where r is the radius of the disk.

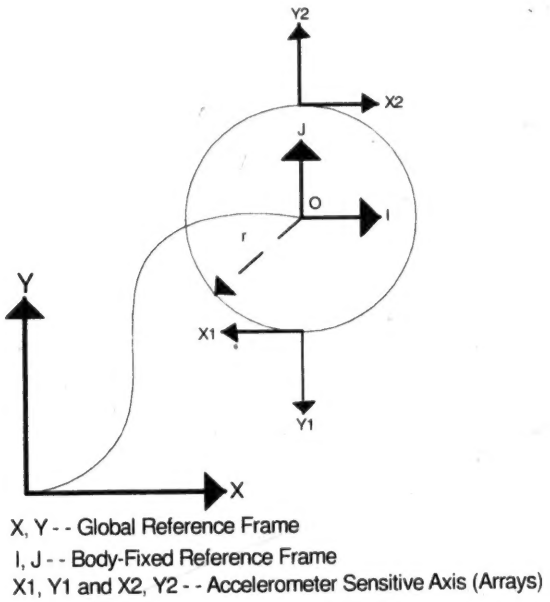

Figure 1.1: A disk translating and rotating in two dimensions with two bi-axes attached, adapted from [8]

Morris [13] extended the ideas presented by Mertz to measure the kinematics of the shank during normal human gait with a five uniaxial accelerometer configuration. translational accelerations were measured in all three planes (coronal, sagittal and transverse), while rotation was monitored in two planes (coronal and sagittal). These planes are shown in Figure 1.2. To measure transverse rotations would have required an additional accelerometer, but because this rotation was expected to be small, it was not included. All velocity and position information was found through integration, which lead to drifting of the signals with time. Morris reduced the drift problem by

assuming that the acceleration at the beginning and end of each stride was equal allowing each stride to be integrated individually over a shorter time period. Becker et. al. [14] took a similar approach to measure human response to impact acceleration. His kinematic sensors consisted of six accelerometers arranged in a T-shaped 3-2-1 configuration, as shown in Figure 1.3, where a triaxial, biaxial and uniaxial accelerometer was individually placed on the ends of the T. One of these devices was attached to a biteblock and held in the subjects mouth, while the other was attached to the first thoracic vertebrae to measure the three-dimensional response during impact.

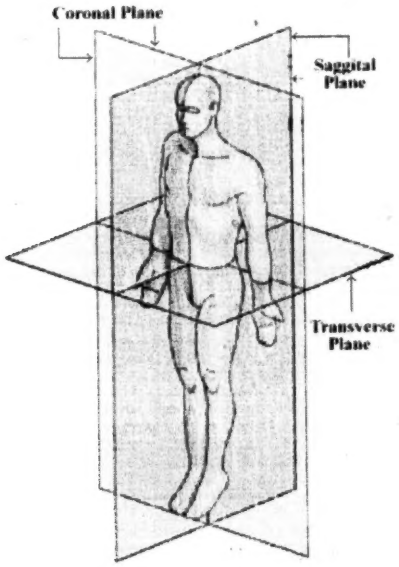

Figure 1.2: Anatomical planes, adapted from [15]

Kane et. al. [16] expanded on Morris and Becker's research by developing an accelerometer system for measuring tennis racket forces during swing. The system consisted of four triaxial accelerometers, which were placed in a non-coplanar arrangement. Through knowledge of the vectors that connect the rackets center of mass (CM) to each accelerometer, and knowing that the points are non-coplanar, the CM acceleration was determined directly from linear accelerometer measurements. Also, because four triaxial accelerometers were used, twelve acceleration equations can be formed. Solving nine of the twelve equations provides numerical values for angular velocity and angular acceleration terms. This accelerometer configuration was also used by Hayes et. al. [17] for predicting forces in the knee.

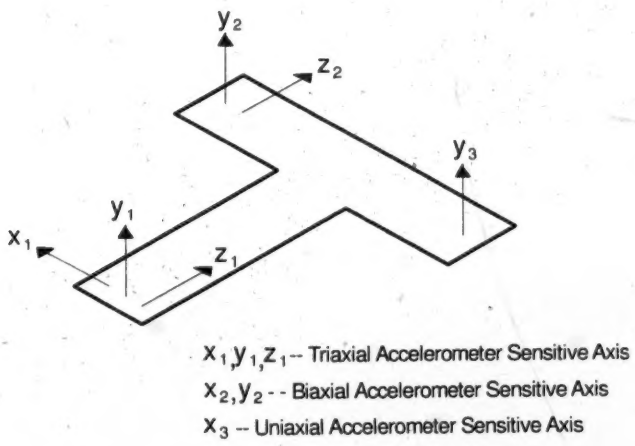

Figure 1.3: Becker 3-2-1 configuration, adapted from [14]

Another accelerometer based, six degree of freedom, motion analysis system was presented by Padgaonkar et. al [18]. The system, which is referred to as a 3-2-2-2 configuration, involves a triaxial accelerometer being placed on the chosen origin, while biaxial pairs are attached some distance away perpendicular to the sensitive axis' of the triaxial. This arrangement is shown in Figure 1.4. Padgaonkar's approach is less taxing to the data acquisition system than Kane's technique, since it only requires nine channels, but more so than the system proposed by Morris. Although full kinematic description can be achieved with six acceleration measurements, which was employed by Morris and Becker, Padgaonkar used nine in an effort to develop a more stable system. In a six accelerometer configuration, the equations formed to determine the angular acceleration vector rely on angular velocity measurements. In a practical situation, numerical integration would have to be used to obtain the necessary angular velocity terms and the resulting error would accumulate at each time step leading to inaccuracy. Liu [19] expressed similar concerns with the six accelerometer configuration. Padgaonkar's addition of three accelerometers provides enough additional information to form three new equations which, when combined with the original ones, produce expressions not dependent on angular velocity. This technique has been used in impact studies by Mital et. al. [20], Chou et. al. [21] and Cholewicki et. al. [22]. Also, Nusholtz [23] presented a slightly different nine channel accelerometer system that was used to determine the three dimensional response of an anthropomorphic dummy during impact. He attached three triaxial accelerometers, which were arranged in a spherical configuration, to a dummy and full kinematics description was achieved. This system was an extension of his two-dimensional model discussed earlier.

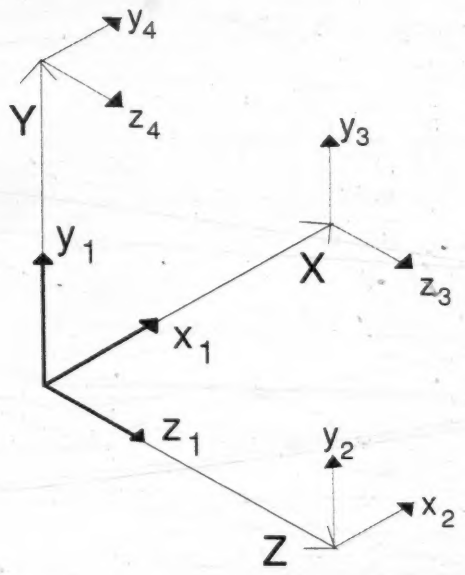

Figure 1.4: 3-2-2-2 accelerometer configuration, adapted from [18]

Although the 3-2-2-2 system does eliminate the coupling and non-linear portions from the 6 accelerometer configuration, the structural arrangement of the sensors can lead to vibrational error during impact. Direct impact causes vibration of the body and since the accelerometers, which are attached to the body, are sensitive to vibration, this increases measurement error. An alternate accelerometer approach aimed at solving this problem was presented by Viano et. al. [24] in a study involving direct impact to the head of an anthropomorphic dummy. This technique, referred to as in-line accelerometry, involves measuring the translational acceleration of a point on the head with three uniaxial accelerometers, while the difference in translational acceleration at multiple points along the three body fixed axes are taken. Statistical methods, such as linear regression, are then used on the rows of accelerometers to determine the acceleration gradients along the axes. This technique can minimize effects of accelerometer noise for the determination of angular acceleration during severe impacts. Shea et. al. [25] used a two dimensional in-line approach to measure body segment trajectories of a hybrid III dummy during frontal impact.

1.1.2 Reduced Computation Approaches

Through application of Becker's, Kane's, Padgaonkar's and Viano's techniques, all kinematic variables can be derived. A more simplistic procedure for motion analysis, where full kinematic description may not be needed, was presented by Smidt et. al. [26]. A system consisting of a single triaxial accelerometer and foot switches was used to measure gait of subjects with tibio-femoral knee implants. The accelerometer was placed on the subjects belt with the three axes being parallel to the transverse, coronal and sagittal planes of the body. Footswitches were used to determine when heel-strike, foot-flat, heel-off, and toe-off occurred and these phases were correlated with acceleration signals. Lafortune [27] also used a single triaxial accelerometer in a separate biomechanics study. Accelerations, along the three orthogonal axis of the tibia, were measured by inserting a pin, which had an accelerometer attached to it, into a healthy subjects tibia. Although accurate results were achieved with this technique, its invasive nature makes it infeasible for widespread use. Kumar et. al. [28] measured acceleration of a subject during low velocity frontal impacts with two triaxial accelerometers where one was placed on the subjects forehead, while the other was placed on the spine (in-line with the shoulder). This system is limited to body fixed translational measurements, which is adequate for applications where little rotation is expected, but not commonly used in crash studies.

1.1.3 High Speed Camera Systems

Angeles [29] took a different approach to the problem of full kinematic description. While the accelerometer based solutions rely on obtaining kinematic information relative to a body fixed frame then transforming it to the inertial frame, Angeles solution is solved entirely in the inertial frame. A mathematical approach for computing rigid body angular acceleration from point acceleration measurements is presented. Angeles' model relies on knowing the position, velocity, and acceleration vectors of three body fixed non-collinear points in the inertial frame. Although his solution is mathematically sound, a method for determining kinematics in the inertial reference frame, such as a high speed camera system, would be necessary to produce the required variables. Yogandan et. al. [30] used high speed cameras to measure the kinematic response of intact head and neck structures, which were obtained from cadavers, during whiplash-like perturbations. In his study only translational and angular displacements were analyzed which eliminated the need for any differentiation or filtering of the data.

Both accelerometer and camera based systems are capable of producing full kine-

matic description, but in both cases mathematical manipulation is involved. A comparison between the two systems was performed by Ladin et. al. [31] where the advantages and disadvantages of each system for the purpose of dynamic measurement were studied. An electromechanical device, which produced pure sine wave kinematics in the range of 1-11 Hz, was used to test the performance of the different systems. Amplitude, offset and noise were the basis of comparison used by the authors. The positional data was differentiated to find the other kinematic parameters, while the acceleration data was numerically integrated. When the camera data was differentiated the high frequency noise present in the signal was amplified. This was not a problem at low frequencies because the application of a low-pass filter with a low cut-off would clean up the signal. However, during higher frequency motion a low cut-off would cause underestimation of the amplitude, while a high cut-off would not remove the noise. The noise in the accelerometer signal was found to be directly proportional to the vibration of the system. Despite this fact, the accelerometer based system produced a signal to noise ratio (SNR) that was, on average, 4-5 times larger than what was seen with the camera system when measuring acceleration. One problem that occurred with the accelerometers that was not seen in the other system was drift. When the accelerometer signals were integrated they tended to drift with time, which necessitated the use of a high-pass filter. Although both systems have their limitations, position measurement systems seem to be more suited to low frequency applications, while accelerometry is better suited for high frequency applications.

1.1.4 Non-Integrating Accelerometer Systems

The drifting associated with integration of accelerometer signals has imposed limitations on the sensor's use for positional measurement. Willemson et. al. [32] took steps toward a possible solution to this problem by presenting an accelerometer based system capable of measuring relative joint angles. The solution is based on two rigid bodies connected by a hinge joint moving in two dimensions. To find the relative angle, two collinear accelerometer pairs were placed on each body some fixed distance apart. Since both bodies share a common point, the hinge, the output from the accelerometers on either body can be used to find the acceleration of the hinge in body fixed coordinates. When the relative angle between the two bodies is zero, the hinge acceleration determined in either reference frame should be the same. When the bodies rotate relative to each other, the difference in the measured hinge acceleration will be proportional to the angle between the bodies. This relationship is shown in Figure 1.5. Willemson applied this system to measure knee angles during shank pendulum movement, standing up, sitting down and walking.

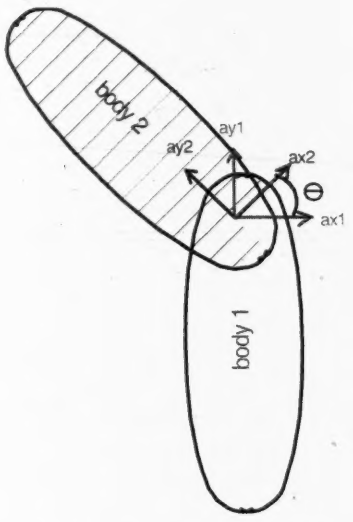

Figure 1.5: Willemson relative angle technique, adapted from [32]

1.1.5 Gyroscope Based Systems

Although Willemson was able to eliminate the need for integration, his solution is limited to measuring the relative angle between bodies. For some applications this is adequate, but for others, knowing the absolute positions of the bodies is necessary. As discussed earlier, accelerometer systems require double integration to obtain this information, and while camera systems measure this directly, they are confined to monitoring a bounded volume and require an unobstructed view. Another type of sensor with motion analysis capabilities is the gyroscope. A typical gyroscope consists of a vibrating structure in a rotating reference frame (assume vibration along X-axis). When rotation occurs about the z-axis, the Coriolis force generated causes additional vibration perpendicular to the axis of rotation (Y-axis). The resulting vibration is proportional to the rate of turn, which is the angular velocity. Since gyroscopes directly measure angular velocity, positional information can be determined by single, as opposed to double integration. Although this re-introduces a similar problem encountered with the accelerometers, the drift associated with double integration is much more pronounced than it is from single integration. Tong et. al. [33] developed a gyroscope based motion analysis system for the purpose of gait measurement. The

system was composed of two uniaxial gyroscopes, one on the thigh and one on the shank, also, four force sensitive resistors (FSR) were placed on the bottom of the foot. Output from the FSR's was used to determine the different phases of gait based on foot contact forces. The data obtained during walking tests was verified with an optical motion analysis system. Comparison between the systems was done by computing the correlation coefficient (R), and the root mean square error (RMSE). The correlation coefficient, denoted as R, is a statistic to measure the extent to which variations in one variable are related to variations in another. The value of R varies between -1 and +1, with +1 or -1 indicating a perfectly linear relationship between the variables, and 0 indicating no relationship. 'R' corresponds to the slope of the regression line when both variables have been converted to z-scores, and plotted in a scatterplot. The correlation coefficient is defined as

$$R = \frac{\sum_{i=1}^{N} Z_X Z_Y}{N-1} \tag{1.1}$$

where Z_X and Z_Y are the z-scores, and N is the number of points. The root mean square error (RMSE) is used when looking for differences between subgroups or for relationships between variables. Essentially it is the standard deviation of the difference between two parameters. This gives a good idea of the average difference between the variables being compared. The root mean square error is defined as

$$RMSE = \sqrt{\frac{\sum_{i=1}^{N} (X_i - Y_i)^2}{N-1}} \tag{1.2}$$

where X and Y refer to the variables being compared. The two systems compared produced similar results demonstrated by a correlation coefficient (R) close to 1, and root mean square error (RMSE) close to 0 (this is based on high-pass filtered positional data). One problem encountered with the gyroscopes, that was not seen with the other systems, is drifting when the subjects changed direction. This was most likely caused by the leg segment being inclined during the turn, and was removed by resetting the leg angle to 0 degrees at the end of each stride.

1.1.6 Combined Measurement Systems

All the systems discussed thus far are either not capable of independently producing a full kinematic description, or require either integration or differentiation in order to do so. Accelerometers, high speed cameras, and gyroscopes each measure a different kinematic variable directly, while numerical techniques are used to determine all other kinematic information. Since integration and differentiation can lead to large uncertainties, it seems desirable to combine the systems and increase the number of

variables that can be measured directly, thus, reducing the overall uncertainty. This mode of thinking led to Ladin et. al. [34] to combine accelerometer and position measurements for the purpose of joint force measurement. In this study the authors presented a method that combines the best aspects of both systems. Acceleration is measured by a triaxial accelerometer, while the position and orientation data is obtained from a high speed camera system. A two degree of freedom pendulum, which was instrumented with strain gauges, was used to evaluate this system. The accelerometer was placed at the pendulum's center of mass and light emitting diodes were attached to the link. A transformation matrix, which was used to remove the gravity component from the accelerometer signals, was obtained from camera output. Joint forces, derived from transformed accelerometer output and from differentiated camera data, were compared to the results from the strain gauges. As expected, the joint force estimation from the combined system produced better results than either of the motion analysis systems on their own. This approach was taken by McConnell et. al. [35] to measure head, neck and trunk kinematics during low velocity motor collisions. A biteblock, which had a triaxial accelerometer assembly fixed to it, was placed in the subjects mouth, while high speed cameras were stationed in several locations around the test area for photographic documentation.

Although Ladin's method worked relatively well, it is limited to applications with an established volume. Heyn et. al. [36] proposed a different approach based entirely on sensors. By combining accelerometers and gyroscopes, the authors were able to directly measure more kinematic variables than traditional techniques, but were not limited by volume. The system was designed to measure the swing phase of gait, which is assumed to primarily occur in two dimensions. This assumption reduces the number of required sensors, the complexity of the problem, and computational time. Heyn's system consisted of two lightweight aluminum strips outfitted with four uniaxial accelerometers, placed in pairs, and a rate gyroscope. translational acceleration, angular acceleration and angular velocity were measured directly, while the relative joint angle was calculated using the Willemson et. al. approach. Positions/orientations of the shank and thigh were derived from length measurements and integrated gyroscope output. A high speed camera system was used during the tests for verification of position measurements, and correlation was quantified by determining the correlation coefficient (R) and normalized root mean square error (NRMSE) between the signals. In this case R was close to 1 (0.995), and NRMSE was close to 0 (0.054), which indicates a high correlation. A similar system was used by Mayagoitia et. al. [37] in a separate gait study.

The systems developed by Ladin and Heyn do have lower uncertainty than non-

combination systems, but still involve some mathematical manipulation and filtering. When filtering is applied to a signal the frequency range of the system is reduced, which limits it to certain applications. Wu et. al. [38] developed the Integrated Kinematic Sensor (IKS) with the focus being kinematic description of a bodies center of mass over a large frequency range. By developing a system capable of measuring all important kinematic parameters directly, the use of integration, differentiation, high and low pass filtering is not necessary, thus, frequency range is maximized. The IKS is composed of a triaxial accelerometer, a triaxial angular rate sensor, and multiple markers for measurement of segmental position. Design of the IKS was based on an analysis that showed direct measure of position, angular velocity and translational acceleration resulted in the least error for determining the center of mass acceleration. This sensor was applied to a walking study, where an IKS was placed on the foot, shin and thigh and the subjects were asked to walk and run. A comparison between results from this study and those obtained by other researchers showed general agreement. A similar approach was taken by McConnell et. al. [39] to measure head and neck kinematics during low velocity rear-end impacts. In this study a biteblock, which was instrumented with a triaxial linear accelerometer as well as a triaxial angular accelerometer, was placed in the mouth of the subject, while high speed cameras, which were stationed in several locations around the test site, provided photographic documentation. Sigmund et. al. [40],[41] also took this approach in two separate studies where the subject's kinematic response to whiplash-like perturbations during aware and unaware situations was monitored. Since the motion of interest to the researcher was expected to be primarily planar, two-dimensional analysis was deemed adequate. Two linear accelerometers and an angular rate sensor were fixed to the subjects forehead, while markers, which were tracked by high-speed cameras, were attached to the forehead and neck/spine area to obtain kinematic data.

1.2 Jaw Measurement Techniques

There are a number of different techniques available for measuring jaw position. For the most part, these systems work by attaching a transmitter to a mandibular tooth, while a receiver is, in some way, fixed to the head. The output from the transmitter is recorded by the receiver and, based on some calibration procedure, converted to a jaw displacement. A review of jaw measurement devices will now be presented in chronological order.

1.2.1 Transmitter/Receiver Systems

Hannam et. al. [42] assessed the feasibility of using a kinesiograph for measuring jaw displacement. A kinesiograph uses magnetometers to sense the position of a magnet, which is cemented to the lower anterior teeth, in three orthogonal planes. There are three main problems associated with the kinesiograph: it is only capable of measuring the three translational degrees of freedom, the output is non-linear for the entire range of functional jaw movement, and it requires reference to fixed cranial landmarks (magnetometers). Since the most significant measurement during the majority of jaw reflex studies is the mandible position relative to the maxilla, the systems restriction to translational measurement is not a significant deterrent. However, the problems associated with non-linearity and fixed reference points are more difficult to solve. Typically error resulting from non-linearity is reduced through calibration, which means the accuracy of the system relies on the calibration procedure. To ensure cranial landmarks remain fixed they are attached to a rigid structure, commonly referred to as a head bracket, which is worn by the subject. Because any rotation of the landmarks with respect to the magnet will cause errors, the head is kept still during measurement. Hannam concludes that a kinesiograph can be used in jaw reflex studies provided adequate calibration is performed prior to measurement and the head bracket system remains fixed. The kinesiograph was used in a study by Plesh et. al. [43] to measure 3-D movement trajectory and velocity profiles during chewing.

In a study by Miles et. al. [44] the relationship between jaw closing movement and the timing of muscle activity was investigated. Because how open or closed the jaw is can be assessed by a single parameter, which is vertical displacement, Miles employed a single degree of freedom system. Jaw movement was monitored by cementing a small light to the subjects lower incisor, which activated a photosensitive position detector. The velocity and acceleration associated with the movement was found through differentiation of the positional data. A similar approach was used by Luschei and Goodwin [45] to monitor mandibular patterns during mastication by monkeys.

A linear variable differential transformer (LVDT) was used by Ostry et. al. [46] to measure movement amplitudes and maximum velocities during mastication and speech. The LVDT was composed of a lightweight circular transformer and a metallic core. A modified hockey helmet, with the transformer attached, was worn by the subject. One end of the core was fixed to the subjects chin while the other end was placed inside the transformer so that movement of the jaw would induce a linear change in voltage. This system is similar to the one used by Miles in that only the principal direction of jaw movement is monitored. One extra caution involved in the

LVDT set-up is the diameter of the core. The core diameter must be sufficiently sized to prevent contact with the transformer walls, which would prevent normal jaw movement. LVDT's have been shown to be very accurate for measure of translational displacements, but they tend to be expensive.

Wilding et al. [47] used a sirognathograph to analyze human jaw movement during mastication. A sirognathograph consists of a head set, which has a number of hall effect sensors mounted on it, and a computing unit. The system works by passing current through the sensors and measuring the voltage produced by the presence of a magnetic field. A magnet, which is fixed to a subjects lower anterior teeth, creates the magnetic field and its position is monitored by the hall effect system. The induced voltages are sent to the computing unit, which segregates the signals, and converts them to three-dimensional positions. Although this system relies on measuring magnetic field, similar to a kinesiograph which showed linearity problems, Wilding points out that a sirognathograph is accurate to within 1% of actual jaw movement. This result was based on a studies by Hannam et. al [42] and Mongini [48]. However, because the sensors are used as landmarks for the system, they must remain fixed in their initial positions. This limits the use of the system to applications where the head can be constrained during measurement. A separate study by Agrawal et. al. [49] involved the use of a sirognathograph to determine the effects of food fragmentation on the mandibular closing angle.

1.2.2 Accelerometer System

The systems that have been presented thus far have been based on attaching some form of marker to a mandibular tooth, while a separate sensor is attached to the head. Many of these systems are bulky, expensive, or require the head to be constrained during measurement. Flavel et. al. [50] presented a method for measuring vertical displacement of the jaw, which is cheap, non-intrusive, and simple. Although it is incapable of doing 3-D analysis, the jaw movement of most interest to researchers studying the jaw is vertical displacement. The following studies were cited by the authors as examples: Hannam et. al., [51]; Miles and Wilkinson, [44]; Miles et. al., [52]; Wang et. al., [53]. Flavel's system consisted of two uniaxial accelerometers and a Hall effect sensor. Each accelerometer was mounted on a lightweight bracket made of lead-free and resin-free solder wire, which was glued to the upper and lower incisors of the subject. The hall effect magnet was attached to the upper bracket, while the sensor was attached to the lower bracket. Verification of the system was done by mounting the devices on an apparatus used in jaw reflex studies and moving the transducers

known distances, relative to each other, at known angular accelerations under servo control. The results from these test showed Flavel's system agreed well with output obtained from an LVDT over an acceleration range of 0.5 - 40 $\frac{m}{s^2}$. Dynamic position, which refers to the opening and closing of the mouth, was found through double integration of the acceleration signals, while initial conditions were determined from static measurements with the Hall effect sensor. Although the system presented is not hindered by the majority of problems associated with other jaw motion measurement devices, it can only be used to measure vertical displacement during the rotational part of jaw motion. Full jaw motion, which includes rotation and translation, cannot be measured with this system.

1.2.3 6 Degree of Freedom System

As mentioned earlier, the motion of most interest to researchers studying jaw reflexes has been vertical jaw displacement. However, the need for a full six degree of freedom system still exists. Leader et. al. [54] presented a method for full kinematic description of the jaw that is easy to understand by the clinicians who would use it, while still being mathematically rigorous. To do this, subjects were required to wear a customized dental clutch, which was designed not to inhibit natural jaw movement, and a reference cap. Seven reflective spheres, including three non-collinear motion markers and four non-collinear magnetic resonance imaging markers, were attached to the clutch, while three non-collinear reflectors were attached to the reference cap. A high speed camera system, which was shown to be linear and reliable across three series of 0.10 mm incremental movements with a surgical micrometer, was used to gather positional information for all six degrees of freedom. Registration of the three-dimensional geometric model of the jaw, which was generated from MRI images, and kinematic data involved the use of three transformation matrices. A non-orthogonal floating axis system was used to derive a relationship between jaw and head movement. This system was able to fully describe mandibular motion. In a separate study by Wagner et. al. [55], jaw measurement by high speed cameras was compared to a Cadiax system, which is a caliper-like device for measuring the relationship between the jaws and temporomandibular joints. Based on confidence intervals found from comparing the camera measurements to the more commonly used Cadiax, the optoelectronic system was shown to be adequate.

1.3 Summary

Although some of the systems that were discussed measure in three-dimensions, a two-dimensional system should be adequate for measurement of movement during rear-impact. This is because the force applied during rear-impact is nearly planar, and thus, it is reasonable to assume the majority of the resulting motion will also be planar. A review of results obtained from rear-impact studies using three-dimensional motion analysis systems, [5, 9, 10, 11, 14], showed that the magnitude of motion was much larger within the plane than outside it. Therefore, a two-dimensional system for our application is justified. Because high speed cameras require a predefined volume and an unrestricted view of the subject, which may not be the case during rear-impact, a sensor based motion analysis system would appear to be the best choice. Gyroscopes will not be incorporated into the system because they tend to be more expensive than accelerometers, and the angular velocities experienced during impact are expected to exceed the range of the average gyroscope (above $3.14\frac{rad}{s}$). Also, improved accelerometer technology, and adequate calibration will decrease the uncertainty in direct acceleration measurements and could reduce the problems associated with integration to an acceptable level.

The majority of jaw studies reviewed were focused on measuring sagittal plane motion with the main interest being position of the mandible relative to the maxilla or, in more general terms, how open the mouth is. Because this seems to be the primary focus of jaw researchers, it makes sense that persons investigating jaw movement during rear-impact will be mostly interested in the same thing, thus, a two dimensional system was deemed adequate for this application. Most systems used to measure jaw movement tend to be bulky and require the head to be stationary during measurement. This is normally not a problem since most jaw studies are performed in a clinical atmosphere. However, because the head moves a substantial amount during impact, the majority of these systems cannot be used in a whiplash simulation study. The accelerometer based system, which was developed by Flavel, was shown to accurately measure vertical jaw displacement when compared with more accepted and expensive systems during the rotation phase of movement. Therefore, an accelerometer based system should be capable of measuring jaw displacement with suitable accuracy for clinicians. The system developed in this thesis will use the same base sensor, but is not limited to measuring the rotation phase. Additional accelerometers will be added so that angular acceleration, velocity and displacement can be determined. By combining this with the information gathered from the head, the relative angles can be determined, and the openness of the mouth inferred. Although Willemson's technique allows direct computation of relative angles, it relies on modelling the joint between

the bodies as a hinge, which is not a realistic assumption for the jaw.

1.4 Proposed Solution

To measure head and jaw accelerations, during low-speed rear impact, a two-dimensional system consisting of four biaxial accelerometers will be used. The head and jaw coordinate systems are shown in Figure 1.6. The accelerometers are arranged in a similar way to Mertz and Veltink where two axis, one from each biaxial, are in-line while the other axis' are parallel and separated by some distance. Two-dimensional kinematic description is obtained by attaching one biaxial pair to the head, while the other is attached to the jaw, during impact. Since the system is only capable of measuring translational and angular acceleration directly, other kinematic parameters will have to be determined through mathematical manipulation.

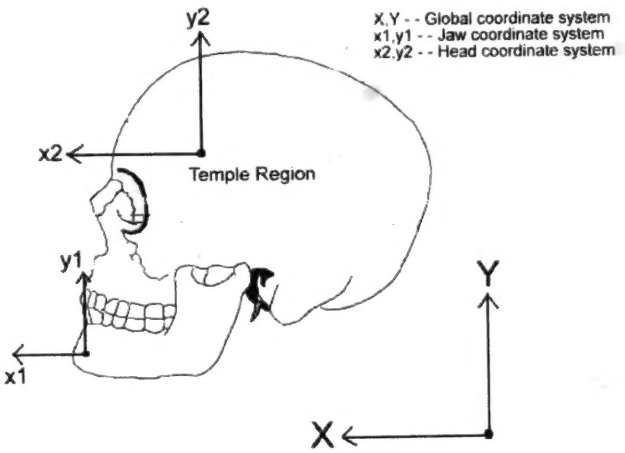

Figure 1.6: Proposed solution coordinate systems, adapted from [56]

This thesis will be organized in the following way: Chapter 2 will focus on the equipment and theory that relates to every experiment, while specific equipment, or theory, pertaining to individual experiments will be discussed separately. Chapter 3 provides uncertainty analysis for accelerometer derived angular and translational kinematics. Chapter 4 presents the results from pure rotation measurement, involving the use of a double pendulum. Chapter 5 presents the result for measurement of translating and rotating movement, which was done by suspending a single pendulum from a translating cart. Chapter 6 presents the results from an actual crash test, where the accelerometer system was used to measure head and jaw movement during

simulated rear-impact. Finally, Chapter 7 gives an overview of the system's overall performance, and ideas for improvement.

Chapter 2

Equipment and Theory

In the previous chapter, motion analysis systems were reviewed and a system for our application was proposed. In this chapter, we will discuss the equipment and theory that was employed in the development of the system. Theory and calibration of accelerometers will be covered first. Next, the mathematical operations for determination of body kinematics from accelerometer output will be shown. Finally, specifications of the data acquisition system used to gather sensor information will be discussed.

2.1 Accelerometer Theory

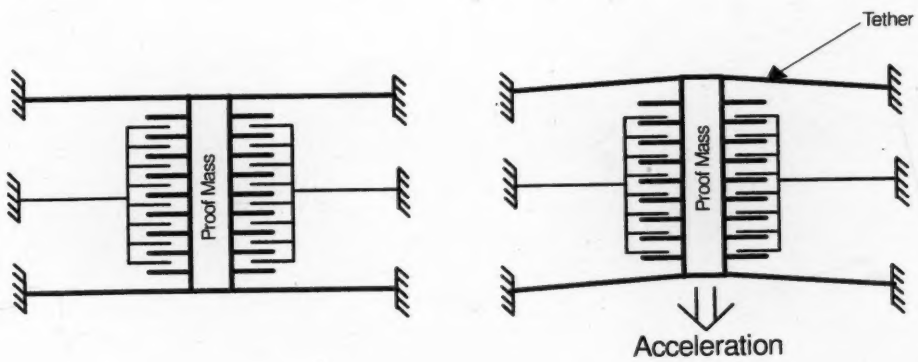

Figure 2.1: Diagram of accelerometer operation

Figure 2.1 shows a simplified diagram of how an Analog Devices micro-machined ADXL series accelerometer works. When the sensor undergoes acceleration, the inertia of the mass causes deflection in the opposite direction, and the capacitance changes

accordingly. Since excessive flexing of the tethers leads to non-linearity, voltage is applied to keep the mass relatively still. Figure 2.2 shows the accelerometer board that was used in this work.

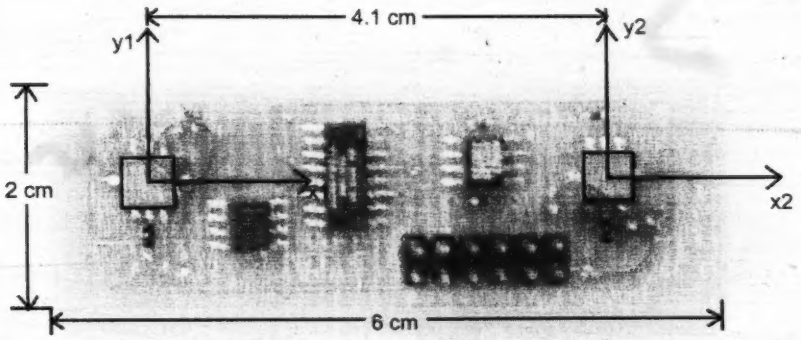

Figure 2.2: Sensor board used to gather kinematic information (black squares indicate accelerometers)

2.1.1 Calibration

Calibration of the ADXL 210's (10 g range) and 202's (2 g range) were calibrated by measuring the gravity vector. The accelerometers are components on multi-purpose sensor boards. To begin calibration, the sensor board is bolted to the calibration block and placed so that, based on a right handed coordinate system, the x and y axis of accelerometer 1 point in the positive direction. This initial set-up can be seen in Figure 2.3.

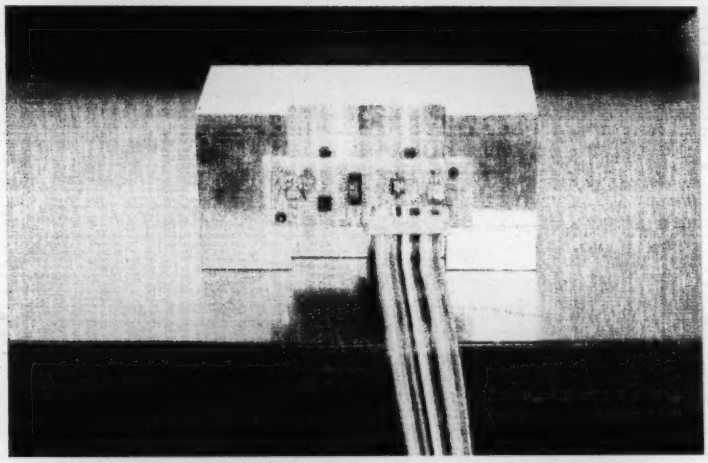

Figure 2.3: First position for calibration procedure

The block is then rotated 270 deg in 90 deg increments to obtain data in four different positions. In two of the positions the accelerometers will measure gravity, while in the other two positions they will measure a 0 $\frac{m}{s^2}$ acceleration. The NullLevel, which is defined as the voltage corresponding to an acceleration of 0 $\frac{m}{s^2}$, is found by taking the mean of the output recorded at 0 g's. To find the Sensitivity, which is the change in voltage when the sensitive axis is measuring gravity, the mean of the output at +1 g is subtracted from the mean of the output at -1g and that number is divided by 2. Expressions for NullLevel and Sensitivity are shown below

$$
\begin{aligned}
NullLevel_{x-axis} &= mean(Xoutput_{position(1)} + Xoutput_{position(3)}) \qquad (2.1)\\
NullLevel_{y-axis} &= mean(Youtput_{position(2)} + Youtput_{position(4)})\\
Sensitivity_{x-axis} &= \frac{mean(Xoutput_{position(2)}) - mean(Xoutput_{position(4)})}{2}\\
Sensitivity_{y-axis} &= \frac{mean(Youtput_{position(1)}) - mean(Youtput_{position(3)})}{2}
\end{aligned}
$$

where $Xoutput$ and $Youtput$ refer to the voltages recorded along the axis shown in Figure 2.2. NullLevels are reported in $Volts$ while Sensitivities are reported in $\frac{Volts}{gravity}$.

2.2 Sensor Kinematics

In this section, a mathematical description for the determination of a rigid body's angular acceleration, based on measurements from two collinear and coplanar accelerom-

eters, will be given. Also, a method for determining the translational acceleration of a point on a rigid body, and the coordinate transformation employed to convert body fixed kinematics to the global reference frame will be shown. We start off with angular acceleration theory.

2.2.1 Angular Acceleration

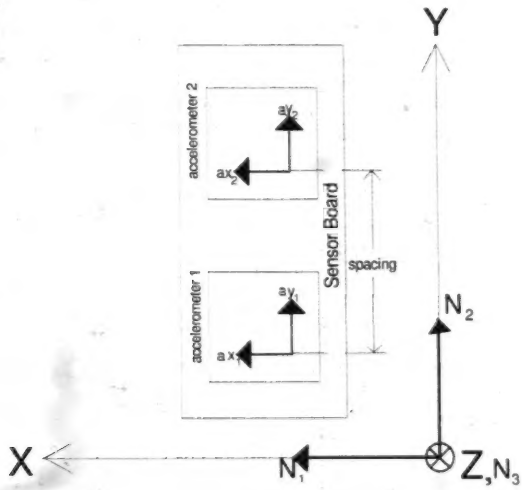

Figure 2.4: Sensor board in the fixed frame

Figure 2.4 shows the accelerometer configuration that will be employed in this study. The sensor board, which we will refer to as a rigid body, is fixed in the N_1, N_2, N_3 frame and a_{x1},a_{y1},a_{x2}, a_{y2} refer to accelerometer outputs. X, Y, Z refers to the global reference frame. We begin by defining the relative acceleration equation for two points on a rigid body as

$$\vec{a}_2 = \vec{a}_1 + \vec{\alpha} \times \vec{r} + \vec{\omega} \times (\vec{\omega} \times \vec{r}) \tag{2.2}$$

where $\vec{\alpha}$ and $\vec{\omega}$ refer to the angular acceleration and velocity vectors for the body, $\vec{a}_1$ is a known acceleration vector at a point on the body, $\vec{a}_2$ is the acceleration vector we are interested in, and $\vec{r}$ is the vector from the point of known acceleration to the point of unknown acceleration. We will define a set of orthogonal unit vectors, based on a right handed system, in the body fixed reference frame as

$$[\mathbf{N}] = \{\vec{n}_1, \vec{n}_2, \vec{n}_3\} \tag{2.3}$$

and a set of orthogonal unit vectors, based on a right handed system, in the global reference frame as

$$[\mathbf{M}] = \{\vec{x}, \vec{y}, \vec{z}\}. \tag{2.4}$$

Then, to complete the derivation, we define the following variables:

$$\vec{a}_{1/N} = A_1\vec{n}_1 + B_1\vec{n}_2 + C_1\vec{n}_3 \tag{2.5}$$

$$\vec{a}_{2/N} = A_2\vec{n}_1 + B_2\vec{n}_2 + C_2\vec{n}_3 \tag{2.6}$$

$$\vec{r}_N = a\vec{n}_1 + b\vec{n}_2 + c\vec{n}_3 \tag{2.7}$$

$$\vec{\alpha}_N = \alpha_1\vec{n}_1 + \alpha_2\vec{n}_2 + \alpha_3\vec{n}_3 \tag{2.8}$$

$$\vec{\omega}_N = \omega_1\vec{n}_1 + \omega_2\vec{n}_2 + \omega_3\vec{n}_3 \tag{2.9}$$

Now Equation 2.2 can be re-written as

$$A_2\vec{n}_1 + B_2\vec{n}_2 + C_2\vec{n}_3 = A_1\vec{n}_1 + B_1\vec{n}_2 + C_1\vec{n}_3 + \begin{bmatrix} \alpha_1 & \alpha_2 & \alpha_3 \\ a & b & c \end{bmatrix} + \vec{\omega}_N \times \begin{bmatrix} \omega_1 & \omega_2 & \omega_3 \\ a & b & c \end{bmatrix}, \tag{2.10}$$

or in expanded form

$$\begin{aligned}(A_2 - A_1)\,\vec{n}_1 + (B_2 - B_1)\,\vec{n}_2 + (C_2 - C_1)\,\vec{n}_3 \;=\; & (\alpha_2 c - \alpha_3 b)\vec{n}_1 - (\alpha_1 c - \alpha_3 a)\vec{n}_2 + (\alpha_1 b - \alpha_2 a)\vec{n}_3 \\ & +(\omega_2(\omega_1 b - \omega_2 a) - \omega_3(-\omega_1 c + \omega_3 a))\vec{n}_1 \\ & -(\omega_1(\omega_1 b - \omega_2 a) - \omega_3(\omega_2 c - \omega_3 b))\vec{n}_2 \\ & +(\omega_1(-\omega_1 c + \omega_3 a) - \omega_2(\omega_2 c - \omega_3 b))\vec{n}_3.\end{aligned}$$

However, if we assume planar motion and that $\vec{a}_1$ and $\vec{a}_2$ are the acceleration vectors at the points where the accelerometers are located, $C_2, C_1, a, c, \alpha_1, \alpha_2, \omega_1, \omega_2 = 0$ and Equation 2.8 simplifies to

$$(A_2 - A_1)\,\vec{n}_1 + (B_2 - B_1)\,\vec{n}_2 = -\alpha_3 b\vec{n}_1 - \omega_3^2 b\vec{n}_2. \tag{2.11}$$

Therefore angular acceleration for the body is determined from

$$\alpha_3 = \frac{A_1 - A_2}{b} \tag{2.12}$$

where A_1 and A_2 are the outputs from accelerometers 1 and 2 in the $\vec{n}_1$ direction. Also, the square of the angular velocity can be found from

$$\omega_3^2 = \frac{B_1 - B_2}{b} \tag{2.13}$$

Since this term is squared, direction cannot be determined from this expression.

2.2.2 Translational Acceleration

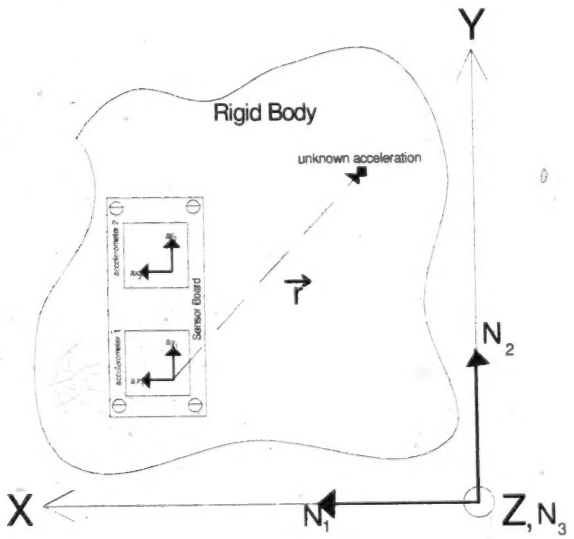

Figure 2.5: Sensor board fixed to a rigid body

In this study, determination of the translational kinematics at points on a rigid body where accelerometers cannot be directly attached is required. This can be achieved by fixing a sensor board to the body as shown in Figure 2.5. We start with Equation 2.2

$$\vec{a}_2 = \vec{a}_1 + \vec{\alpha} \times \vec{r} + \vec{\omega} \times (\vec{\omega} \times \vec{r}),$$

which becomes

$$a_{2/N} = A_1\vec{n}_1 + B_1\vec{n}_2 + \alpha_3(-b\vec{n}_1 + a\vec{n}_2) - \omega_3^2(a\vec{n}_1 + b\vec{n}_2) \tag{2.14}$$

for the 2-D case expressed in the [**N**] frame, since $B_1, C_1, \alpha_2, \alpha_1, \omega_2, \omega_1$ *and* c all equal 0. In order to solve this equation, knowledge of the bodies angular acceleration, (angular velocity)^2 as well as the acceleration at a fixed point on the body, and the vector from the point of known acceleration to the point of interest is required. In the previous section we showed that the angular acceleration of the sensor board can be determined from

$$\alpha_3 = \frac{A_1 - A_2}{b}$$

based on rigid body kinematics. Because the board is fixed to the rigid body, which means no relative motion occurs, their angular accelerations will be the same. These angular accelerations will be passed through a trapezoidal integrator to obtain angular velocities, and the output from accelerometer 1 will be considered the known point of acceleration. The a and b components of the vector $\vec{r}$ can be found through direct measurement. The values are substituted into Equation 2.12 to obtain the translational acceleration vector at the point of interest. Determination of translational velocity and displacement is achieved with trapezoidal integration. A trapezoidal integrator was selected since it can be performed with a simple algorithm, and delivers high accuracy.

2.2.3 Coordinate Transformation

Since in the previous section we defined angular and translational kinematics in the body fixed frame, while we are interested in global measurements, a coordinate transformation is required. Figure 2.6 shows graphically the relationship between the body fixed and global coordinate systems.

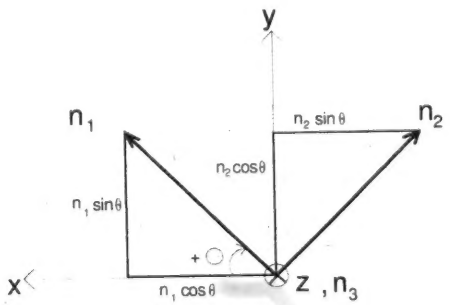

Figure 2.6: Coordinate transformation from body fixed to global reference frame

The following rotation matrix is employed in the coordinate transformation:

$$\begin{bmatrix} \vec{x} \\ \vec{y} \\ \vec{z} \end{bmatrix} = \begin{bmatrix} \cos\theta & -\sin\theta & 0 \\ \sin\theta & \cos\theta & 0 \\ 0 & 0 & 1 \end{bmatrix} \begin{bmatrix} \vec{n}_1 \\ \vec{n}_2 \\ \vec{n}_3 \end{bmatrix}$$

2.3 Data Acquisition

Two different data acquisition systems will be used in this thesis. Double pendulum and crash test data will be recorded with a National Instruments 6024E data acquisition (DAQ) card while translating pendulum data will be collected with a dspace 1104 R&D controller board. Although the National Instruments system could be used for all experiments, the translating pendulum apparatus incorporates its own data acquisition which the accelerometers can easily be connected to, while diverting outputs from the pendulum apparatus to a separate DAQ is more time consuming. Since the cameras will be used as verification for all experiments, the use of a different DAQ should not be a problem provided there is adequate agreement in all experiments.

2.3.1 National Instruments Data Acquisition

This data acquisition system will be used in the double pendulum and crash test experiments. It consists of a desktop computer, which contains a National Instruments 6024E data acquisition card, running MATLAB based data acquisition software. A terminal block, which is connected to the data acquisition, or DAQ, card is used to gather signals from the sensors through wires attached to the appropriate input channels. Also, a 5 V linear power supply is connected to the block to provide power for the system. Figure 2.7 shows this set-up.

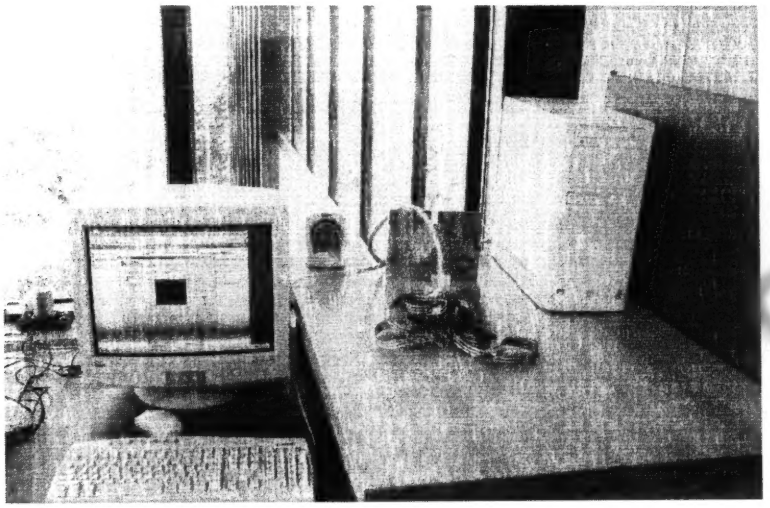

Figure 2.7: National Instruments data acquisition set-up

Triggering will be achieved in two different ways. In the double pendulum experiment a nine volt battery will be connected through a switch, which will be activated manually, to the terminal block and high speed cameras to allow synchronization. In the crash test experiment a 5 V signal, which coincides with firing of the hydraulic cylinder, will be diverted to the terminal block and high speed cameras so that measurement commences with impact. Table 2.1 lists the important specifications of the National Instruments 6024E data acquisition card used.

Table 2.1: National Instruments 6024E data aquisition card specifications

Parameter	**Description**
Analog Input	12 bit successive approximation ADC
Number of Channels	16 referenced single-ended
Input Range	± 5 V
Sampling Rate	**Double Pendulum**: 200 Hz/*Channel* · 9 *Channels* = 1.8 kHz
	Crash Test: 4000 Hz/*Channel* · 9 *Channels* = 36 kHz
	Maximum: 200 kHz
Accuracy	Noise: 1.95 mV
	Offset: 4.42 mV
	Absolute: 6.51 mV
Resolution	2.44 mV
Digital Input/Output	8 *Channels*
Warm-up Time	30 min suggested

2.3.2 dspace Data Acquisition

This data acquisition system will only be used for the translating pendulum experiment. It consists of a desktop computer, which contains a dspace 1104 R&D controller board, running dspace data acquisition software. A block diagram, that was composed in Simulink, will be compiled with the data acquisition interface to control the motion of the cart. Sensor outputs will be relayed to the appropriate analog input channels through RCA jacks which act as a terminal block. Again, the accelerometer boards will be powered by a 5 V linear power supply. Figure 2.8 shows this set-up.

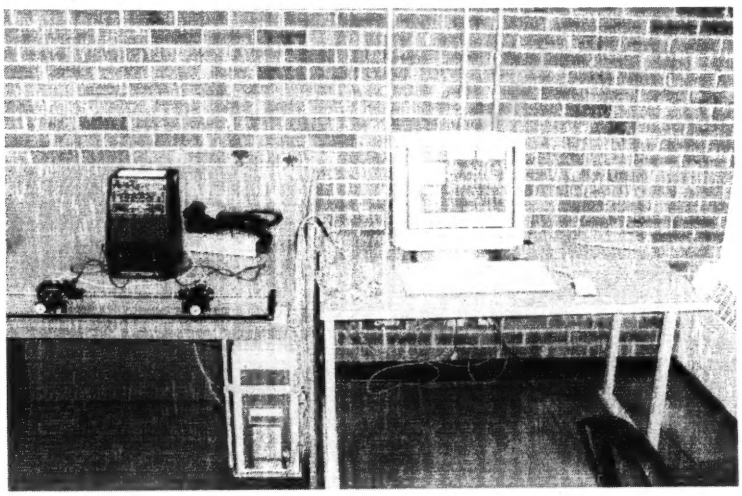

Figure 2.8: dspace data acquisition set-up

Triggering will be achieved by diverting the TTL signal, which coincides with each exposure, from the External Synch Out pin on the high speed cameras to the designated trigger channel. Therefore, data collection will commence when the cameras are activated. Table 2.2 lists the important specifications of the dspace 1104 R&D controller board.

Theory related to the operation of the high speed cameras, potentiometers and encoders can be found in Appendix A.

Table 2.2: dspace 1104 controller board specifications

Parameter	**Description**
Number of Channels	4 ADC inputs - multiplexed, 16 bit
	4 ADC inputs, 12 bit
	2 Incremental Encoder interfaces
Input Range	±5V
Sampling Rate	**Translating Pendulum**: 2000 Hz/*Channel* · 9 *Channels* = 18 kHz
	Maximum: 1.6 MHz
Signal-to-Noise Ratio	>80 dB (16bit)
	>65 dB (12bit)
Resolution	0.153 mV (16 bit)
	2.44 mV (12bit)
Digital Input/Output	20-bit digital I/O (bit-selectable)
Warm-up Time	30 min suggested

Chapter 3

System Uncertainty

In this chapter, the error associated with determining kinematic parameters from accelerometer measurements during static and dynamic movement will be assessed. Since the uncertainty in accelerometer output propagates to all other kinematic variables, it will be determined first. The effects of this uncertainty on measurement of static angles, as well as angular and translational kinematics will be discussed next. Also, the effect of high pass filtering on uncertainties associated with integrating time-dependent signals will be shown. Finally, an approximation of the uncertainty in double differentiated position data, which is obtained from the high speed cameras, will be determined.

3.1 Accelerometer Output Uncertainty

The three factors that will be considered for uncertainty in accelerometer output are misalignment of the sensitive axis, noise, and sensitivity. Based on specifications from Analog Devices, the alignment error for the sensitive axis is $\pm 1^0$ and the noise on the accelerometer, which has white Gaussian noise characteristics, is expressed as

$$Noise(rms) = \left(200\frac{\mu g}{\sqrt{Hz}}\right)\sqrt{BW \cdot 1.5} \tag{3.1}$$

for 2 g and 10 g accelerometers, where BW is the bandwidth of the system, which has been set to 50 Hz, and $\frac{\mu g}{\sqrt{Hz}}$ are units.

$$Noise(rms) = \left(200\frac{\mu g}{\sqrt{Hz}}\right)\sqrt{50 \cdot 1.5} = 1.7\ mg.$$

The rms value indicates where the majority of noise is concentrated, since it is defined as one standard deviation from the true signal. However, peak to peak noise

gives the best estimate of uncertainty in a single measurement. The peak to peak noise is expected to remain within 4× the $Noise(rms)$ value for 95% of the time, based on a normal distribution. This results in a value of

$$4 \times 1.7\ mg = 6.8\ mg.$$

This value corresponds to the smallest measurable acceleration, since smaller accelerations will be indistinguishable from noise. The resolution of the accelerometer system, or quantization error, is determined from the following expression

$$\frac{resolution_{DAQ}}{sensitivity_{Accelerometer}} = resolution_{System}. \tag{3.2}$$

National Instruments Data Acquisition (DAQ) resolution is

$$\frac{10\ V}{2^{12}-1} = 2.44\ mV,$$

based on a full scale 10 V input, and a 12-bit system. 10 g accelerometer sensitivity is 100 $\frac{mV}{g}$, while the 2 g accelerometer sensitivity is 312 $\frac{mV}{g}$. This leads to a 10 g system resolution of

$$\frac{2.44\ mV}{100\ \frac{mV}{g}} = 24.4\ mg,$$

and a 2 g system resolution of

$$\frac{2.44\ mV}{312\ \frac{mV}{g}} = 7.8\ mg.$$

In both the 2 g and 10 g cases, the system resolution is larger than the peak to peak noise. Therefore, the error in acceleration measurements will correspond to system resolution. It should be noted that the data acquisition sensitivity is based on a 10 V (-5 V→5 V) input signal to utilize all 12 bits. In our case the input signal is only 5 V (0 V→5 V) which means only 11 of the 12 bits will be used.

Next we will derive an analytical expression for the uncertainty in accelerometer output. We begin with

$$A_{output} = f_1(A_{actual}, A_\perp, \gamma) = A_{actual}\cos\gamma + A_\perp \sin\gamma \tag{3.3}$$

where A_{output} is the system's measurement of acceleration assuming no measurement errors in the system aside from finite resolution, A_{actual} is the true acceleration that we are trying to measure, $A_\perp$ is the acceleration perpendicular to A_{actual} and γ is the misalignment of the sensitive axis. Figure 3.1 shows this graphically.

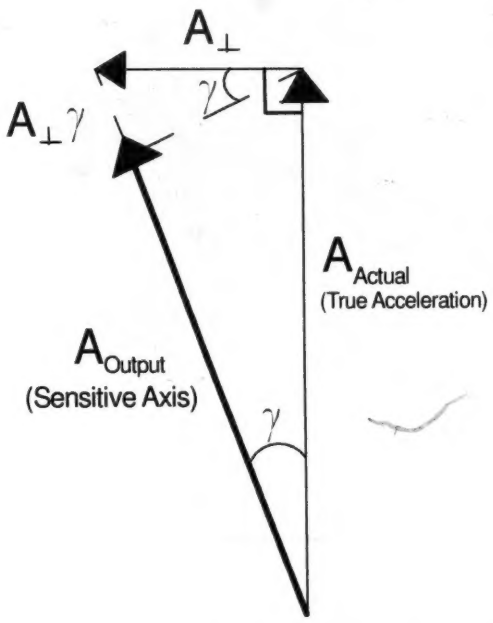

Figure 3.1: Effects of sensitive axis misalignment on acceleration measurement. γ is considered a small angle.

For simplicity we are assuming two-dimensional misalignment only. Since the input variable's uncertainties are independent of each other, we can use Taylor series expansion to determine the effects of combined uncertainty on a single parameter. The sensitivity of an acceleration measurement to misalignment and output uncertainties can now be assessed. We begin with the Taylor series expansion of 3.3

$$\Delta A_{output} = \frac{df_1}{dA_{actual}} \cdot \Delta A_{actual} + \frac{df_1}{dA_{\perp}} \cdot \Delta A_{\perp} + \frac{df_1}{d\gamma} \cdot \Delta\gamma$$

now the uncertainties are expressed as

$$u_{A_{output}} = \sqrt{\left(\frac{df_1}{dA_{actual}} \cdot u_{A_{actual}}\right)^2 + \left(\frac{df_1}{dA_{\perp}} \cdot u_{A\perp}\right)^2 + \left(\frac{df_1}{d\gamma} \cdot u_{\gamma}\right)^2}$$

where the Δ terms are now expressed as uncertainties. If we substitute into the above expression, the result is

$$u_{A_{output}} = \sqrt{(\cos\gamma \cdot u_{A_{actual}})^2 + (\sin\gamma \cdot u_{A_{\perp}})^2 + ((-A_{actual}\sin\gamma + A_{\perp}\cos\gamma) \cdot u_{\gamma})^2}$$

where $u_{A_{output}}$ refers to the uncertainty in A_{output}, which was described on the previous page, $u_{A_{actual}}$ is the uncertainty in true acceleration measured by the DAQ, while u_{γ}

refers to uncertainty in the alignment of the sensitive axis. This expression reduces to

$$u_{A_{output}} = \sqrt{(\cos 0 \cdot u_{A_{actual}})^2 + (\sin 0 \cdot u_{A_\perp})^2 + (-A_{actual} \sin 0 \cdot u_\gamma + A_\perp \cos 0 \cdot u_\gamma)^2}$$

or

$$u_{A_{output}} = \sqrt{u_{A_{actual}}^2 + (A_\perp \cdot u_\gamma)^2}. \tag{3.4}$$

The following parameters, which are based on static accelerometer measurement, have been derived to determine the worst case uncertainty in a single acceleration measurement. The bias term in the $u_{A_{actual}}$ expression refers to the difference between true and perceived acceleration. This term is incorporated to account for a voltage offset due to calibration error.

$$\begin{aligned}
u_{A_{actual}}(10\ g) &= \sqrt{system\ resolution^2 + bias^2} = \sqrt{24.4\ mg^2 + 44.8\ mg^2} = 51.0\ mg \\
u_{A_{actual}}(2\ g) &= \sqrt{system\ resolution^2 + bias^2} = \sqrt{7.8\ mg^2 + 15.6\ mg^2} = 17.4\ mg \\
u_\gamma &= \sqrt{misalignment^2 + construction\ error^2} = \sqrt{0.0175\ rad^2 + 0.0438\ rad^2} = 0.0472\ rad \\
A_\perp &= 2000\ mg\ (2 \times gravity)
\end{aligned}$$

A translational acceleration of 2×gravity will be substituted for the perpendicular acceleration term since it is the maximum measurable acceleration by the 2 g system. 2 g and 10 g accelerometer bias's were approximated as 2× the system sensitivity, and alignment error due to construction was approximated at 2.5 degrees. Substituting these values into Equation 3.6 results in

$$\begin{aligned}
u_{A_{output}}(10\ g) &= \sqrt{(51.0\ mg)^2 + (\sqrt{2000\ mg^2 + 24.4\ mg^2} \cdot 0.0472\ rad)^2} = 107.3\ mg \\
u_{A_{output}}(2\ g) &= \sqrt{(17.4\ mg)^2 + (\sqrt{2000\ mg^2 + 7.8\ mg^2} \cdot 0.0472\ rad)^2} = 95.9\ mg
\end{aligned}$$

These errors are equivalent to 1.33 $\frac{m}{s^2}$ (107.3 mg) for the 10 g system and 0.96 $\frac{m}{s^2}$ (95.9 mg) for the 2 g system, which corresponds to 5.4% and 4.8% of the full scale input acceleration assuming that A_{actual}, $A_\perp = 2\ g$. The second term in the above expression, which is error due to misalignment and perpendicular acceleration, is the largest contributor to uncertainty in both systems during dynamic measure.

3.2 Static Angle Measurement

Static angles can be determined from biaxial accelerometer output through measurement of the gravity vector. This relationship is shown in Figure 3.2

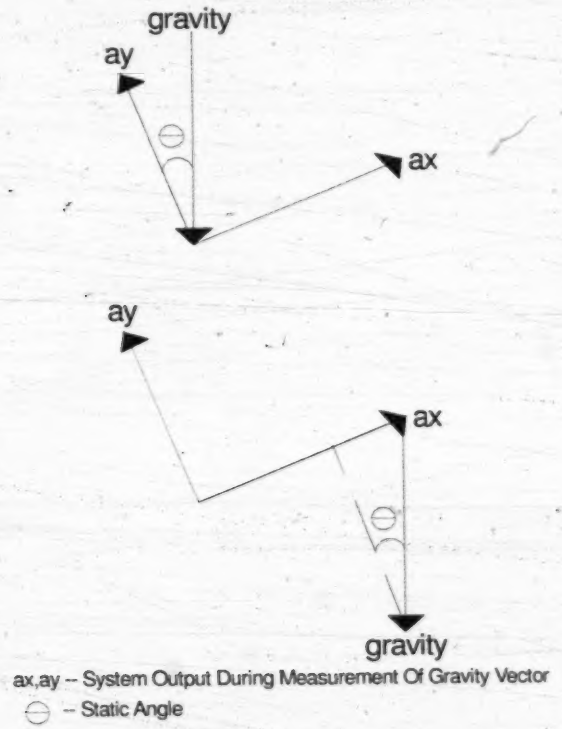

Figure 3.2: Relationship between sensitive axis' of a biaxial accelerometer and the gravity vector

From the Figure above, the relationships for θ are

$$\theta = \cos^{-1} \frac{a_y}{gravity}$$
$$\theta = \sin^{-1} \frac{a_x}{gravity}$$

Based on the uncertainty in static accelerometer measurement from the previous section, the uncertainty in θ is

$$u_{\theta 1(10\ g)} = \frac{\pi}{2} - \cos^{-1} \frac{51}{1000} = 0.051\ rad\ (2.92\ \text{deg})$$

for the 10 g accelerometers and

$$u_{\theta 1(2\ g)} = \frac{\pi}{2} - \cos^{-1}\frac{17.4}{1000} = 0.0174\ rad\ (0.99\ \text{deg})$$

for the 2 g accelerometers. These uncertainties are based on system sensitivity and bias only, if we include sensitive axis misalignment and construction error the result is

$$\begin{aligned} u_{\theta(10\ g)}\sqrt{2.92^2 + 1^2 + 2.5^2} &= 0.07\ rad\ (4.01\ \text{deg}) \\ u_{\theta(2\ g)}\sqrt{0.99^2 + 1^2 + 2.5^2} &= 0.05\ rad\ (2.86\ \text{deg}) \end{aligned}$$

Since the main reason for determining static angles is to ensure the gravity vector can be removed from system output, the theoretical uncertainties shown here are acceptable. Based on these uncertainties, 99% of the gravity component will be removed.

3.3 Angular Uncertainty

In this section the uncertainties associated with angular acceleration, velocity and displacement will be determined. This is based on errors in accelerometer output, which were derived in the previous section, and accelerometer spacing.

3.3.1 Angular Acceleration

The angular acceleration of a rigid body in two-dimensions can be found from

$$\alpha_3 = f_2(A_1, A_2, b) = \frac{A_1 - A_2}{b}$$

where A_1, A_2, and b were defined in Chapter 2. To derive the uncertainty we, again, start with a Taylor series expansion

$$\Delta\alpha_3 = \frac{df_1}{dA_1}\cdot\Delta A_1 + \frac{df_1}{dA_2}\cdot\Delta A_2 + \frac{df_1}{dy}\cdot b,$$

which yields the uncertainty expression

$$u_{a_3} = \sqrt{\left(\frac{df_1}{dA_1}\cdot u_{A_1}\right)^2 + \left(\frac{df_1}{dA_2}\cdot u_{A_2}\right)^2 + \left(\frac{df_1}{db}\cdot u_b\right)^2},$$

or,

$$u_{\alpha_3} = \sqrt{\left(\frac{1}{b}\cdot u_{A_1}\right)^2 + \left(\frac{-1}{b}\cdot u_{A_2}\right)^2 + \left(\left(\frac{A_2 - A_1}{b^2}\right)\cdot u_b\right)^2} \qquad (3.5)$$

where u_{A_1} and u_{A_2} refer to the uncertainties in accelerometer output, while u_y refers to uncertainty in accelerometer spacing. The static uncertainties derived in section 3.1 will be used to evaluate the above expression assuming a static measurement (angular acceleration = 0, $A_\perp = 0$).

$$\begin{aligned} b &= 41\ mm \\ u_b &= 0.5\ mm \\ u_{A_1}, u_{A_2}(10\ g) &= \pm 0.50\ \frac{m}{s^2} \\ u_{A_1}, u_{A_2}(2\ g) &= \pm 0.17\ \frac{m}{s^2} \\ A_1 - A_2 &= 0.01\ \frac{m}{s^2} \end{aligned}$$

$A_1 - A_2$ is based on the difference in acceleration measurements due to misalignment of the sensitive axis'. To simulate a worst case scenario, the misalignment between the two measurements was assumed to be 0.0873 *rad* (5 deg). The uncertainties in angular acceleration are:

$$u_{\alpha 10\ g} = \sqrt{\left(-\frac{1}{0.041}.0.50\right)^2 + \left(\frac{1}{0.041}.0.50\right)^2 + \left(\frac{0.01}{0.041^2}\cdot 0.0005\right)^2} = 17.25\ \frac{rad}{s^2}$$

for the 10 g system and

$$u_{a2\ g} = \sqrt{\left(-\frac{1}{0.041}.0.17\right)^2 + \left(\frac{1}{0.041}.0.17\right)^2 + \left(\frac{0.01}{0.041^2}\cdot 0.0005\right)^2} = 5.86\ \frac{rad}{s^2}$$

for the 2 g system. Uncertainty due to accelerometer spacing is insignificant when compared to the uncertainties in accelerometer measurements. The results shown above appear to be quite large; however, because accelerometer bias is the largest contributing factor, we may be able to reduce it through knowledge of initial conditions.

3.3.2 Angular Velocity and Displacement

To determine angular velocity, the angular acceleration was passed through a trapezoidal integrating filter. The corresponding coefficients are

$$A = [1, -1, 0]$$

and

$$B = [0, \frac{dt}{2}, \frac{dt}{2}],$$

with dt being the time-step. The filtering equation

$$y(n) = \sum_{k=0}^{2} B_{k+1} x(n-k) - \sum_{k=1}^{2} A_{k+1} y(n-k). \tag{3.6}$$

becomes

$$\omega(n) = \frac{dt}{2}\alpha(n-1) + \frac{dt}{2}\alpha(n-2) + \omega(n-1),$$

through substitution of the coefficients. This leads to the following expression for uncertainty in angular velocity

$$u_{\omega(n)} = \sqrt{\left(\frac{dt}{2} \cdot u_{\alpha(n-1)}\right)^2 + \left(\frac{dt}{2} \cdot u_{\alpha(n-2)}\right)^2 + \left(u_{\omega(n-1)}\right)^2},$$

where $u_{\alpha(n-1)}$ *and* $u_{\alpha(n-2)}$ refer to uncertainties in angular acceleration from two previous time-steps, while $u_{\omega(n-1)}$ is the uncertainty in ω from one time-step earlier. The final term in the uncertainty equation leads to an accumulation of error over time. If we assume a time-step of 0.005 s (200 Hz sampling rate), uncertainty in angular acceleration to be 17.25 $\frac{rad}{s^2}$ for the 10 g analysis, and 5.86 $\frac{rad}{s^2}$ for the 2 g analysis, and an initial error in angular velocity of 0, the uncertainty in angular velocity will increase in the following way

$$u_{\omega(n)} = \sqrt{u^2_{\omega_{(n-1)}} + 2 \cdot (0.0025 \cdot u_\alpha)^2}. \tag{3.7}$$

Figure 3.3 represents the error graphically, based on use of the 10 g system.

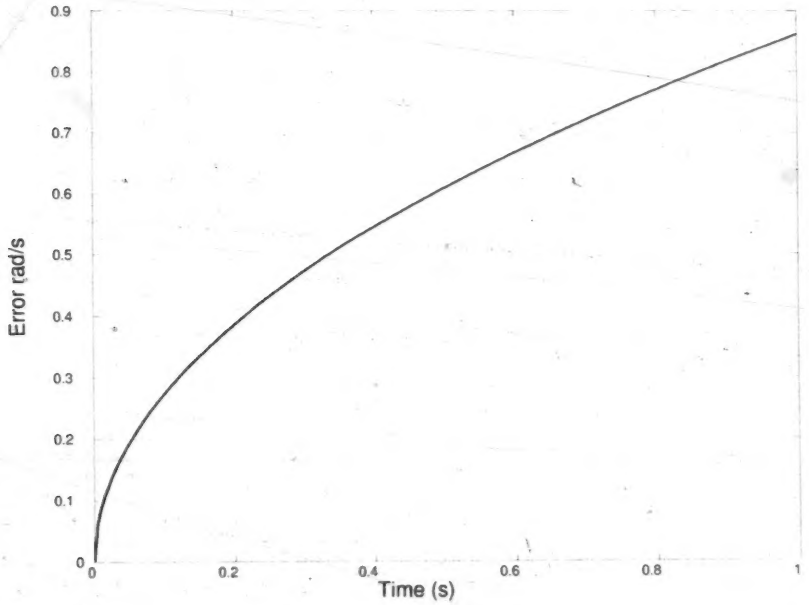

Figure 3.3: Error associated with single integration of a time dependent signal

The maximum error is approximately 0.86 $\frac{rad}{s}$ for the 10 g accelerometers, and 0.29 $\frac{rad}{s}$ for the 2 g accelerometers, after a 1 s interval. Since the results above are based on a static measurement, where the angular velocity should be 0, we can expect accumulation of error to contribute to signal drift.

Angular displacement is determined by integrating angular velocity. The uncertainty is expressed as

$$u_{\theta(n)} = \sqrt{\left(\frac{dt}{2} \cdot u_{\omega(n-1)}\right)^2 + \left(\frac{dt}{2} \cdot u_{\omega(n-2)}\right)^2 + \left(u_{\theta(n-1)}\right)^2}. \tag{3.8}$$

Again the final term in the expression, which is the uncertainty in θ from the previous time-step, leads to an accumulation of error over time. Figure 3.4 shows a graphical representation of the error, based on use of the 10 g system.

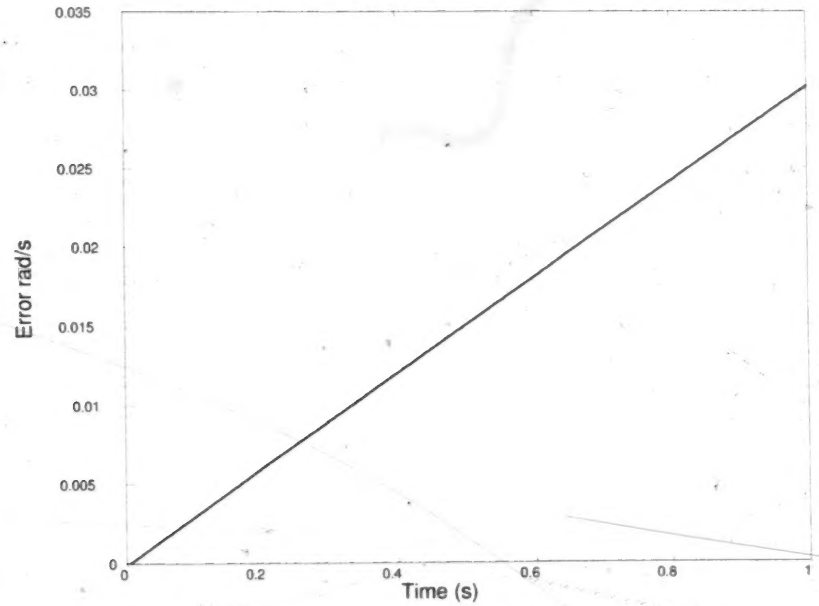

Figure 3.4: Error associated with double integration of a time dependent signal

The error increases linearly to a maximum value of approximately 0.030 *rad* (1.7 deg) for the 10 g system, and 0.010 *rad* (0.6 degrees) for the 2 g system. As was the case with angular velocity, these errors result over time while measuring an angle of 0. Since the double integration of time-dependent signals typically results in substantial signal drift, the magnitude of the error shown above will most likely not be significant.

3.4 Translational Uncertainty

In this section we will discuss the effects of uncertainties in different parameters on the determination of translational variables. The acceleration equation, which will be used to determine the translational acceleration of a specific point on a rigid body (pendulum, head or jaw), will be evaluated. Also, the results of integrating this signal to obtain translational velocity and displacement information will be assessed.

3.4.1 Translational Acceleration

The relative acceleration of two points on a rigid body, which was reviewed in Chapter 2, is expressed as

$$\vec{a}_2 = \vec{a}_1 + \vec{\alpha} \times \vec{r} + \vec{\omega} \times (\vec{\omega} \times \vec{r})$$

where a_1 is the acceleration of a point on the body, α is the angular acceleration of the rigid body, ω is the angular velocity of the rigid body, and r is the displacement vector from point 1, where the acceleration is known, to point 2. If we assume 2-D motion, the above equation reduces to

$$a_{2/N} = f_4(a_1, r, \alpha, \omega) = a_1 + \alpha_3[-b, a, 0] - \omega_3^2[a, b, 0],$$

where a and b have already been defined. Rewriting this equation in its vector components, based on earlier definitions, results in

$$A_2 = A_1 - \alpha_3 b - \omega_3^2 a$$

and

$$B_2 = B_1 + \alpha_3 a - \omega_3^2 b.$$

The uncertainty in these components is

$$\begin{aligned} \Delta A_2 &= \frac{df_4}{dA_1} \cdot \Delta A_1 + \frac{df_4}{d\alpha_3} \cdot \Delta\alpha_3 + \frac{df_4}{d\omega_3} \cdot \Delta\omega_3 + \frac{df_4}{db} \cdot \Delta b + \frac{df_4}{da} \cdot \Delta a \qquad (3.9) \\ u_{A_2} &= \sqrt{\left(\frac{df_4}{dA_1} \cdot u_{A_1}\right)^2 + \left(\frac{df_4}{d\alpha_3} \cdot u_{\alpha_3}\right)^2 + \left(\frac{df_4}{d\omega_3} \cdot u_{\omega_3}\right)^2 + \left(\frac{df_4}{da} \cdot u_a\right)^2 + \left(\frac{df_4}{db} \cdot u_b\right)^2} \\ u_{A_2} &= \sqrt{(u_{A_1})^2 + (-b \cdot u_{\alpha_3})^2 + (-2\omega_3 a \cdot u_{\omega_3})^2 + (-\omega_3^2 \cdot u_a)^2 + (-\alpha_3 \cdot u_b)^2} \end{aligned}$$

and

$$\begin{aligned} \Delta B_2 &= \frac{df_4}{dB_1} \cdot \Delta B_1 + \frac{df_4}{d\alpha_3} \cdot \Delta\alpha_3 + \frac{df_4}{d\omega_3} \cdot \Delta\omega_3 + \frac{df_4}{db} \cdot \Delta b + \frac{df_4}{da} \cdot \Delta a \qquad (3.10) \\ u_{B_2} &= \sqrt{\left(\frac{df_4}{dB_1} \cdot u_{B_1}\right)^2 + \left(\frac{df_4}{d\alpha_3} \cdot u_{\alpha_3}\right)^2 + \left(\frac{df_4}{d\omega_3} \cdot u_{\omega_3}\right)^2 + \left(\frac{df_4}{da} \cdot u_a\right)^2 + \left(\frac{df_4}{db} \cdot u_b\right)^2} \\ u_{B_2} &= \sqrt{(u_{B_1})^2 + (a \cdot u_{\alpha_3})^2 + (-2\omega_3 b \cdot u_{\omega_3})^2 + (-\omega_3^2 \cdot ub)^2 + (\alpha_3 \cdot u_a)^2} \end{aligned}$$

The following parameters, which are meant to simulate a static measurement, will be used to evaluate the above expressions:

$$
\begin{aligned}
\omega &= 0\ \frac{rad}{s} \\
\alpha &= 0\ \frac{rad}{s^2} \\
a &= 0.15\ m \\
b &= 0.10\ m \\
u_{A_1}, u_{B_1}(10\ g) &= \pm 0.50\ \frac{m}{s^2} \\
u_{A_1}, u_{B_2}(2\ g) &= \pm 0.17\ \frac{m}{s^2} \\
u_{\omega}(10\ g) &= \pm 0.86\ \frac{rad}{s} \\
u_{\omega}(2\ g) &= \pm 0.29\ \frac{rad}{s} \\
u_{\alpha}(10\ g) &= \pm 17.25\ \frac{rad}{s^2} \\
u_{\alpha}(2\ g) &= \pm 5.86\ \frac{rad}{s^2} \\
u_a, u_b &= \pm 0.003\ m
\end{aligned}
$$

The uncertainties in translational x and y accelerations, based on the above values, are 1.80 $\frac{m}{s^2}$ and 2.64 $\frac{m}{s^2}$ for the 10 g accelerometers, and 0.37 $\frac{m}{s^2}$ and 0.89 $\frac{m}{s^2}$ for the 2 g accelerometers. Because the calculation above was based on static measurement, only two terms in the expression contributed with the most significant contribution being made by uncertainty in angular acceleration. Therefore, to achieve substantial improvements in translational acceleration requires reduction of angular acceleration uncertainty.

3.4.2 Translational Velocity and Displacement

Translational velocity and displacement vectors are found through single and double integration of the translational x and y accelerations. The same integrating filter, which was employed in the angular uncertainty section, was also used to determine the translational variables. Uncertainty in translational velocity is expressed as

$$
\begin{aligned}
u_{V_x} &= \sqrt{\left(\frac{dt}{2} \cdot u_{A_1(n-1)}\right)^2 + \left(\frac{dt}{2} \cdot u_{A_1(n-2)}\right)^2 + \left(u_{Vx(n-1)}\right)^2} \qquad (3.11) \\
u_{V_y} &= \sqrt{\left(\frac{dt}{2} \cdot u_{B_1(n-1)}\right)^2 + \left(\frac{dt}{2} \cdot u_{B_1(n-2)}\right)^2 + \left(u_{V_y(n-1)}\right)^2}
\end{aligned}
$$

while the uncertainty in translational displacement is

$$u_{D_x} = \sqrt{\left(\frac{dt}{2} \cdot u_{Vx(n-1)}\right)^2 + \left(\frac{dt}{2} \cdot u_{Vx(n-2)}\right)^2 + \left(u_{Dx(n-1)}\right)^2} \qquad (3.12)$$

$$u_{D_y} = \sqrt{\left(\frac{dt}{2} \cdot u_{Vy(n-1)}\right)^2 + \left(\frac{dt}{2} \cdot u_{Vy(n-2)}\right)^2 + \left(u_{Dy(n-1)}\right)^2}.$$

u_{A_1} and u_{B_1} are the uncertainties in acceleration, u_{V_x} and u_{V_y} are the uncertainties in velocity, u_{D_x} and u_{D_y} are the uncertainties in displacement. As was shown in the angular parameter section, the integration process causes an accumulation of error. The maximum errors, in the four parameters discussed above, based on a 1s interval and a time-step of 0.005 (200 Hz sampling rate) are:

$$\begin{aligned}
u_{V_x}(10\ g) &= 0.090\ \frac{m}{s} \\
u_{V_y}(10\ g) &= 0.132\ \frac{m}{s} \\
u_{D_x}(10\ g) &= 0.003\ m \\
u_{D_y}(10\ g) &= 0.005\ m \\
u_{V_x}(2\ g) &= 0.019\ \frac{m}{s} \\
u_{V_y}(2\ g) &= 0.044\ \frac{m}{s} \\
u_{D_x}(2\ g) &= 0.0007\ m \\
u_{D_y}(2\ g) &= 0.002\ m
\end{aligned}$$

In all cases the maximum values occurred at the end of the 1 s interval and the error accumulation, for first and second integrations, followed the same pattern as was seen in the angular parameter section. Although the uncertainties shown above are quite low, they are based on static measurement where the magnitude of all kinematic parameters should be zero. Uncertainty in angular parameters will remain the same during dynamic measurement, based on the analysis done here, however, uncertainty in translational parameters will increase.

3.5 Dynamic Uncertainty

During dynamic measurement the uncertainties in all kinematic parameters will increase. The values listed in tables 3.1 and 3.2 are based on accumulation of error where integration was performed.

Table 3.1: Angular Uncertainty During Dynamic Measurement

System	Angular Acceleration	Angular Velocity	Angular Displacement
10 g	52.1 $\frac{rad}{s^2}$	2.60 $\frac{rad}{s}$	0.09 rad
2 g	38.3 $\frac{rad}{s^2}$	1.91 $\frac{rad}{s}$	0.07 rad

Table 3.2: Translational Uncertainty During Dynamic Measurement

System	Acceleration x/y	Velocity x/y	Displacement x/y
10 g	16.5 $\frac{m}{s^2}$ / 13.2 $\frac{m}{s^2}$	0.83 $\frac{m}{s}$ / 0.66 $\frac{m}{s}$	0.029 m / 0.023 m
2 g	12.2 $\frac{m}{s^2}$ / 9.7 $\frac{m}{s^2}$	0.61 $\frac{m}{s}$ / 0.48 $\frac{m}{s}$	0.0213 m / 0.017 m

The uncertainties shown in the tables above are based on the following parameters:

$$\begin{aligned} \alpha &= 100\ \frac{rad}{s^2} \\ \omega &= 20\ \frac{rad}{s} \\ a &= 0.15\ m \\ b &= 0.10\ m \\ u_a, u_b &= \pm 0.003\ m \\ A_\perp &= 2\ g \end{aligned}$$

which are meant to predict a worst case scenario for the motion we intend to measure. Based on equation 3.4, uncertainty in dynamic acceleration measurement is very sensitive to sensitive axis misalignment. This is because the $A_\perp$ term is multiplied by sensitive axis misalignment. Larger values of $A_\perp$ lead to an increase in the uncertainty of accelerations measured by the system and, since all other kinematic parameters are derived from raw acceleration signals, this causes an increase in uncertainty for all parameters. Although the uncertainties determined are higher than desired, the analysis was based on a worst case scenario. Also, through knowledge of initial conditions, uncertainty may be reduced. Although the uncertainties discussed in this chapter cannot be directly applied to the pendulum and crash testing experiments, they will give an idea of where larger uncertainties can be expected. This analysis was done to gain a better understanding of the system's limitations.

3.6 High-Pass Filtering

One major problem with integration of time-dependent signals is drifting. Although the accumulation of error, which was discussed earlier in this chapter, does add to the

drift, it is not the principle cause. The DC value, which is the frequency component at 0 Hz, causes an offset that is present throughout the signal. This offset may not be substantial in the original signal, however, application of a numerical integrator causes amplification of low frequency components. This amplification is the principle cause of signal drift, and leads to increased uncertainty in time. In order to remove drift, the DC component must be eliminated. This can be done by passing the data through a high-pass filter. High-pass filtering involves saving all frequency components above a specific cut-off, while all those below the cut-off are removed.

To demonstrate how high-pass filtering reduces integration uncertainty, simulated data will be passed through a high-pass filter and the results will be analyzed. To prevent corruption of the signal we are interested in, the high-pass filter has to have a cut-off close to the DC value and a steep roll-off. For these reasons we selected a 4^{th} order Butterworth filter with a 0.5 Hz cut-off. The coefficients generated for this filter by MATLAB are:

$$\begin{aligned} A &= [1.00, -3.96, 5.88, -3.89, 0.96] \\ B &= [0.98, -3.92, 5.88, -3.92, 0.98]. \end{aligned}$$

and its frequency response is shown in Figure 3.5.

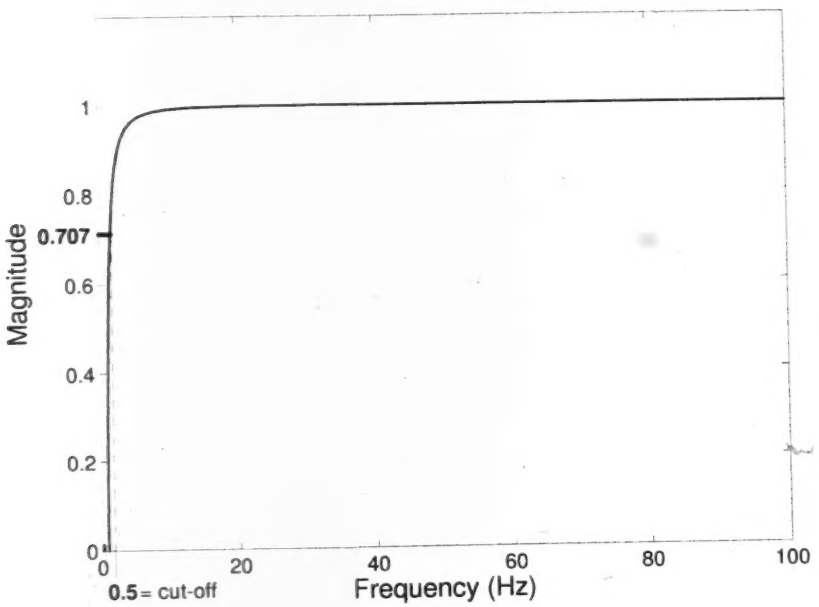

Figure 3.5: Frequency response of a 4th-order high-pass Butterworth filter with a 0.5Hz cut-off

Substitution of A and B into the recursive filtering equation

$$y(n) = \sum_{k=0}^{k=M} B_k x(n-k) - \sum_{k=1}^{k=N} A_k y(n-k)$$

where y(n) is the filtered signal, M+1 is the number of elements in B, and N is the number of elements in A, results in

$$\begin{aligned} y(n) &= 0.98x(n) - 3.92x(n-1) + 5.88x(n-2) - 3.92x(n-3) + 0.98x(n-4) \\ &\quad +3.96y(n-1) - 5.88y(n-2) + 3.89y(n-3) - 0.96y(n-4) \end{aligned}$$

where $y(n)$ refers to the drifting signal. We define the function to be integrated as the sine wave

$$m = 100 \sin 2\pi t$$

based on the dynamic uncertainty analysis where an angular acceleration of $100\frac{rad}{s^2}$ was assumed. The integral of this function is

$$\int m dt = -\frac{100}{2\pi} \cos 2\pi t.$$

If no DC component was present in the signal, and we assume a sampling rate of 200 Hz and a time interval of 1s, the signal before and after integration would look like Figure 3.6. Since this simulation is based on an object starting from rest, the start value for the first integral, which for simulation purposes corresponds to angular velocity, has been set to 0.

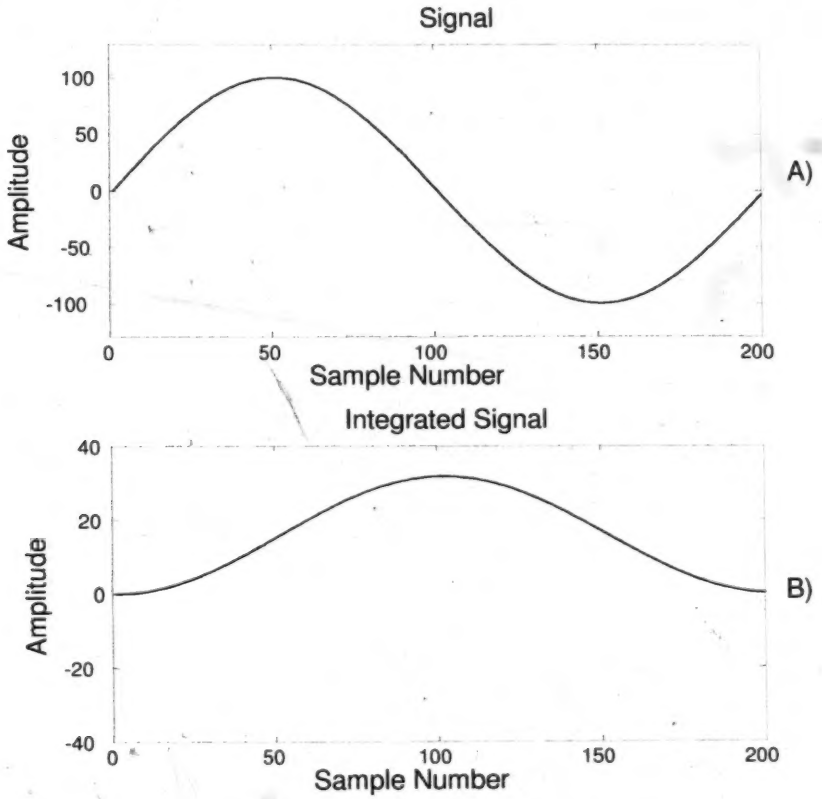

Figure 3.6: Integration of an error free signal

However, it was shown earlier that the uncertainty in an angular acceleration measurement of 100 $\frac{rad}{s^2}$ can be close to 50 $\frac{rad}{s^2}$, which would correspond to a DC component with a magnitude of 50. Figure 3.7 shows what occurs when this signal is integrated.

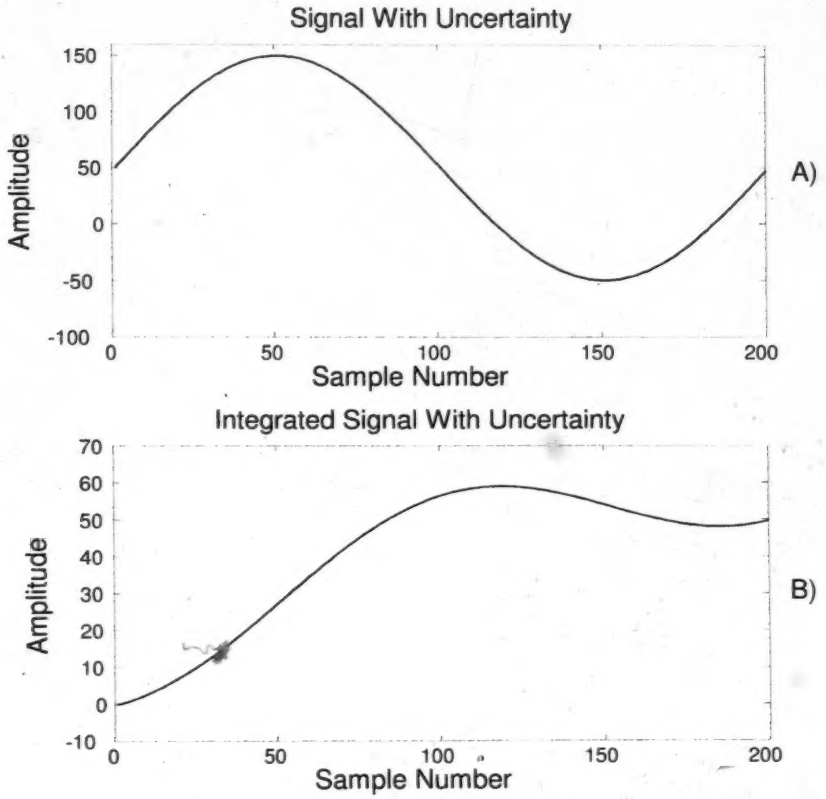

Figure 3.7: Integration of a signal with a DC offset

Substantial drift can be seen as a result of the added DC offset. The maximum value of the integrated signal is nearly twice what is seen in Figure 3.6, which corresponds to an uncertainty of nearly 100%. Figure 3.8B shows the frequency spectrum of the integrated signal.

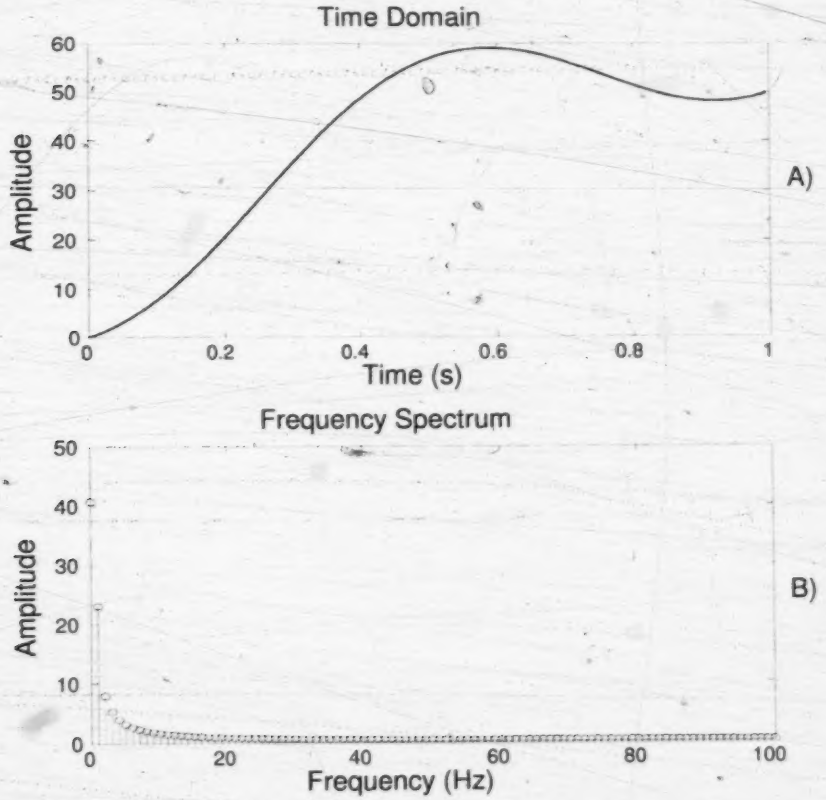

Figure 3.8: Frequency spectrum of an integrated signal with a DC offset.

The DC offset can be seen at 0 Hz and its amplitude is nearly twice that of the component at 1 Hz, which is the component we are interested in. Next, we will pass the data through the high-pass filter that was discussed earlier in this chapter. The result is shown in Figure 3.9.

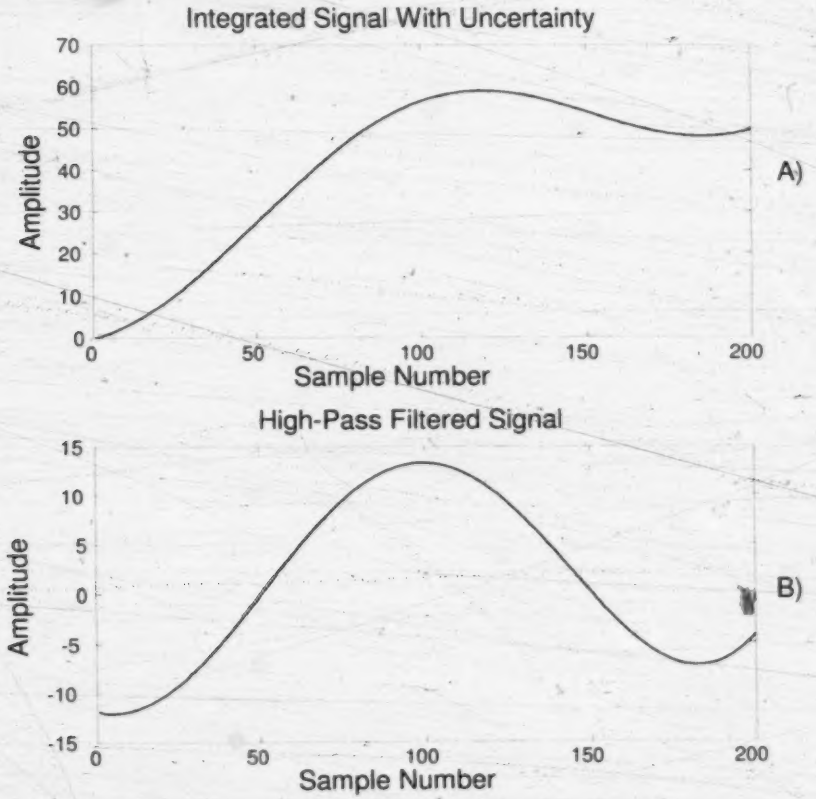

Figure 3.9: Result of high-pass filtering the drifting signal

The drift from the signal has been mostly removed, however, the signal is still offset. Since we will know that all experiments in this thesis will start from rest, the signal should start at 0, therefore, the initial value will be subtracted. Figure 3.10 shows the filtered frequency spectrum.

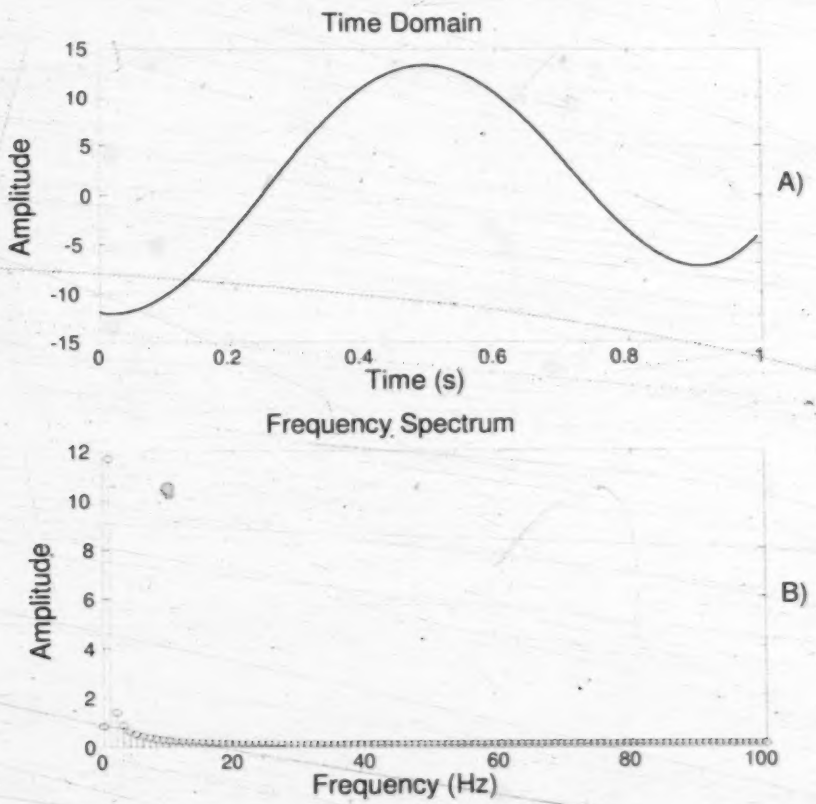

Figure 3.10: Frequency sprectrum after passing the integrated data through a high-pass filter.

The DC component has been almost completely removed, and the component at 1 Hz now has the largest amplitude. Figure 3.11 compares the uncertainty before and after application of the high-pass filter.

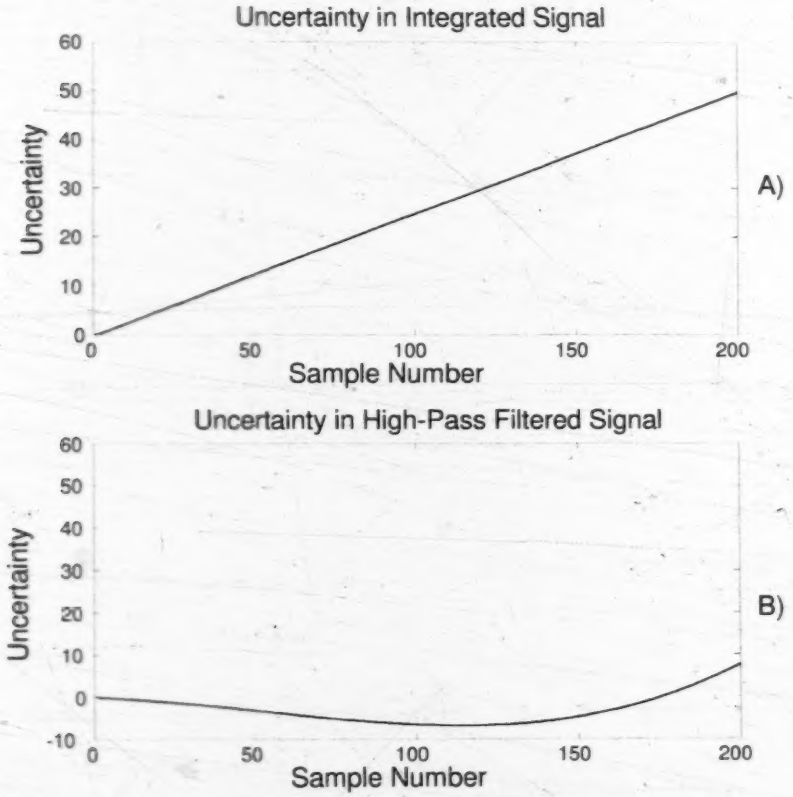

Figure 3.11: Uncertainty before and after high-pass filtering

High-pass filtering has reduced the uncertainty in measurement by more than 5×. A comparison between the true data (from Figure 3.6) and the filtered signal produced a correlation coefficient (R) and root mean square error (RMSE) of 0.9819 and 4.6230. The R value is a measure of the likeness between the variables being compared, where values close to 1 correspond to a high correlation between the data sets being compared, The RMSE value is the average error in the signal. In this case, it corresponds to 14.5% error expressed as a percentage of range. The filters performance could have been further improved by removing the offset prior to integration. In this simulation, if the initial value was subtracted no drift would have occurred. However, it is not so simple in real-life. Since the offset will not be constant as was assumed, subtraction of the initial value prior to integration (body starts from rest assumption) will eliminate drift to due accelerometer bias, but may not remove the entire DC component. In this thesis, double integration will be required to determine angular and translational displacements. Since this will cause further magnification of the DC value, increased

drift and uncertainty is expected in displacement data. One final thing to note is that this filter is recursive, which means it relies of past and future values. Large differences in these values can lead to start-up or ending transients. To minimize the effects, as well as to prevent phase distortion, all filtered data will be filtered forwards and backwards with the MATLAB function **filtfilt**.

3.7 Differentiated Position Data

Since high speed cameras will be used as the main source of verification for the accelerometer system, we need to assess the uncertainty in kinematics determined from their output. In the accelerometer system, integration is required to obtain full kinematic description since the sensors directly measure acceleration. An optical system, however, directly measures position which means differentiation is required to obtain full kinematic description.

Since all high speed camera data will be differentiated by the central difference method, we start with the equation.

$$f'(x) = \frac{f(x+1) - f(x)}{dt} \tag{3.13}$$

where $f'(x)$ is the derivative at the point of interest, $f(x)$ is point of interest from the original data set, and $f(x+1)$ is the value from one future time-step. The dt value is 0.005 based on a 200 Hz sampling rate. In order for camera calibration to be acceptable, a wand length range less than 2.5 mm with a standard deviation under 0.5 mm had to be achieved. Camera calibration is based on determination of wand length during dynamic movement. The procedure is described in detail in Appendix A. The Taylor series expansion of the above expression is

$$\Delta f'(x) = \frac{df'(x)}{df(x+1)}\Delta f(x+1) + \frac{df'(x)}{df(x)}\Delta f(x)$$

which yields the uncertainty expression

$$u_{f'(x)} = \sqrt{\left(\frac{u_{f(x+1)}}{dt}\right)^2 + \left(\frac{u_{f(x)}}{dt}\right)^2}.$$

Since one standard deviation away from the mean in a normal distribution encompasses 67% of the data, the standard deviation from calibration will be used as the uncertainty in a single position measurement. Substitution of 0.5 mm into the above expression yields

$$u_{f'(x)} = \sqrt{\left(\frac{0.0005}{0.005}\right)^2 + \left(-\frac{0.0005}{0.005}\right)^2}$$
$$u_{f'(x)} = 0.141\,\frac{m}{s}$$

Double differentiation leads to the uncertainty

$$u_{f''(x)} = \sqrt{\left(\frac{0.141}{0.005}\right)^2 + \left(\frac{0.141}{0.005}\right)^2}$$
$$u_{f''(x)} = 40.0\frac{m}{s^2}$$

Based on the results obtained here, the uncertainty in camera derived kinematics for translational displacement and velocity are lower than the accelerometer system. The uncertainty due to double differentiation (translational acceleration) is somewhat high, however, it will remain relatively constant while the uncertainty in translational kinematics determined with the accelerometer system increases at higher accelerations. Also, the calculations above were based on using the standard deviation, while the manufacturers claimed resolution is more than 10× smaller. Acceptable performance of the accelerometer system will be dependent on the average error not exceeding 10% of full scale for each kinematic variable, when compared with the high speed cameras. This value was selected based on the uncertainty in both systems, and the specifications given by a group planning to use this system in a separate rear-impact study.

Chapter 4

Double Pendulum Analysis

In this chapter the results of measuring the 2-D kinematics of a double pendulum, with 2 g and 10 g accelerometers, are reported. This experiment was done as a preliminary step in the development of a system for measuring head and jaw kinematics during low velocity rear-impact. Because rotation makes up a large portion of the movement a person experiences during impact, measurement of a swinging pendulum, was chosen as an initial verification for the system. Angular kinematics obtained from accelerometer output were verified with potentiometer and high speed camera data, while only the high speed cameras were used for verification of translational kinematics. Because crash testing involves impact, some accelerations experienced by the subject may exceed 2 g's, which is why both 2 g and 10 g accelerometers were evaluated. Although the 10 g accelerometers are capable of measuring the full range of expected accelerations, the system will be used during low-velocity impact where accelerations above 2 g's are expected, but accelerations in the 10 g range are unlikely. Therefore, the output from the 2 g and 10 g accelerometers was compared, and the effects of reduced sensitivity were assessed. The results presented in this section were obtained from two separate tests, one with the 2 g system, and one with the 10 g system.

4.1 Experimental Set-Up

A double pendulum, which was instrumented with potentiometers at both joints, was the test apparatus for this experiment. Both potentiometers were connected to a linear power supply, and calibrated through 180 deg with the +/- 5 V source. Specially designed circuit boards, which contained 2 g and 10 g accelerometers, were bolted to the upper and lower links of the pendulum to record their acceleration. A separate

5 V linear power supply was connected to the boards, and the output from both the accelerometers and potentiometers was relayed to a National Instruments Data Acquisition (NIDAQ) system through ribbon cables and a breakout box. Three high speed cameras, which sampled at 200 Hz, were placed around the test area and calibrated for a 1 $m \times 1\ m \times 1\ m$ space to monitor the pendulum's motion. The reflective markers, which the camera system recorded the positions of, were placed on the pendulum joints, and on one accelerometer from each board. These positions are shown in Figure 4.1.

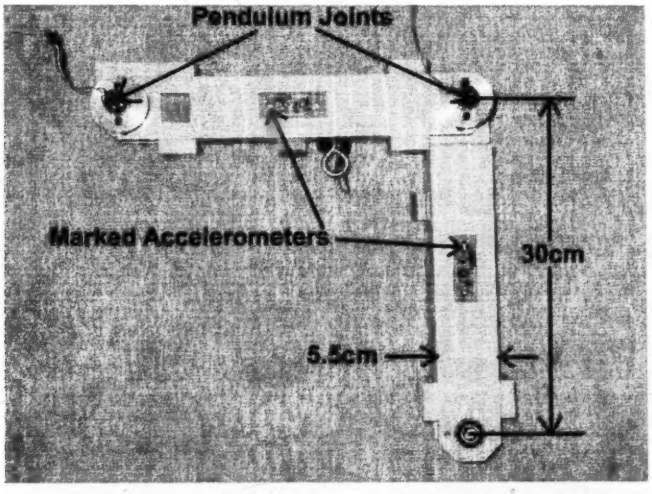

Figure 4.1: Instrumented double pendulum

The start configuration of each test consisted of the pendulum's upper link being fixed to the pendulum frame, while the lower link hung freely. Data collection was initiated by the release of the pendulum, and continued for a 10 second period. MATLAB was used to collect information from the NIDAQ at a rate of 200 Hz, while PCReflex software was used to collect data from the cameras. Determination of angular and translational parameters, as well as overlaying of data sets, and statistical comparison of kinematic parameters obtained from different systems was done with MATLAB. Although the chosen sampling rate was 200 Hz, the frequency range of interest was 0 Hz-15 Hz, therefore, all sensor outputs were low-pass filtered down to 15 Hz prior to any data analysis. A 15 Hz cut-off was selected based on an analysis of the raw accelerometer frequency spectrum as well as residual analysis. This procedure is demonstrated in Appendix B. A higher sampling rate was employed to prevent aliasing. Also, all integrated data was high-pass filtered with a 4^{th} order Butterworth filter (0.5 Hz cut-off), while all differentiated camera and potentiometer data was fil-

tered with a 5^{th} order low-pass Butterworth filter with a 15 Hz cut–off. Verification for this cut-off is also shown in Appendix B. The criteria for selecting an adequate high-pass filter was how well the filter removed drift without producing transients, which the 4^{th} order Butterworth was shown to do well in the previous chapter. The low-pass filter was selected for its steep roll-off, and 15 Hz was chosen as the cut-off since the raw accelerometer signals were filtered to the same degree. The performance of 2 g and 10 g accelerometers was evaluated in separate tests.

4.2 Discussion/Results

In this discussion, the performance of both 2 g and 10 g accelerometers for measuring angular and translational pendulum motion is evaluated. The evaluation is based on comparisons between accelerometer derived kinematics with those obtained from high speed camera and potentiometer measurements. The global coordinate system for this experiment is shown in Figure 4.2.

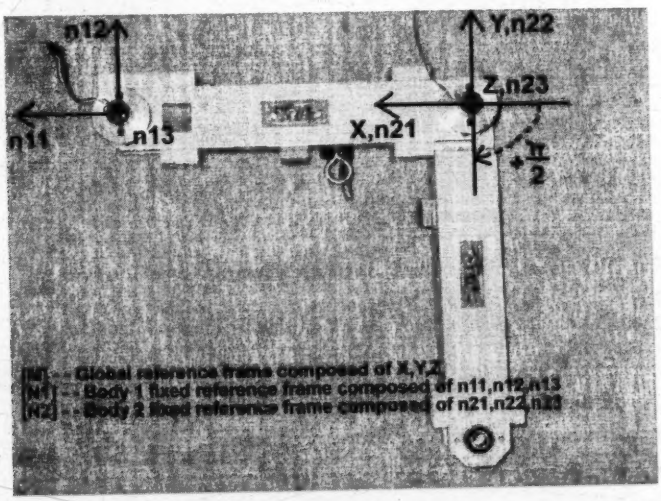

Figure 4.2: Global coordinate system for the double pendulum

The global reference frame is defined as [**M**], which is composed of the vectors $\vec{X}, \vec{Y}$ *and* $\vec{Z}$ as discussed in Chapter 2. The fixed reference frames [**N1**] and [**N2**] are defined by the vectors $\vec{n}_{11}, \vec{n}_{12}, \vec{n}_{13}$ and $\vec{n}_{21}, \vec{n}_{22}, \vec{n}_{23}$. Body 1 refers to the upper link, while body 2 refers to the lower link. Translation of the joint will be measured relative to its starting position.

4.2.1 2 g Angular Measurements

The angular accelerations, which were obtained in the way described in Chapter 2, were integrated to find angular velocity and orientation. Since numerical integration assumes a starting value of zero, initial conditions must be determined separately. This is not a problem for angular velocity because the pendulum starts from rest, but it is a problem for orientation since the correct angles are required to remove the gravity vector. However, it was shown in Chapter 3 that the uncertainty in determination of angles from static accelerometer measurements is acceptable, therefore, this technique was employed here.

High speed cameras recorded the positions of reflective markers, which were then converted to orientations and differentiated to obtain angular velocity and acceleration. Potentiometers directly measured the relative orientations of the links but determination of angular velocity and acceleration involved differentiation. To begin we will look at accelerometer data.

Figure 4.3 shows an overlaid plot of the accelerometer signals, from the upper link, that were used to determine angular acceleration. A1 and A2 refer to the signals from the parallel axis' as defined in the theory section of Chapter 2. In the pendulum's starting position, misalignment uncertainty due to measurement of the gravity vector, and accelerometer bias should be visible. Upon inspection of the data, the signals appear to start in very close agreement. The uncertainty in accelerometer output is well within the expected value determined in Chapter 3, and since uncertainty in angular acceleration is directly related to accelerometer output, it is also expected to be low. Raw acceleration signals from the lower-link are not shown, however, when they were compared, a noticeable offset was seen between the starting points of the signal. This was surprising since no difference was seen in the upper-link data. More explanation as to the cause of this offset is provided later in the chapter.

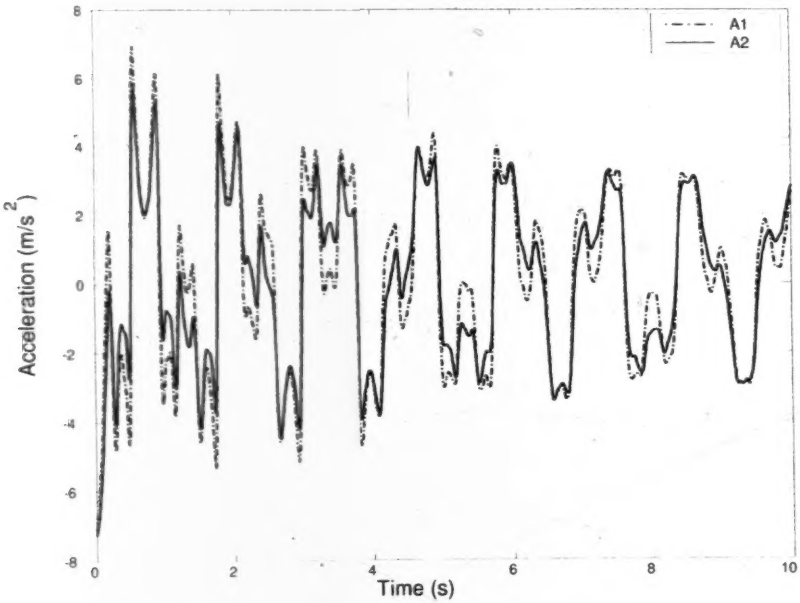

Figure 4.3: 2 g Parallel accelerometer signals from the upper-link during double pendulum motion.

Figures 4.4 and 4.5 show full and zoomed frequency spectrums for the upper and lower links. A1 and A2 are the parallel acceleration signals, which were defined in Chapter 2. Since the signals at time zero, for the upper link, appear to be nearly equivalent, a large DC value was not anticipated. The DC offset shown in Figure 4.4B is nearly non-existent.

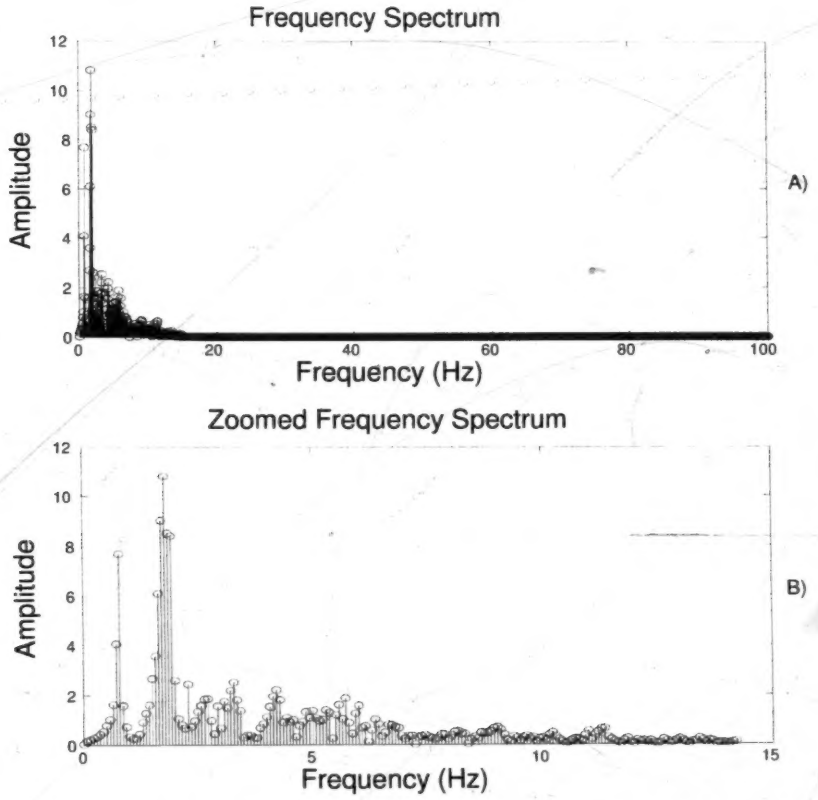

Figure 4.4: Frequency components of the upper-link's angular acceleration (2 g)

Figure 4.5B shows a DC component with an amplitude of 5.5, which is approximately 25% of the largest component in the spectrum. This is expected to produce an offset in the angular acceleration data obtained from the lower-link, since a difference between the accelerometer signals was seen at time 0. Although this component increases the uncertainty in angular acceleration, the cause is assumed to be mostly accelerometer bias, which we may be able to remove by subtracting the initial value. A comparison of the angular parameters obtained from the three different systems will now be presented.

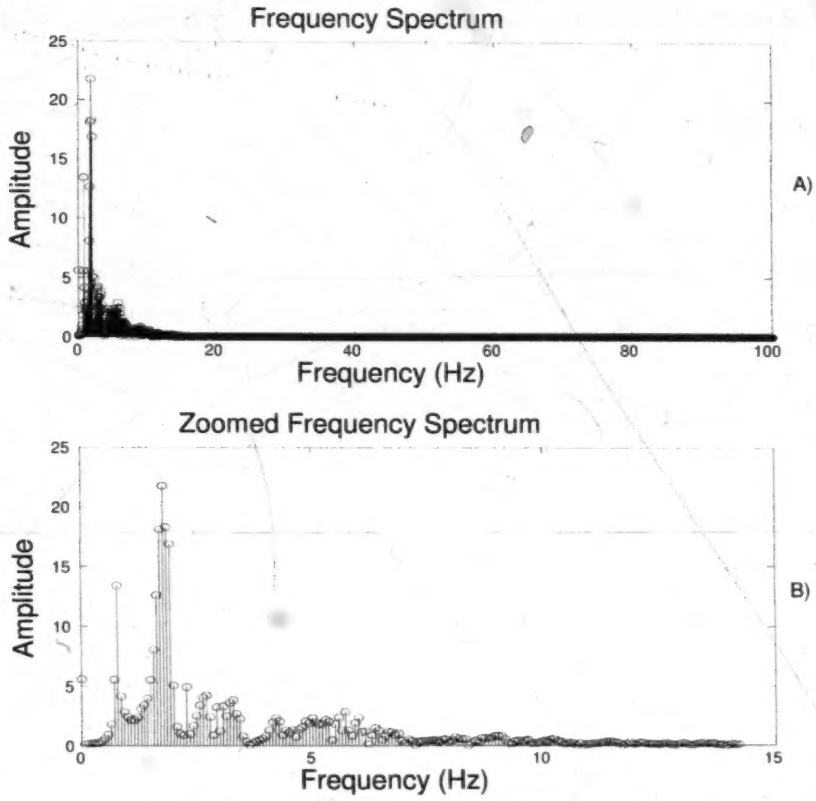

Figure 4.5: Frequency components of the lower-links angular acceleration (2 g)

Figures 4.6 and 4.7 show comparisons of angular accelerations, angular velocities and orientations which were obtained with 2 g accelerometers, cameras and potentiometers from the upper and lower links. Figures 4.6A and 4.6B, which compare angular acceleration and velocity, appear to be very consistent. Figure 4.6C, which compares orientation, shows a nearly constant offset between accelerometer output and the verification devices. Figure 4.7, which compares the same kinematic parameters for the lower-link, shows good agreement in all three plots. Removal of the lower links initial offset, which was almost 50 $\frac{rad}{s^2}$, appears to have effectively reduced the uncertainty in all angular parameters.

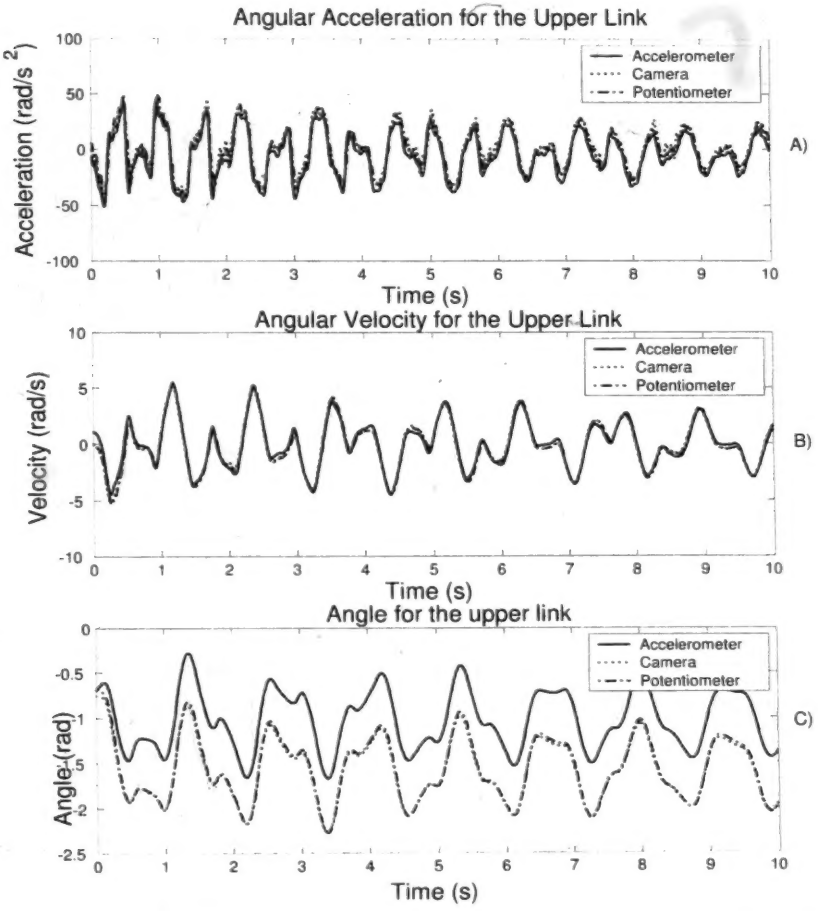

Figure 4.6: Angular kinematic variable comparison for the upper-link (2 g)

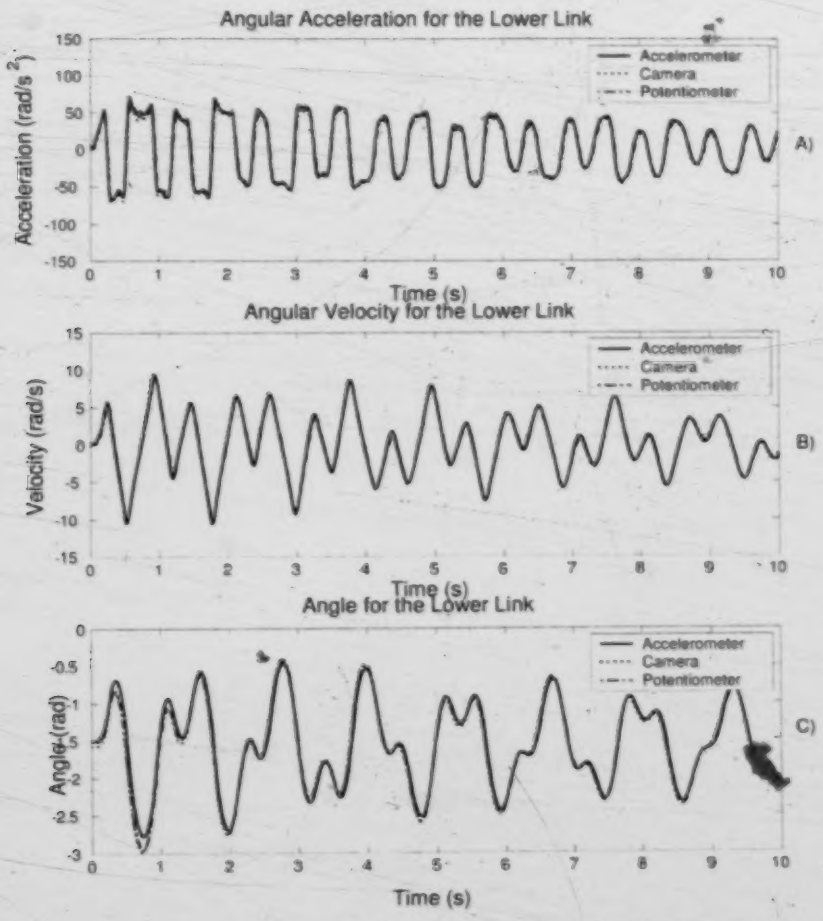

Figure 4.7: Angular kinematic variable comparison for the lower link (2 g)

Based on observation, it appears that the offset between accelerometer and potentiometer/high speed camera data, in Figure 4.6C, is relatively consistent. This was verified by determining the offset through peak matching, where the absolute maximum peak from the accelerometers was matched with the absolute maximum from the potentiometers, as opposed to using the initial angle. The result is shown in Figure 4.8. The data corresponds much better, which means that there is corruption at the start of the data set, which prevents aligning the data based on initial values alone.

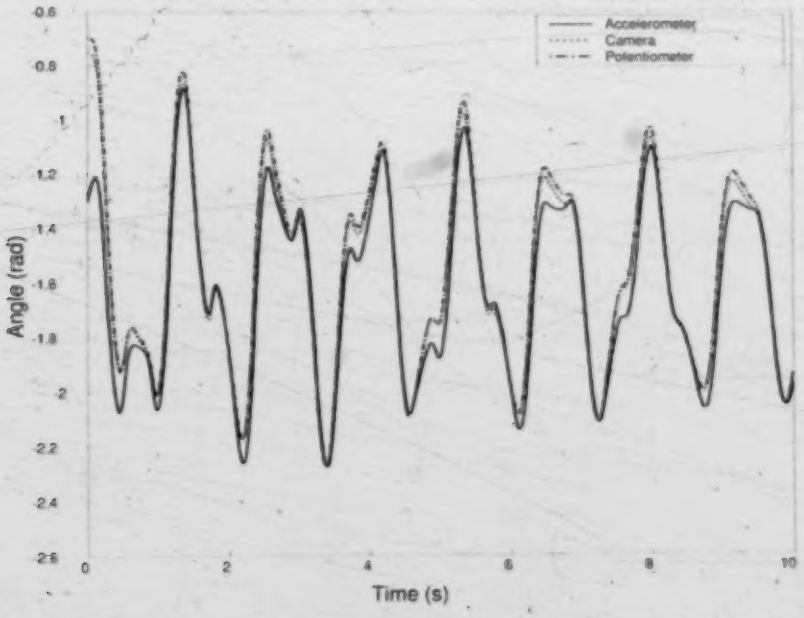

Figure 4.8: Peak matching between accelerometer and camera derived angles for the upper-link

Comparing trends in both upper and lower link data sets and examining the data in a physical sense, provided insight to the offset problem. When the pendulum is released, the top link begins rotating instantly which leads to a large change in orientation. The lower link, on the other hand, translates initially (demonstrated by the initial flat portion of Figure 4.7C) before starting rotation. Although the range of angles the lower link moved through was almost twice the range of the upper link, the initial change in angle for the upper link, approximately 1.25 *rad*, is substantially larger than the initial angular change in the lower link, approximately 0.75 *rad*. As was mentioned earlier, the orientation was found by double integrating the angular acceleration data, which resulted in some signal drift. To remove this, the data was passed through the 4^{th} order high-pass Butterworth filter (0.5 Hz cut-off), which was discussed in Chapter 3. Although this filter was shown to be effective for removing drift, in some cases it can cause distortion. The distortion is seen in the form of filter transients, which result because of the filters recursive nature. Recursive filters rely on past and future data to determine the current value. Large differences in these values can cause an impulse-like response when passed through the filter. This impulse gives rise to transients, which cause either over or underestimation making it impossible to determine the offset based on the initial values alone. However,

because peak matching was successful for removing the offset, the transient effect is not present throughout the entire data set. Based on this knowledge the initial 1.5 s of angular acceleration data was duplicated and placed at the start of the signal prior to integration. The length of data duplicated was determined based on at what point the end of the duplicated data would closely match the data in the original signal following the impulse. Figure 4.9 shows the result.

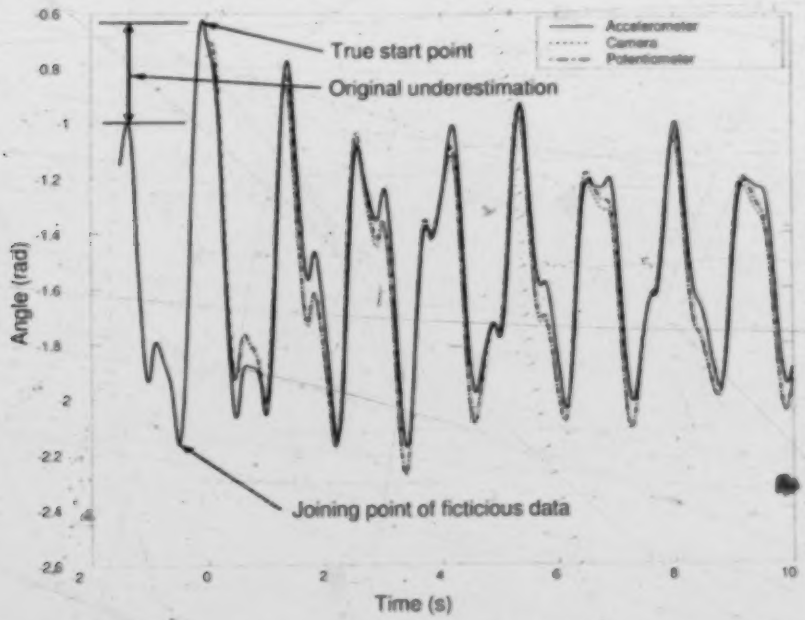

Figure 4.9: Upper-link orientation with the addition of ficticious data

The addition of fictitious data appears to have improved the transient problem, and greatly reduced error in this parameter. Initial angle matching has been made possible but there is still some over estimation following the large initial angular change. Aside from this discrepancy the orientation data is within 0.10 *rad* (5.7 deg) or less than 10% of the full scale range. Tables 4.1 and 4.2 show the correlation coefficient (R), and root mean square errors (RMSE) for comparisons between the angular accelerations, angular velocities, and orientations obtained from accelerometers, potentiometers and high speed cameras for the upper and lower links. Although the potentiometers are considered the most accurate device for angular measurement, the accelerometer system is also compared with camera data. This was done since high speed cameras will be the only source of verification during crash testing. To ensure the camera system is reliable for determination of angular kinematics, the R and RMSE values

for a comparison between potentiometer and camera derived angular parameters were found. Since the results of this comparison were better than what was obtained when the potentiometers and accelerometers were compared, camera data can be considered a reliable verification source during the crash test experiment.

Table 4.1: R and RMSE angular coefficients for upper-link (2 g)

Accel vs. Pot	**angular acceleration**	**angular velocity**	**angle**
R	0.9729	0.9885	0.9686
RMSE	6.8331 $\frac{rad}{s^2}$	0.3183 $\frac{rad}{s}$	0.5605 rad
Accel vs. Cam	**angular acceleration**	**angular velocity**	**angle**
R	0.9608	0.9888	0.9699
RMSE	7.4786 $\frac{rad}{s^2}$	0.3317 $\frac{rad}{s}$	0.5434 rad

Table 4.2: R and RMSE angular coefficients for lower-link (2 g)

Accel vs. Pot	**angular acceleration**	**angular velocity**	**angle**
R	0.9922	0.9984	0.9935
RMSE	5.4086 $\frac{rad}{s^2}$	0.2324 $\frac{rad}{s}$	0.0708 rad
Accel vs. Cam	**angular acceleration**	**angular velocity**	**angle**
R	0.9988	0.9982	0.9926
RMSE	2.6718 $\frac{rad}{s^2}$	0.2451 $\frac{rad}{s}$	0.0774 rad

The correlation coefficient (R) is a measure of the relationship between two variables, while RMSE approximates the average error between them. The closer the value of R is to 1, the better the relationship between the compared variables. The results in Tables 4.1 and 4.2 show that there is a high correlation between the different systems when measuring angular parameters. In many of the plots it is difficult to distinguish between the different measurement systems. The average errors expressed as a percentage of range are all well under 10%, with the exception of upper-link orientation. However, the R and RMSE values for orientation in Table 4.1 are based on the data shown in Figure 4.5C. By adding 1.5 s of data prior to integration and filtering, the R and RMSE coefficients for accelerometers versus potentiometers improved to 0.9688 and 0.1000, while the coefficients for accelerometers versus cameras improved to 0.9720 and 0.0930 respectively. Based on these values, the error in upper-link orientation is less than 10% as well.

4.2.2 2 g Translational Measurements

The translational acceleration for the double pendulum joint was determined from then equation

$$\vec{a}_{joint/N} = \vec{a}_{1_{board1}/N} + \vec{\alpha}_N \times \vec{r}_N + \vec{\omega}_N \times (\vec{\omega}_N \times \vec{r}_N).$$

Where $\vec{a}_{1_{board1}}$ is the vector $\vec{a}_1$, as described in Chapter 2, from board 1, while α, and ω were determined from accelerometer measurements and $\vec{r}$ is the vector from accelerometer 1 on the upper link to the joint. This upper link is assumed to be the rigid body as discussed in Chapter 2. Because the joint is in-line with the accelerometers, there is only one component in the vector r. This term was derived from high speed camera data, however, it could have been measured directly. The joint's translational velocities and displacements were determined through single and double integration of the acceleration vector. As was the case with angular information, initial conditions for translational velocity and position were not preserved after integration. The initial velocity and acceleration were zero because the body is at rest prior to release, while the initial displacement was set to be zero. Although, in a global reference, the start position is not zero, subtracting the initial displacement gives position relative to the pendulums starting point which is what we desire. Also, because the equation above is based in a body fixed frame, the rotation matrix

$$[\mathbf{M}] = \begin{bmatrix} \cos\theta_{link1} & -\sin\theta_{link1} \\ \sin\theta_{link1} & \cos\theta_{link1} \end{bmatrix} [\mathbf{N1}],$$

which was derived in Chapter 2, was required to transform the translational kinematics to the global reference frame.

As was mentioned in the angular measurement section, high speed cameras directly measure position. This data was single and double differentiated to obtain translational velocities and accelerations to be compared with accelerometer output. Potentiometer data was not compared in this section because they were not set-up to directly measure translational parameters and, therefore, the cameras were a better standard. A comparison of translational kinematics will now be presented.

Figure 4.10 shows overlaid plots of translational X and Y accelerations obtained from accelerometers and high speed cameras. Figure 4.9A, which contains translational X-accelerations, appears to show good agreement between accelerometers and cameras, while Figure 4.9B, which compares translational Y-accelerations, shows some deviations. This is not surprising since the range of accelerations in the Y-direction are half of those in the X-direction, while the uncertainty in acceleration for either direction is close to the same (uncertainty in Y-direction is 80% of uncertainty in X-direction from Chapter 3). Therefore, the difference between cameras and accelerometers should be more noticeable in the Y-direction.

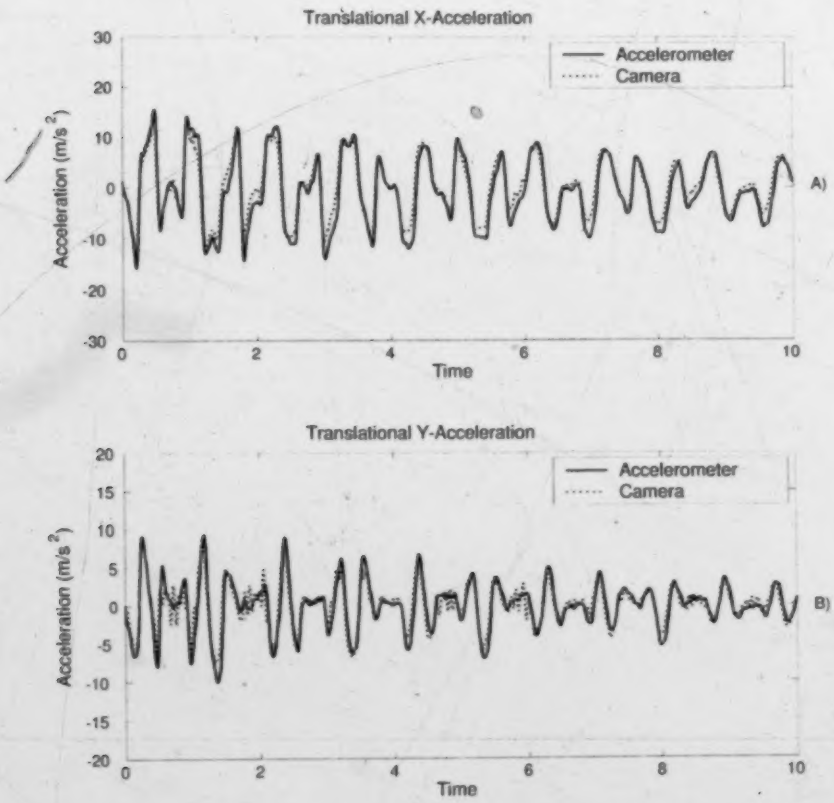

Figure 4.10: Translational X and Y accelerations of the pendulum joint (2 g)

Figure 4.11 compares the pendulum joints translational X and Y velocities. Figures 4.10A and 4.10B show a general agreement between the systems for both components of velocity. However, it was discussed earlier that the pendulum starts from rest and, therefore, the initial velocity should be zero but this does not appear to be the case. Both accelerometer signals, X and Y, appear to start just off 0 but match up with camera data after a short time. The data was not manually adjusted to zero since any adjustment would have introduced a constant offset throughout the data.

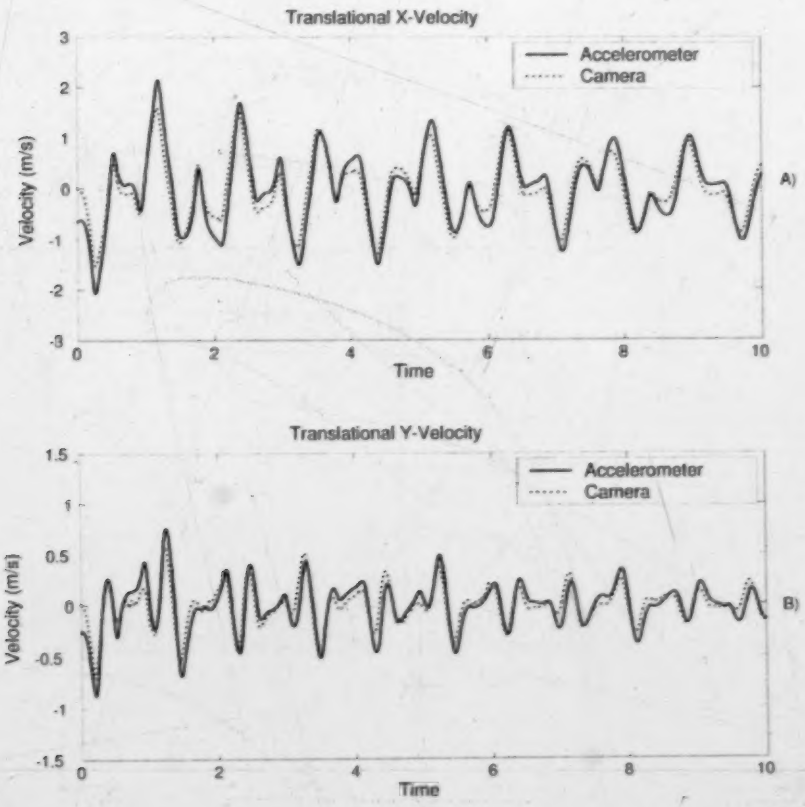

Figure 4.11: Translational X and Y velocities of the pendulum joint (2 g)

Figure 4.12 compares translational X and Y displacements. A somewhat consistent offset between accelerometer and camera output was seen in Figures 4.12A and 4.12B, which was similar to what occurred in the orientation plot from Figure 4.6. Again, filter transients have corrupted the early part of the signal making removal of the offset impossible by subtracting the initial value alone. Since the addition of fictitious data reduced the effect of filter transients in orientation, a similar approach was taken again. 1.5s of translational X and Y-acceleration data was duplicated and placed at the start of each signal prior to integration. Figure 4.13 shows the new displacement data.

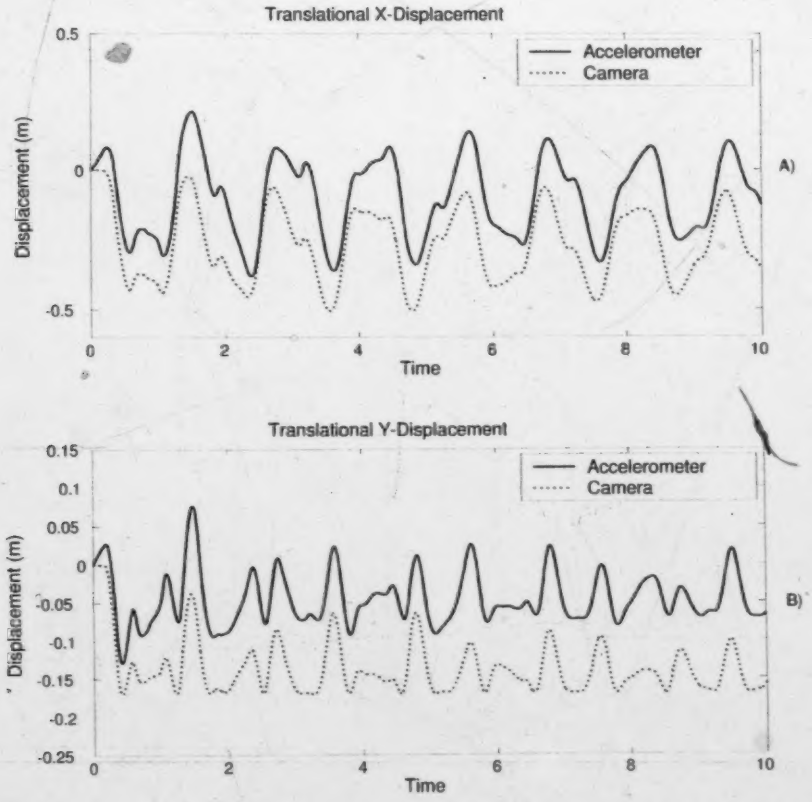

Figure 4.12: Translational X and Y displacements of the pendulum joint (2 g)

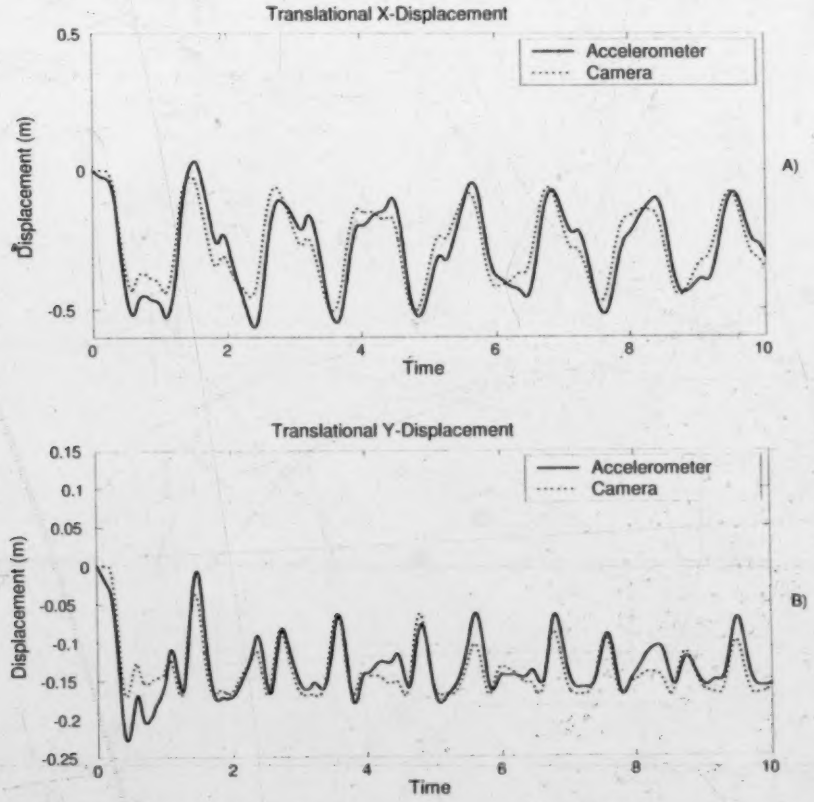

Figure 4.13: Translational X and Y displacements with the addition of ficticious data

The addition of fictitious data has improved the offset problem present in Figure 4.11. However, the agreement between accelerometer and camera output does not appear to be as good as the other parameters that have been discussed thus far. Also, the drift has not been removed entirely from the translational Y-displacement which deviates after 2 s. As was the case with translational acceleration, more noticeable discrepancy was expected in the Y-direction since uncertainties in both directions are close to the same, but the range of motion in the X-direction is much larger. Table 4.3 shows the R and RMSE coefficients for comparisons between translational X and Y acceleration, velocity and displacement obtained from accelerometers and cameras.

The R coefficients, and RMSE values, demonstrate mostly good agreement for all translational variables except displacement. However, since the system is being designed for the analysis of head and jaw kinematics during rear impact, the time period we are interested in is the initial 0.5 s. During this time period the agreement

Table 4.3: R and RMSE translational coefficients for pendulum joint (2 g)

X-Direct (Accel vs. Cam)	acceleration	velocity	displacement
R	0.9713	0.9409	0.9039
RMSE	1.9463 $\frac{m}{s^2}$	0.2576 $\frac{m}{s}$	0.0695 m
Y-Direct (Accel vs. Cam)	**acceleration**	**velocity**	**displacement**
R	0.9079	0.8881	0.8555
RMSE	1.3391 $\frac{m}{s^2}$	0.1025 $\frac{m}{s}$	0.0389 m

between accelerometer and camera displacement output is better than the signal as a whole. The error, expressed as a percentage of the range, for position measurement with accelerometers in the X-direction during the first 0.5 s ranged from 0-13.5% with the error not exceeding 5% for the first 300 ms, while the error in the Y-direction ranged from 0-14%, and did not exceed 10.5% for the first 300 ms. Average errors, or RSME values, for acceleration and velocity are under 10% when expressed as a percentage of range.

4.2.3 10 g Angular Measurements

The same procedure used to determine angular variables from 2 g acceleration measurements was also applied to the 10 g measurements. Angular accelerations were measured directly while angular velocity and displacement were found through integration. Although it was shown in Chapter 3 that we should be able to determine static angles within approximately 4 deg, much higher error was seen in practical application. For this reason, the initial angle was determined from potentiometer data. The primary interest here was to determine how much using accelerometers with decreased sensitivity and, thus, reduced measurement resolution, would affect kinematic measurements during the same motion.

Figure 4.14 plots accelerometer signals from the two accelerometers used to determine angular acceleration. A difference of nearly 6 $\frac{m}{s^2}$ can be seen at time 0 between the two data sets. This substantial difference is caused by accelerometer bias, which is approximately 10× higher than was predicted in Chapter 3. Variance in accelerometer bias was noticed during, both 2 g and 10 g testing, and no definite explanation was uncovered. Since NullLevels are subtracted from the accelerometer signals prior to converting the voltages to accelerations (this procedure is shown in Chapter 2), an error in NullLevels was expected to be the cause the bias problem. However, upon re-calibration, the NullLevels were nearly the same. Some other possible explanations for the bias issue are stray voltages that may be the result of board construction, since they were not assembled professionally, or the data acquisition system itself. However,

I am not knowledgeable enough in the construction of the system to be certain. As a result of this offset, large DC values are expected in the angular acceleration data.

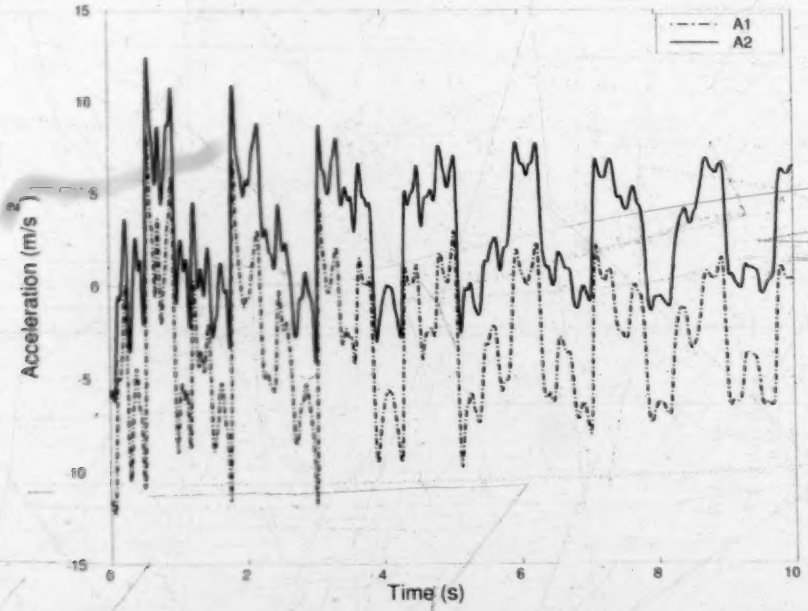

Figure 4.14: 10 g parallel accelerometer signals from upper-link during double pendulum motion

Figures 4.15 and 4.16 show the full and zoomed frequency spectrums for upper and lower link angular acceleration measurements with 10 g accelerometers. The DC offsets are 6-10× the magnitude of the next largest frequency component. As was the case in the 2 g experiment, initial conditions will be used to remove part of the offset, and hopefully reduce the uncertainty to an acceptable level. A comparison of angular parameters obtained from the different devices will now be presented. Since the procedure for determining two-dimensional kinematics with the 10 g system is the same as it was for the 2 g system (addition of fictitious data etc.), only final results will be shown.

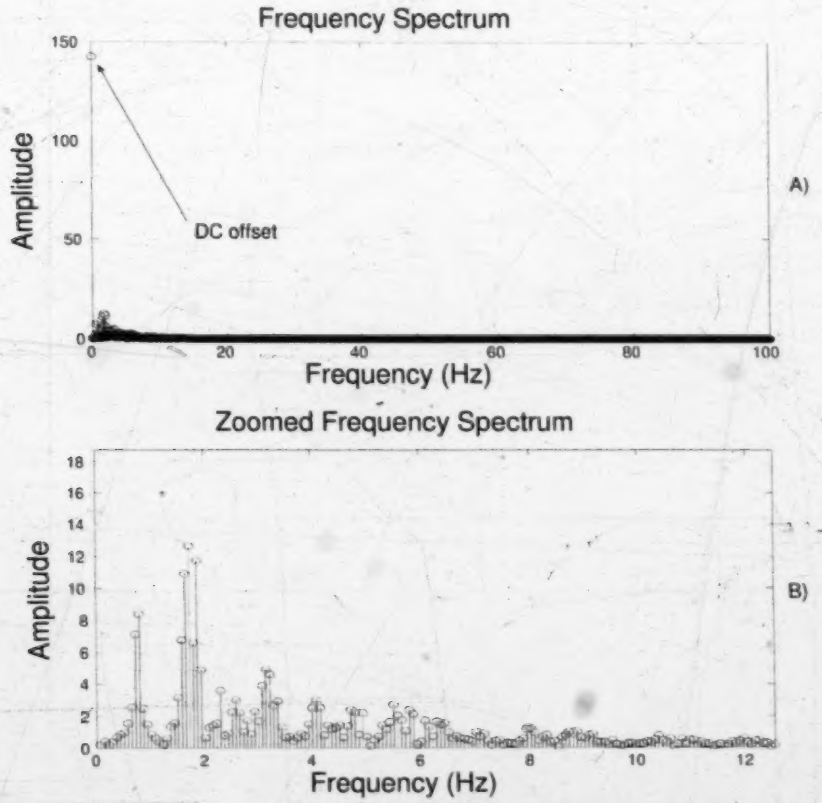

Figure 4.15: Frequency components of the upper-link's angular acceleration (10 g)

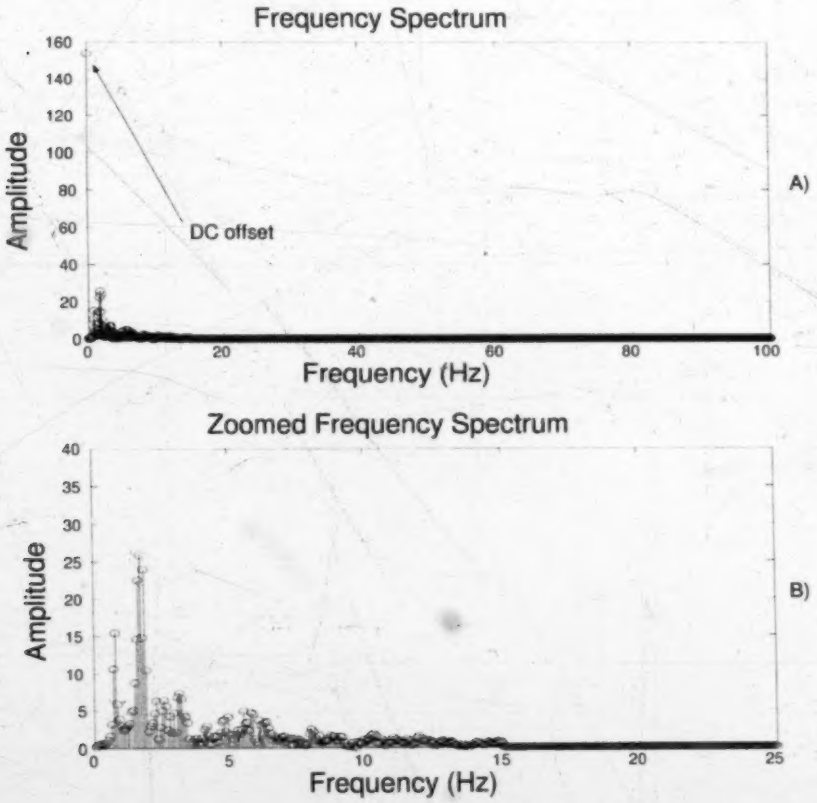

Figure 4.16: Frequency components of the lower-link's angular acceleration (10 g)

Figures 4.17 and 4.18 show comparisons of angular accelerations, velocities and displacements for the upper and lower links which were obtained from 10 g accelerometers, cameras and potentiometers. The plots show good agreement for the kinematic parameters obtained by all three measurement devices. The large DC values, which were shown in Figures 4.15 and 4.16, were mostly removed by subtracting the initial angular acceleration value, since the pendulum started from rest. Although the uncertainty in accelerometer measurements was much larger than expected, it does not appear to have a large effect on angular kinematics. As was necessary in the 2 g case, the initial 1.5 s of angular acceleration data for the upper link was duplicated and placed at the start of the signal prior to integration. This reduced the effects of filter transients on the orientation information and allowed the offset to be removed by adding the initial angle. Based on the analysis in Chapter 3, the uncertainties in the angular parameters were expected to be only slightly worse than those obtained with the 2 g system. The additional uncertainty was caused by the large DC value

that resulted from accelerometer bias.

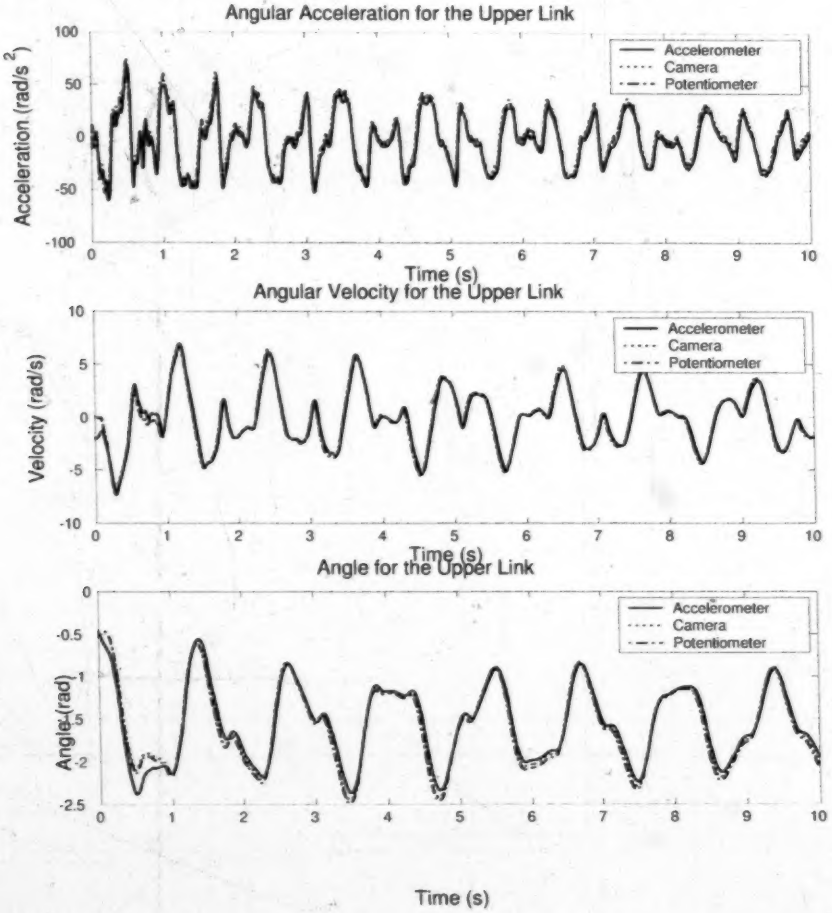

Figure 4.17: Angular kinematic variable comparison for the upper-link (10 g)

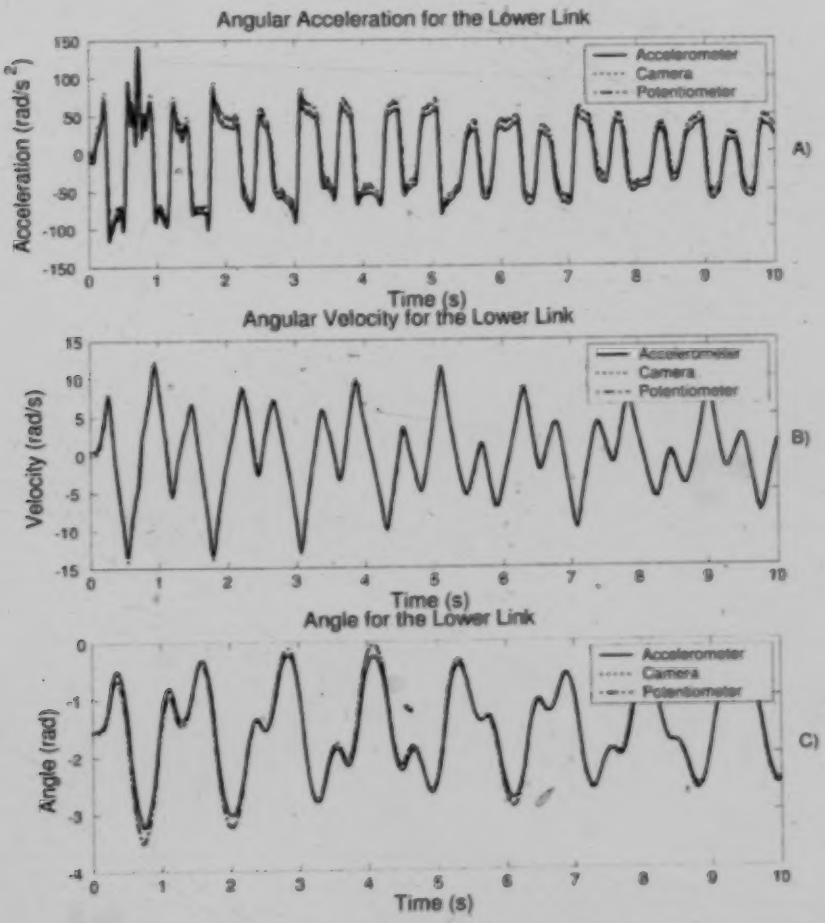

Figure 4.18: Angular kinematic variable comparison for the lower link (10 g)

Tables 4.4 and 4.5 show R and RMSE values for comparisons between kinematic parameters obtained from the different devices for both upper and lower links.

Table 4.4: R and RMSE angular coefficients for upper link (10 g)

Accel vs. Pot	**angular acceleration**	**angular velocity**	**angle**
R	0.9852	0.9906	0.9831
RMSE	$5.6621\frac{rad}{s^2}$	$0.3580\frac{rad}{s}$	$0.0950rad$
Accel vs. Cam	**angular acceleration**	**angular velocity**	**angle**
R	0.9920	0.9913	0.9843
RMSE*	$4.9100\frac{rad}{s^2}$	$0.3580\frac{rad}{s}$	$0.0822rad$

These results are similar to what was obtained with the 2 g accelerometers. The

Table 4.5: R and RMSE angular coefficients for lower link (10 g)

Accel vs. Pot	**angular acceleration**	**angular velocity**	**angle**
R	0.9840	0.9986	0.9914
RMSE	$11.6623\frac{rad}{s^2}$	$0.3105\frac{rad}{s}$	$0.1150 rad$
Accel vs. Cam	**angular acceleration**	**angular velocity**	**angle**
R	0.9898	0.9990	0.9923
RMSE	$11.6296\frac{rad}{s^2}$	$0.3021\frac{rad}{s}$	$0.1067 rad$

average error for the lower link angular acceleration is noticeably larger than the upper-link. A somewhat consistent difference between the accelerometers and verification devices can be seen in Figure 4.18A, which was removed by the application of a high-pass filter in the angular velocity and displacement plots. This is typically caused by bias error, which we attempted to remove by subtracting the initial value. However, some difference is still present, which increased the root mean square error for the lower link. As expected, the decrease in sensitivity and system resolution does not appear to have had a large effect on the measurement of angular kinematics. Next, the ability of the 10 g accelerometers for translational measurement was assessed.

4.2.4 10 g Translational Measurements

The same approach used to determine translational kinematics based on 2 g accelerometer measurements was also used in this section. Translational acceleration was found by applying Equation 2.2, while velocity and displacement were found through integration. Once again only final results will be presented.

Figure 4.19 shows translational X and Y accelerations. Although the accelerometer and camera data does show similar trends, the agreement between the different devices does not appear to be as good as the 2 g accelerometers provided. Since the translational acceleration components were found by combining translational accelerations of a point on the body, which was obtained from a single accelerometer, with the angular acceleration and velocity components, one of these parameters must be the cause of the difference. However, in the earlier section it was determined that there is very little difference between angular parameters obtained with either the 10 g or 2 g accelerometers, therefore, the problem must be caused by the single accelerometer output. This is not surprising since the uncertainty in 10 g accelerometer measurements was much higher than predicted in Chapter 3, which is evident when Figures 4.3 and 4.14 are compared.

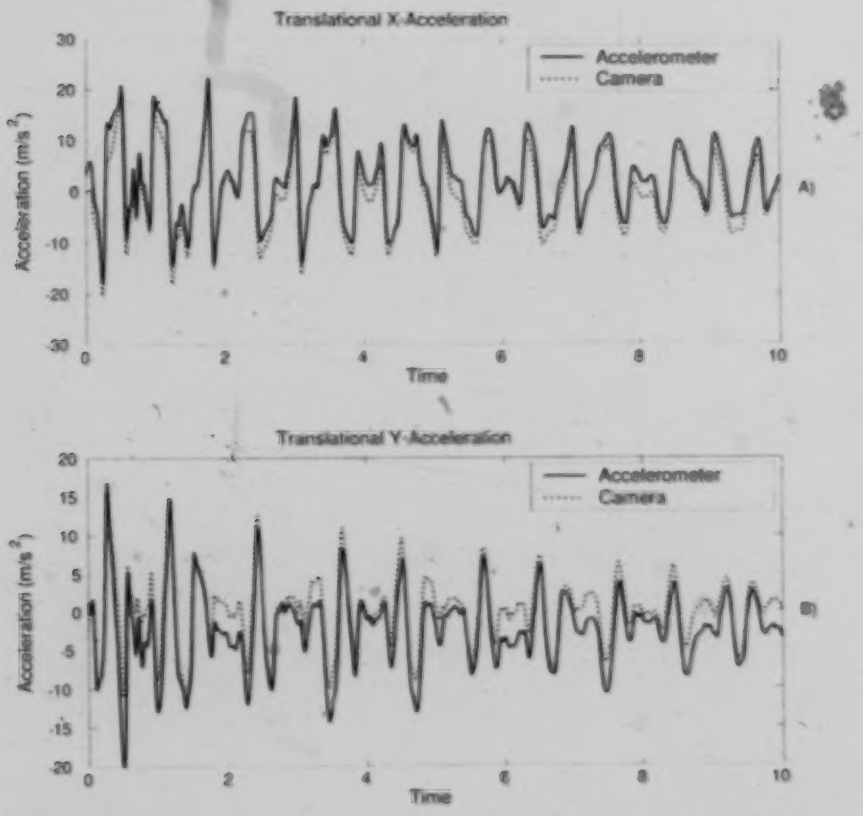

Figure 4.19: Translational X and Y accelerations of the pendulum joint (10 g)

Figure 4.20A compares translational velocity in the X-direction, while 4.20B compares translational velocity in the Y-direction. The agreement between accelerometers and cameras appears to be better in the X-direction than the Y-direction. This trend was also seen in the 2 g experiment, and occurs here for the same reasons.

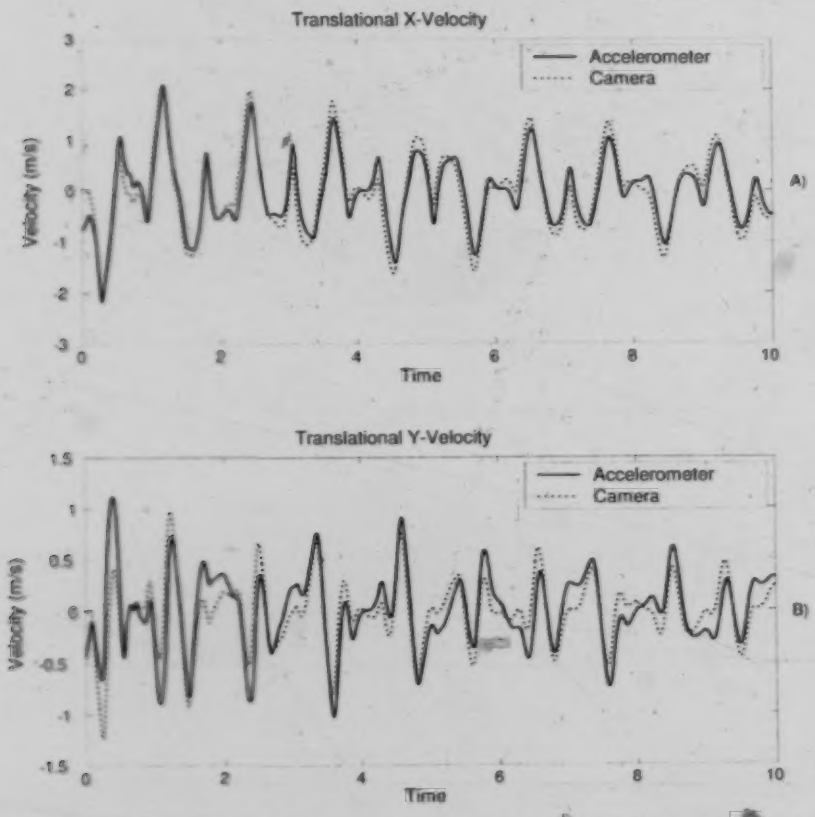

Figure 4.20: Translational X and Y velocities of the pendulum joint (10 g)

Figure 4.21 compares X and Y translational displacements. X-displacement, which is shown in plot 4.20A, appears to be much better than Y-displacement. This was expected for the same reasons discussed in the velocity section. Again 1.5 s of data was added to the start of both displacement data sets and although it did remove the offset in the X-direction, it was not effective for removing it in the Y-direction.

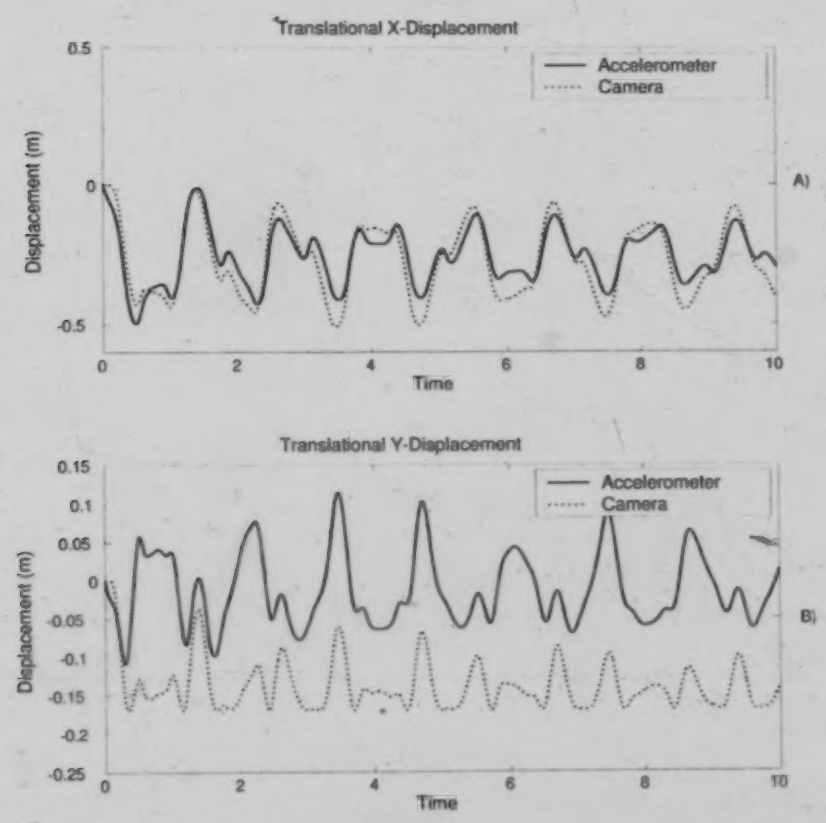

Figure 4.21: Translational X and Y displacements of the pendulum joint (10 g)

Tables 4.6 shows R and RMSE values for comparisons between accelerometer and camera output for the upper and lower links.

Table 4.6: R and RMSE translational coefficients for pendulum joint (10 g)

X-Direct (Accel vs. Cam)	**acceleration**	**velocity**	**displacement**
R	0.9715	0.9404	0.9185
RMSE	2.8293 $\frac{m}{s^2}$	0.2663 $\frac{m}{s}$	0.0586 m
Y-Direct (Accel vs. Cam)	**acceleration**	**velocity**	**displacement**
R	0.9408	0.7884	0.3662
RMSE	3.3183 $\frac{m}{s^2}$	0.2261 $\frac{m}{s}$	0.1335 m

Based on the coefficients shown above there is better agreement between the measurement devices in the X-direction than the Y-direction. In fact, the results in R and RMSE values for the kinematic parameters in the X-direction are very close to what was obtained with the 2 g accelerometers. The correlation in translational dis-

placement for both directions appears to be poor based on the statistical methods used above. However, if we look at the first 0.5 s and express the error as a percentage of the displacement range, as was done in the 2 g case, then error for X-displacement remains below 10% while error for Y-displacement still reaches 90%. The Y-displacement data becomes unreliable after approximately 300 ms, when the error exceeds 25%. Based on the results from this experiment the 10 g accelerometer error was within 10% of the full scale range, with the exception of Y-displacement. Although the lack of sensitivity had more noticeable effects on measurements in the Y-direction, larger accelerations are expected during crash testing, which would decrease error when expressed as a percentage of range.

4.3 Conclusions

In summary, it was observed that both the 2 g and 10 g accelerometer systems adequately measured, based on R and RMSE values, many aspects of the double pendulum motion. The accelerometer derived angular accelerations, velocities and displacements, for both 2 g and 10 g systems, were within 10% of the potentiometer and high speed camera results. However, angular displacement data for the upper link was greatly improved by initializing the high-pass filter, which was necessary because of the large initial movement that occurred when the pendulum was released. Removal of the filter transients allowed offsets to be eliminated by matching start values, as opposed to peak matching, so the accelerometer system could be used independently provided the initial angle of the body is known, or can be determined. This same issue may arise during crash testing since the impact is expected to cause large initial movements of the head and jaw. Although the 10 g accelerometers lack of sensitivity did not seem to have much of an effect on angular measurements, some differences were seen in translational kinematics. The large uncertainty in accelerometer measurements, which was assumed to be a result of some bias error for lack of a better explanation, caused an increase in translational acceleration uncertainty that was transferred to all other translational kinematic parameters. Despite this fact, a large difference in performance was not seen in the X-direction for acceleration, velocity and displacement. However, the 2 g accelerometer system was noticeably more accurate for measurements in the Y-direction. The largest difference was seen in Y-displacement where the 10 g accelerometers overestimated the camera output and showed only marginal agreement in the first 0.3 s, while the 2 g system was within 15% error, expressed as a percentage of range, for the first 0.5 s.

Based on the results obtained here, the systems are, for the most part, interchangeable for measurement of angular parameters. The 2 g system would be a better choice for measurement of translation, but since crash testing involves impact where accelerations in excess of 2 g's are a possibility, 10 g accelerometers may still be required. In the next chapter the performance of the 2 g and 10 g accelerometers during rotating and translating motion will be evaluated.

Chapter 5

Translating Pendulum Analysis

In this chapter, the results of measuring the 2-D kinematics of a translating pendulum, with 2 g and 10 g accelerometers, are reported. In the previous chapter we saw that both systems (2 g and 10 g) were able to measure the majority of kinematic parameters with acceptable accuracy. However, during rear-impact the head and jaw do not just rotate but also translate, therefore, the system's ability to measure this type of motion was used as the next step for verification. In this experiment, angular kinematics obtained from the accelerometers were verified with encoders and high speed cameras, while only high speed cameras were used to verify translational kinematics. Because neither system emerged as a clear choice for crash test analysis in the previous experiment, both 2 g and 10 g accelerometers were evaluated again and the effects of reduced sensitivity were assessed. The results presented in this section were obtained from separate tests with the 2 g and 10 g accelerometer systems.

5.1 Experimental Design

In this experiment a sinusoidally translating cart, which had a single pendulum suspended from it, was used as the test apparatus. The pendulum was specifically designed with an extension arm to more accurately simulate the crash test set-up where the point of interest is not in-line with the accelerometers. The pendulum is shown in Figure 5.1. Encoders monitored the orientation of the pendulum as well as the location of the cart along the track. Because the cart system was prefabricated the encoders, which had a built in power supply, did not need to be re-calibrated. However, they were tested to ensure they were operating properly. The accelerometer boards, which contained 2 g and 10 g accelerometers, were connected to a 5 V linear power supply and fixed to the pendulum. In this experiment, accelerometer ouputs

were not collected with the NIDAQ, instead they were relayed to the cart's built in D-Space data acquisition system and sampled at 2000 Hz. This higher sampling rate was required to catch the signal from the high speed cameras, since they were used to trigger data collection. Three high speed cameras, which were operating at 200 Hz, were calibrated for a 1 $m \times 1\ m \times 1\ m$ space to monitor pendulum motion. Reflective markers were placed at the point of translation, on the end of the extension piece, and on one accelerometer from each board. This set-up can be seen in Figures 5.1 and 5.2.

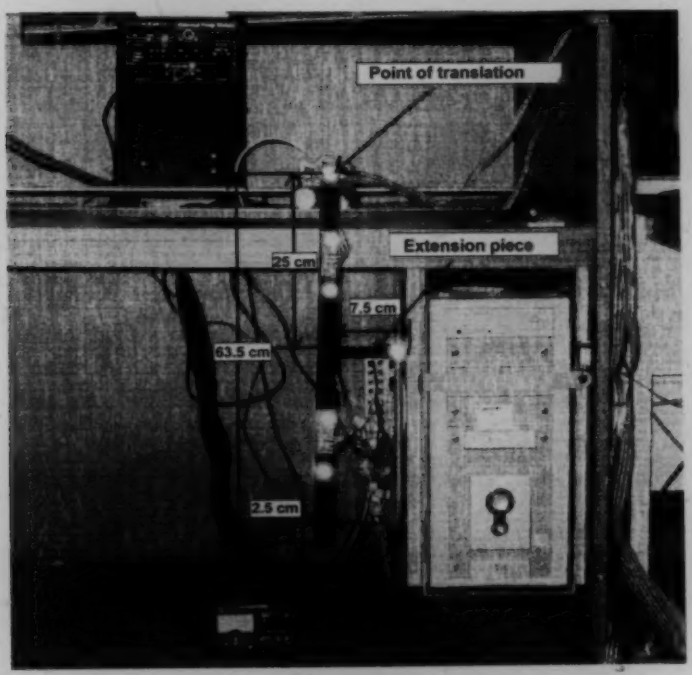

Figure 5.1: Fully instrumented pendulum

Figure 5.2: Translating pendulum test set-up

Data collection was triggered by manually starting the cameras, following the initiation of cart movement, and continued for a 5 s period. A block diagram, which was assembled in Simulink, was used in conjunction with a dspace interface to control the cart's motion and collect sensor output. The model allowed modification of the frequency and amplitude of the input sine wave. The input sine wave for this experiment had an amplitude of 0.1 m at a frequency of 1 Hz. Raw sensor outputs were low-pass filtered down to 15 Hz prior to any analysis. Camera output was collected, and converted to position information, with PCReflex software. All analysis software which was used to determine angular and translational kinematics, and compare the different systems was written in MATLAB. Integrated accelerometer data was pre-filtered with a 4^{th} order Butterworth filter (0.5 Hz cut-off), while differentiated camera and encoder data was smoothed with a 5^{th} order low-pass Butterworth filter with a 15 Hz cut-off. These filters were chosen for the same reasons explained in the previous chapter. Also, frequency spectrum and residual analysis was done, however, the plots are not shown. 2 g and 10 g accelerometer performance was evaluated in separate tests.

5.2 Discussion/Results

In this discussion, the performance of both types of accelerometers will be evaluated based on their abilities to measure angular and translational motion. The evaluation consists of comparing simultaneously recorded accelerometer, encoder, and high speed camera data. Although two accelerometer boards were attached to the pendulum, only the results from the board closest to the cart are presented. The second board was added to determine if a larger spacing between accelerometers would improve angular measurements, however, because the pendulum was not entirely rigid, the vibrations generated during swing corrupted the results. One thing to note is that the dspace data acquisition system, which was used in this experiment, has 16 bit resolution, while the NIDAQ system used in the previous chapter had only 12 bit resolution. This makes a significant difference since it improves both 2 g and 10 g system resolutions by more than 2× in the 2 g case, and more than 5× in the 10 g case. The uncertainty in 2 g accelerometer measurements improves from 17.4 mg (from Chapter 3) to 7.1 mg, while the uncertainty in 10 g accelerometer measurements improves from 51.0 mg to 9.6 mg. Based on these values, the results obtained from 2 g and 10 g systems are expected to be similar. Figure 5.3 shows the coordinate system established for this experiment.

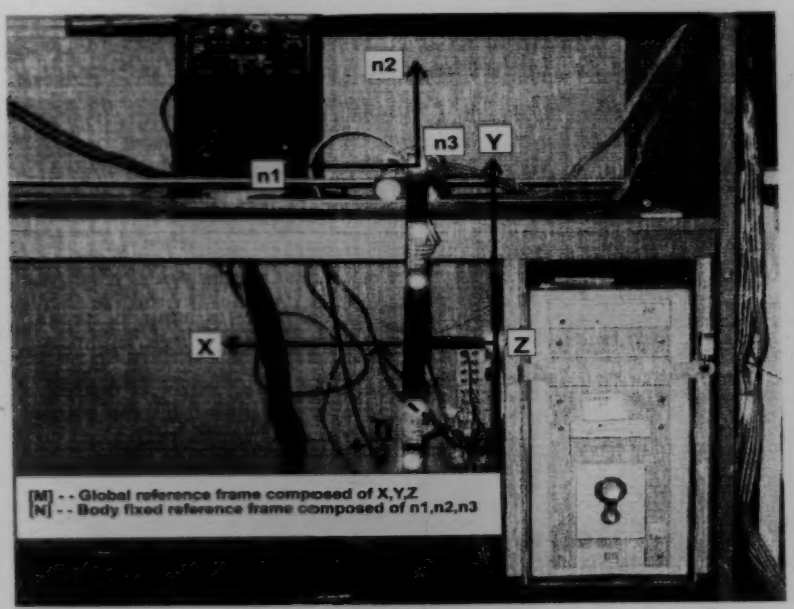

Figure 5.3: Translating pendulum coordinate system

[**M**] refers to the global reference frame, while [**N**] refers to the body fixed reference frame, as described in Chapter 2. In this experiment, translation is defined as relative to the start position of the marker on the extension piece. For angular measure, the vertical position is considered the zero angle.

5.2.1 2 g Angular Measurements

As was the case in the previous chapter, angular acceleration was measured directly while angular velocity and displacement were found through single and double integration. Although the pendulum does start from rest with the initial condition for all angular parameters being zero, manual triggering of data collection made it difficult to synchronize the start of data collection with the initiation of cart movement. To counter this problem, 1s of data was recorded prior to the start of the test. At t = -1 s, the pendulum's initial conditions would be zero while the conditions at t = 0 s, which corresponds to the start of the test, may not be zero. By initiating integration at t = -1 s, the non-zero start conditions were determined. High speed camera and encoder data was differentiated to obtain angular velocities and accelerations for comparison.

In the previous Chapter, raw accelerometer signal were plotted to show the relationship the time and frequency domains. In this Chapter, only the frequency spectrums will be shown. Figure 5.4 shows the frequency spectrum of the angular acceleration data obtained with the 2 g accelerometers. Since the uncertainty in accelerometer measure was greatly improved by the dspace data acquisition system, which was discussed earlier, a large DC offset was not anticipated. Upon inspection of Figure 5.4B, it is apparent that the amplitude of the zero frequency component is almost non-existent. The largest frequency component can be seen at 1 Hz, which results from the sine wave being input to the cart. Low uncertainty is expected in the angular parameters determined with this system.

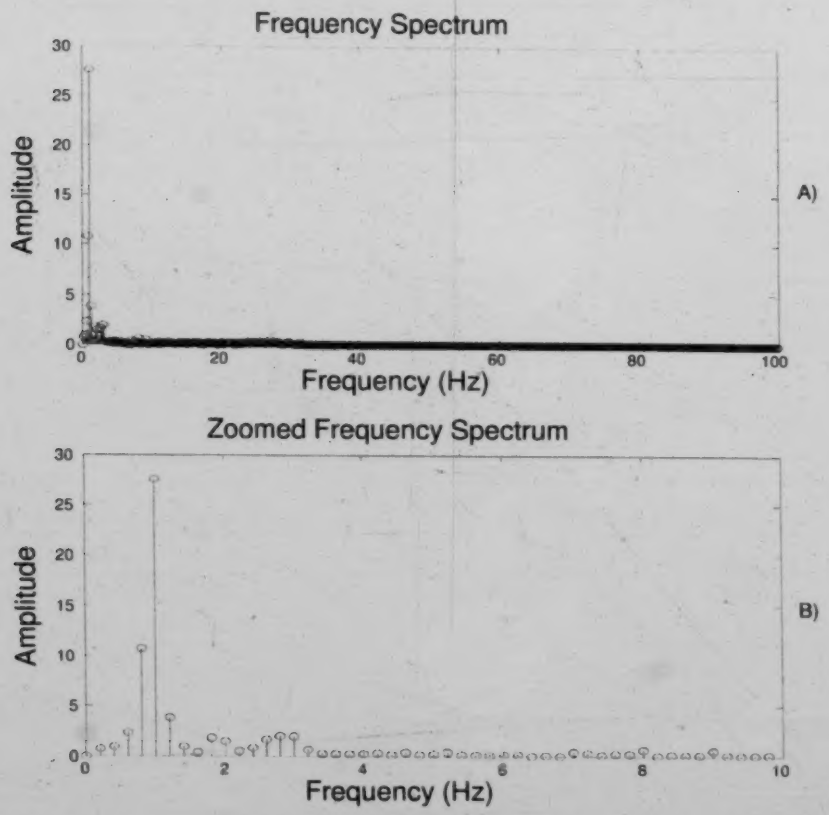

Figure 5.4: Frequency components of the translating pendulum's angular acceleration (2 g)

A comparison of the angular parameters obtained from the three different systems will now be presented. Figure 5.5 compares the angular accelerations, angular velocities and angular displacements obtained from the accelerometers, encoders and high speed cameras. Although there appears to be some high frequency noise at the peaks of the angular acceleration data, it was determined to be a characteristic of the movement since the trend is seen in all three devices. Since the noise occurs at the peaks, when the pendulum is changing directions, it is likely caused by the vibrations generated as a result of the pendulum not being entirely rigid. In the angular velocity and displacement plots, there is deviation of accelerometer data from high speed camera and encoder data, which appears to be caused by filter end transients. To determine if this was the case, the filter was applied to a 3.75 s section of the same data and the results were overlaid with the original 5 s signal. This is shown in Figure 5.6.

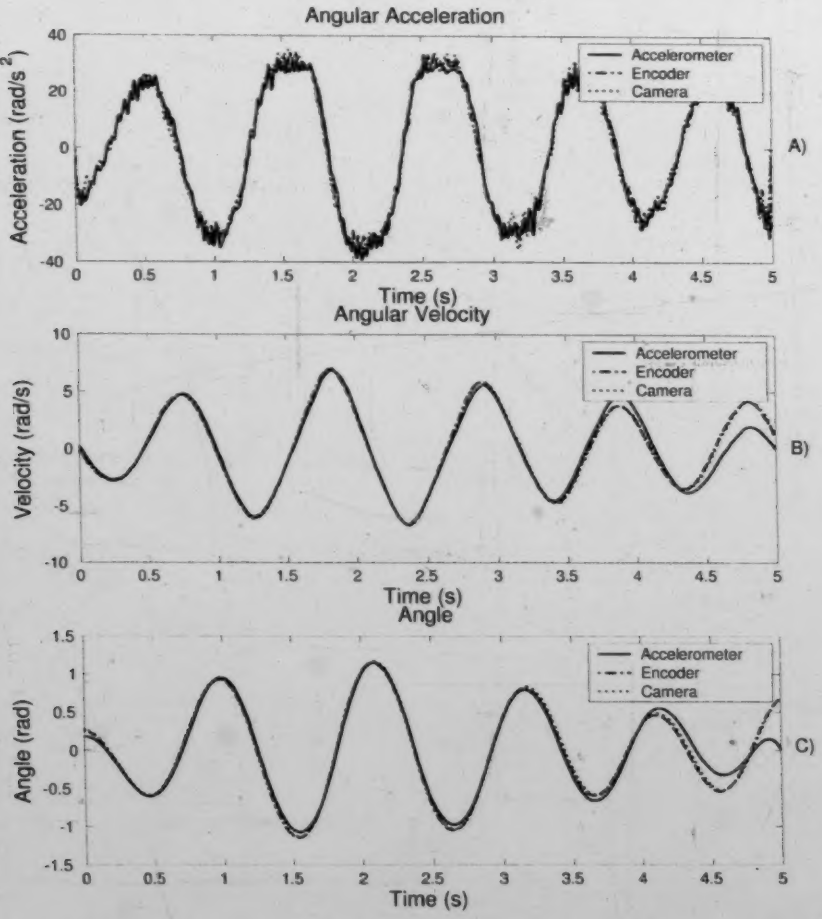

Figure 5.5: Translating pendulum angular kinematic variable comparison (2 g)

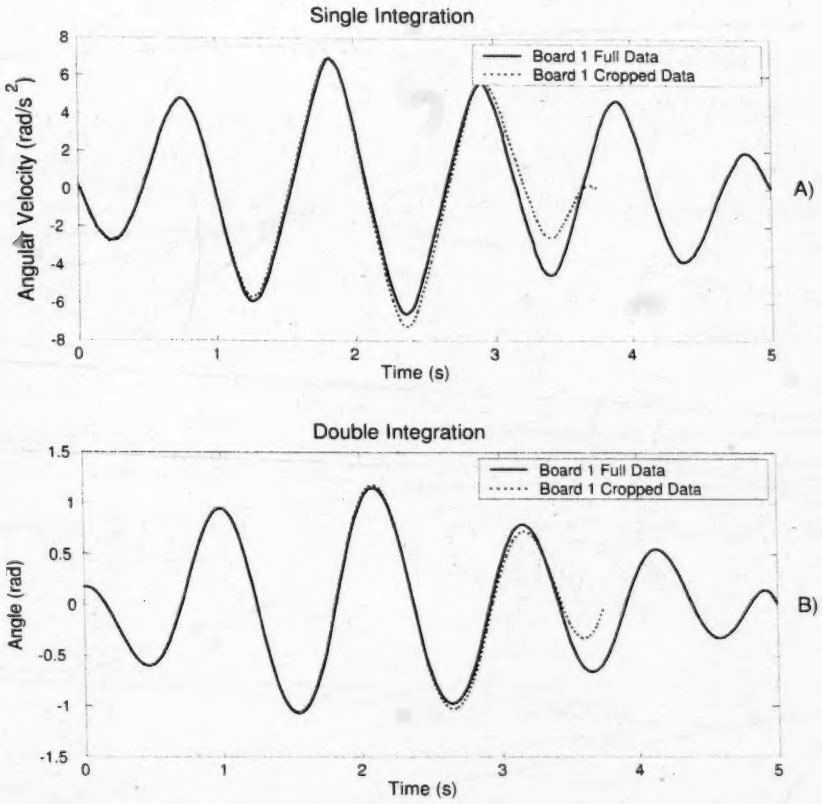

Figure 5.6: Comparison of high pass filtering full and partial data sets

As expected, the cropped data set, which refers to the 3.75 s of data, does not match the full data set. However, since the effects of the filter are seen only at the end of the output, and we are interested in the start, this may not be a problem. By setting the sample time to exceed the period of interest by a minimum of one second, the effects of the filter will not corrupt the important data. As was done for the double pendulum results, the correlation coefficient (R) and root mean square error (RMSE) have been determined based on the comparison between accelerometers with high speed cameras and encoders for all angular variables. The results are presented in Table 5.1.

Since the R value for all variables is close to 1, the signal shapes compare well. The average error seen in angular acceleration is noticeably lower than the double pendulum experiments, which is due to the increased resolution of the DAQ. However, the errors in omega and theta, based on the table above, are close to the same or higher when

Table 5.1: R and RMSE angular coefficients (2 g)

Accel vs. Encoder	**angular acceleration**	**angular velocity**	**angle**
R	0.9932	0.9802	0.9841
RMSE	2.5266 $\frac{rad}{s^2}$	0.7169 $\frac{rad}{s}$	0.1079 rad
Accel vs. Cam	**angular acceleration**	**angular velocity**	**angle**
R	0.9781	0.9791	0.9853
RMSE	4.5720 $\frac{rad}{s^2}$	0.7431 $\frac{rad}{s}$	0.1052 rad

compared with the previous chapter. It should be noted that the R and RMSE values for angular velocity and displacement are based on the data sets where underestimation occurred in the final 1.5 s, which was determined to be a result of the filter applied. If the both values were re-calculated based on the initial 3.5 seconds, improved results would be expected.

5.2.2 2 g Translational Measurements

The parameters that will be discussed in this section are the translational acceleration, velocity and displacement of a point on the translating pendulum's extension piece. In the double pendulum analysis, translational measurements were taken from the joint that connected the upper and lower links which was in-line with the accelerometers. For this experiment, the extension piece was added to the pendulum because it is a more accurate representation of the crash test set-up where the points we want to measure will not be in-line with the accelerometers. Because the initial accelerometer configuration in this experiment was the same as the previous chapter, determination of translational kinematics was done in the same way.

Also, camera output was single and double differentiated to obtain translational velocities and accelerations before being compared with the accelerometer output. Since the cameras directly measure translation of the marker on the extension piece, while the encoders are not set-up to do so, they are the only source of verification in this section. A comparison between accelerometers and high speed cameras for translational measurement of a translating and rotating pendulum will now be presented.

Figure 5.7 compares translational X and Y accelerations obtained from accelerometer and camera output. Figure 5.7A, which compares translational X accelerations, shows mostly good agreement between the two devices. The additional noise in the accelerations determined from the accelerometers was caused by pendulum vibrations, which were the result of the pendulum not being entirely rigid. Also, there does

appear to be some deviation in the last 1.5 s of the data set. This is not surprising since determination of translational accelerations required the use of angular velocities and displacements that showed a similar pattern. Figure 5.8 shows a longer duration test of the same motion.

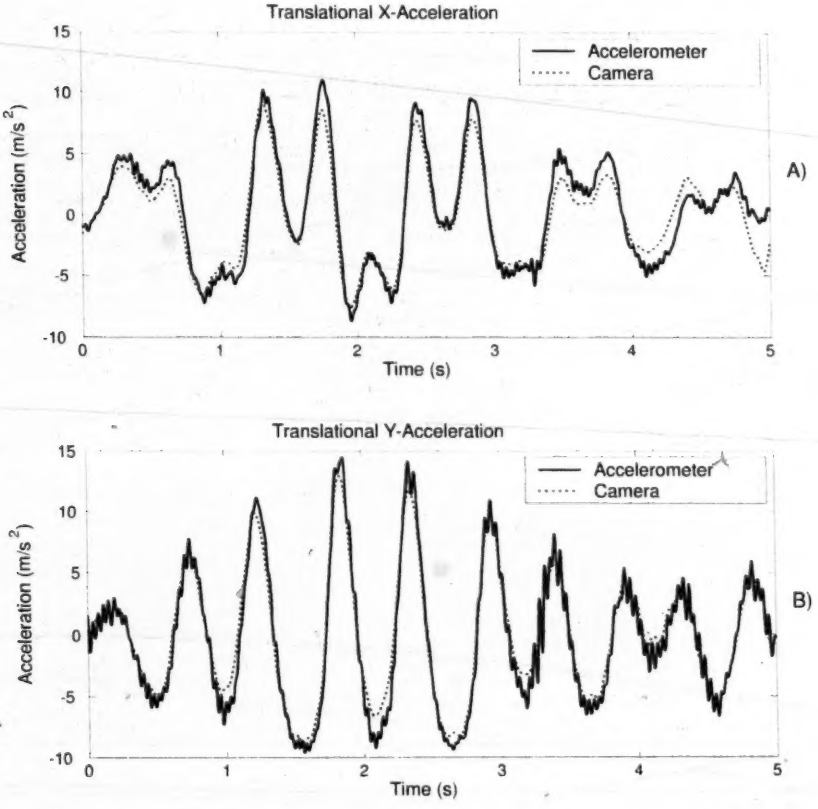

Figure 5.7: Translational X and Y accelerations of the extension piece (2 g)

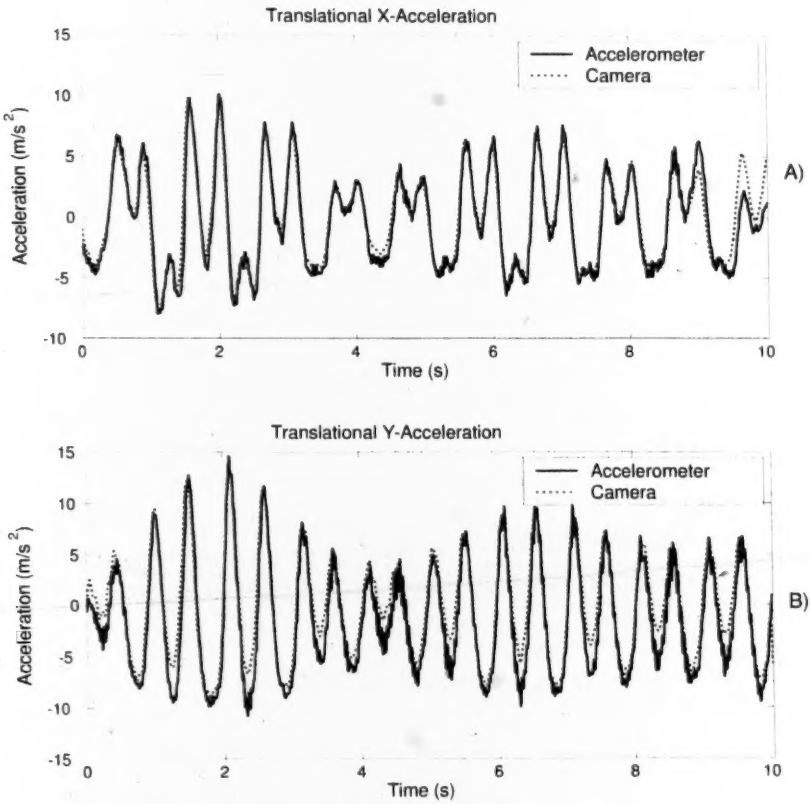

Figure 5.8: Translational X and Y accelerations of the extension piece during a longer duration test (2 g)

Again the signal does not begin to deviate until the final 1.0 to 1.5 seconds of the data set, which is consistent with what occurred in the angular velocity and displacement plot. The comparison of translational Y-acceleration, which is shown in Figures 5.7B and 5.8B, shows better agreement than was seen in the translational X-acceleration plots. Based on the analysis in Chapter 3, larger uncertainty is expected in the X-direction than the Y-direction. Also, the accelerations in the Y-direction fill more of the accelerometer range than those measured in the X-direction. Both of these factors contribute to the additional deviation seen in Figures 5.7A and 5.8A.

Figure 5.9 shows overlaid plots of translational X and Y velocities which were obtained from accelerometers and high speed cameras. The results shown in these plots are very similar to what was seen in Figure 5.7. The accelerometers deviate from the cameras in the final 1.5 seconds of Figure 5.9A while no deviation is seen in

Figure 5.9B. Aside from the final 1.5 seconds of data, the discrepancies in X and Y-velocities determined from the accelerometers with those from the cameras is similar. This was expected since the range of velocities in either direction is nearly the same, and the expected uncertainty in the X-direction is only slightly larger than in the Y-direction.

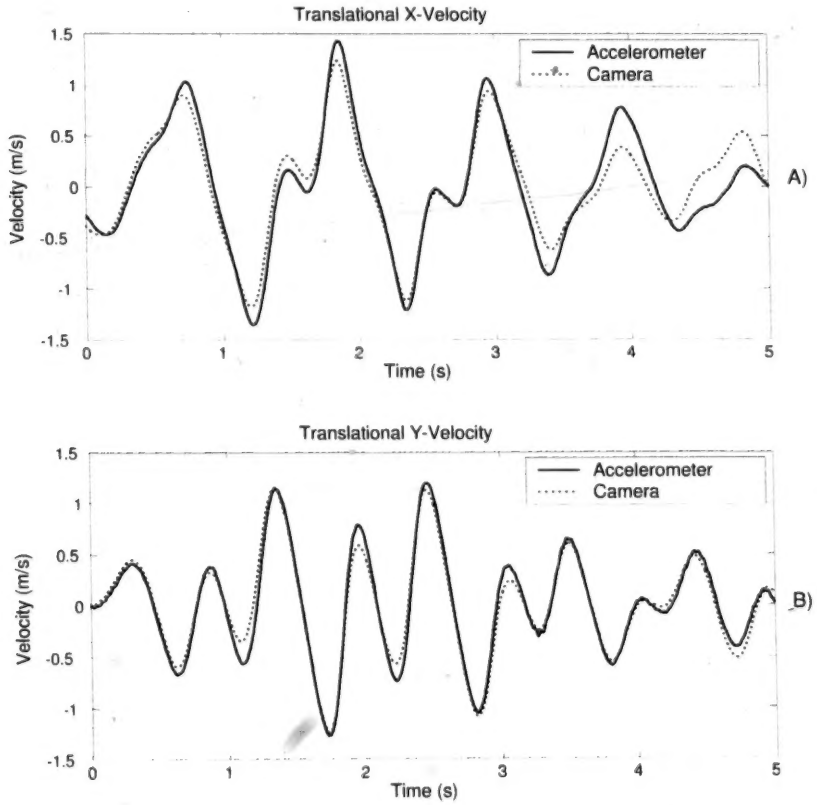

Figure 5.9: Translational X and Y velocities of the extension piece (2 g)

translational X and Y displacements are compared in Figure 5.10. The agreement between the two systems in Figure 5.10A, which compares X-displacement, appears to be good until approximately 3.5 s, where underestimation can be seen. This was expected since the same trend occurred in translational X-accleration and velocity. The accelerometer data in Figure 5.10B, which compares Y-displacement, underestimates the camera output from approximately 0.6 - 3.6 s. Since the dip that is seen in the Y-displacement data was not present in the Y-acceleration or Y-velocity data sets, the corruption is most likely a result of the filtering. However, the deviations seen in

Figure 5.10 may not be a problem. Since the system will ultimately be used for crash testing, only the first 0.5 s of data, which is intact, is of importance. R and RMSE values for comparison of the translational variables determined from the two devices are shown in Table 5.2.

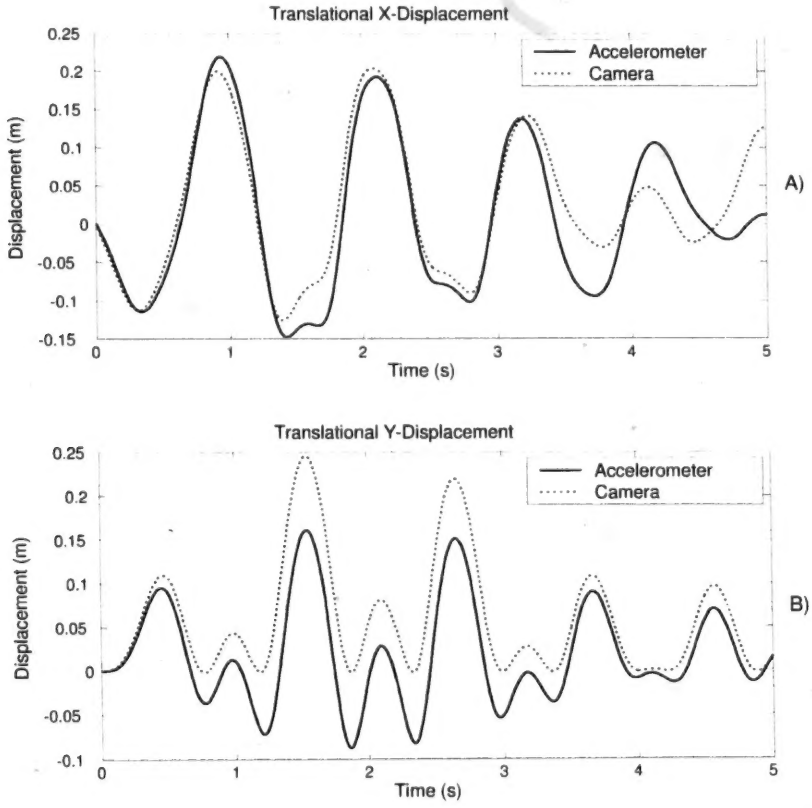

Figure 5.10: Translational X and Y displacements of the extension piece (2 g)

Table 5.2: R and RMSE translational coefficients (2 g)

X-Direct (Accel vs. Cam)	**acceleration**	**velocity**	**displacement**
R	0.9586	0.9530	0.9228
RMSE	1.3608 $\frac{m}{s^2}$	0.1815 $\frac{m}{s}$	0.0462 m
Y-Direct (Accel vs. Cam)	**acceleration**	**velocity**	**displacement**
R	0.9806	0.9831	0.8969
RMSE	1.1812 $\frac{m}{s^2}$	0.0928 $\frac{m}{s}$	0.0643 m

The R coefficients in the tables above show reasonable correlation between accelerometers and cameras for determination of translational variables. An R value below 0.9 is considered inadequate. The lowest R value occurred when comparing data sets for Y-displacement. However, this value is based on the full signal while our interest is primarily in the first 0.5 seconds, since it is the time-frame used during crash testing The accelerometer system error for determination of Y-displacement, expressed as a percentage of the entire Y-displacement range, for the first 0.5 seconds varies from 0-8% with the error not exceeding 5% for the first 300 milliseconds. The improved resolution of the dspace system decreased the average error for all the kinematic variables. If possible, a 16 bit data acquisition system should be used for the analysis.

5.2.3 10 g Angular Measurements

As was done in the double pendulum experiment, 10 g accelerometers were attached to the translating pendulum and subjected to the same motion as the 2 g accelerometers in the previous section. This was done to assess the effects of reduced system resolution on determination of kinematic variables. However, the difference between the systems is not expected to be as significant as was seen in Chapter 4.

Figure 5.11 shows the frequency spectrum for the 10 g accelerometer measurements of angular acceleration. As was the case with the 2 g system, the DC component is nearly 0. This is a much better result than what was obtained in the double pendulum experiment, and would lead us to believe that the bias problem seen in Chapter 4 was more likely caused by the data acquisition system, as opposed to the construction of the accelerometer boards.

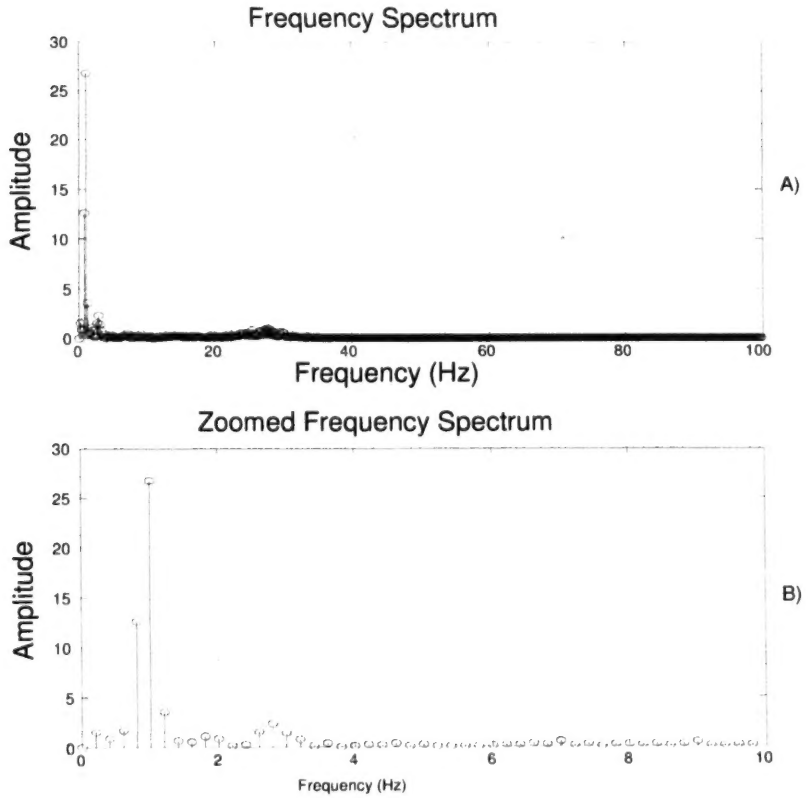

Figure 5.11: Frequency spectrum of translating pendulum's angular acceleration (10 g)

Figure 5.12 compares the angular parameters obtained from 10 g accelerometers, encoders, and high speed cameras. These results are very similar to what was obtained with the 2 g accelerometers during the translating pendulum test previously discussed. The angular accelerations from all three systems agree very well, while the accelerometer output deviates from the other two devices when measuring angular velocity and displacement. This was determined to be an effect of high-pass filtering the data. The R's and RMSE's for comparison of accelerometer results with those obtained from the encoders and high speed cameras have been determined and are shown in Table 5.3.

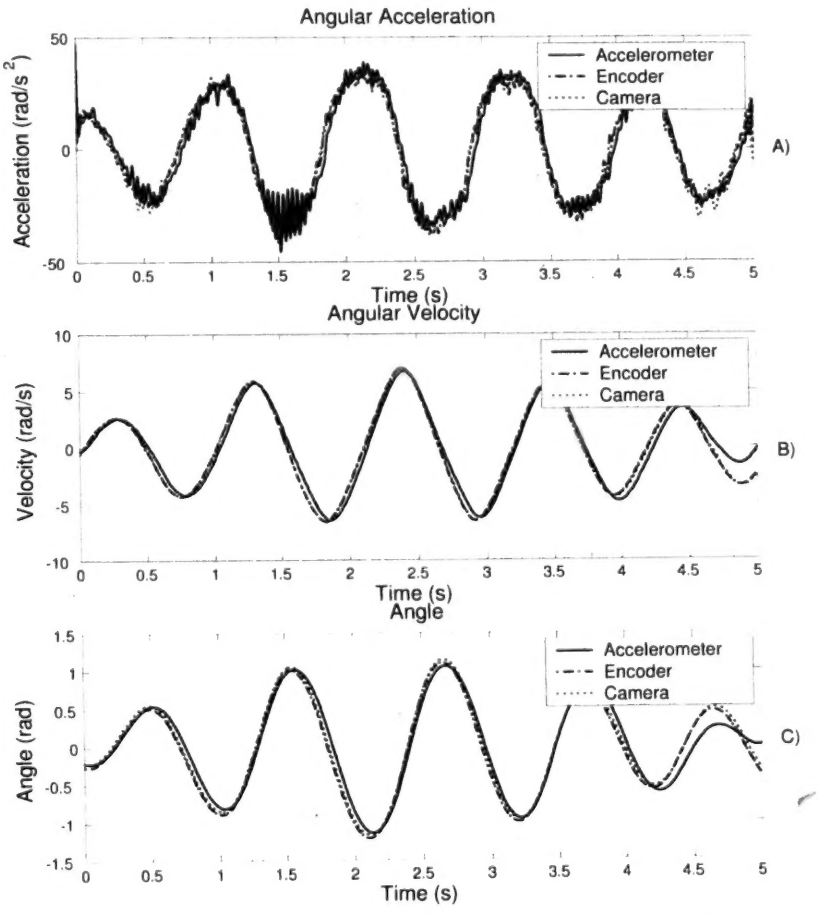

Figure 5.12: Translating pendulum angular kinematic variable comparison (10 g)

Table 5.3: R and RMSE angular coefficients (10 g)

Accel vs. Encoder	**angular acceleration**	**angular velocity**	**angle**
R	0.9713	0.9776	0.9756
RMSE	5.1515 $\frac{rad}{s^2}$	0.7457 $\frac{rad}{s}$	0.1296 rad
Accel vs. Cam	**angular acceleration**	**angular velocity**	**angle**
R	0.9545	0.9748	0.9754
RMSE	6.5617 $\frac{rad}{s^2}$	0.7959 $\frac{rad}{s}$	0.1312 rad

The largest difference when comparing the results above with the 2 g test is seen in angular acceleration. However, some discrepancy was expected based on the differing

system resolutions. Again, the high RMSE values for angular velocity and orientation are the result of the filter applied.

5.2.4 10 g Translational Measurements

The ability of the 10 g accelerometers to measure translational motion of the translating pendulum will now be discussed. Figure 5.13 shows overlaid plots of translational accelerations obtained from the camera and accelerometer systems. More deviation can be seen in the X-direction than the Y-direction, which was expected for the reasons mentioned earlier in this chapter.

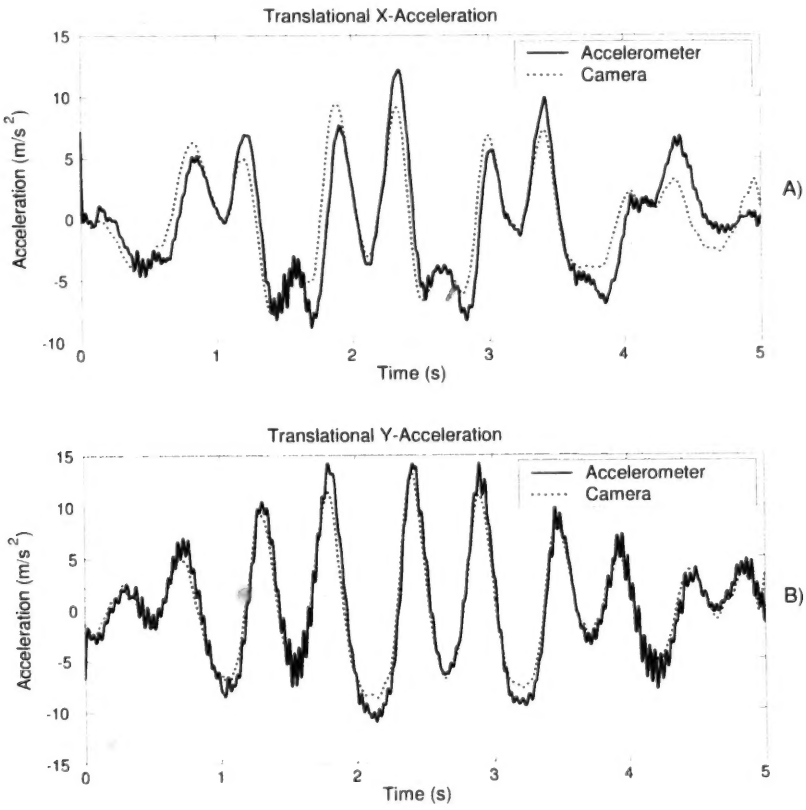

Figure 5.13: Translational X and Y accelerations of the extension piece (10 g)

Translational velocity plots are shown in Figure 5.14. The starting point for the X-velocity determined from the accelerometers and the starting point from the cameras do not line up. As was discussed earlier, 1s of data prior to the start of the test

was recorded in an effort to match non-zero start values, since data collection could not be initiated with cart movement. In this case, there appears to be some start-up transients, similar to what occurred in the double pendulum experiments, that cause underestimation. However, because the data is not being matched at time zero, an offset does not occur, and the rest of the data mostly aligns. There does appear to be more deviation in X-velocity than Y-velocity, which was not the case in the 2 g results. However, in the 2 g experiment, the range of velocities in both directions were nearly the same, while in this case the Y-velocity range is more than 0.5 $\frac{m}{s}$ larger, which is an approximate range increase of 20%. Therefore, any deviations will be more apparent. Also, the uncertainty in X-velocity is expected to be slightly larger than the uncertainty in Y-velocity based on the analysis in Chapter 3.

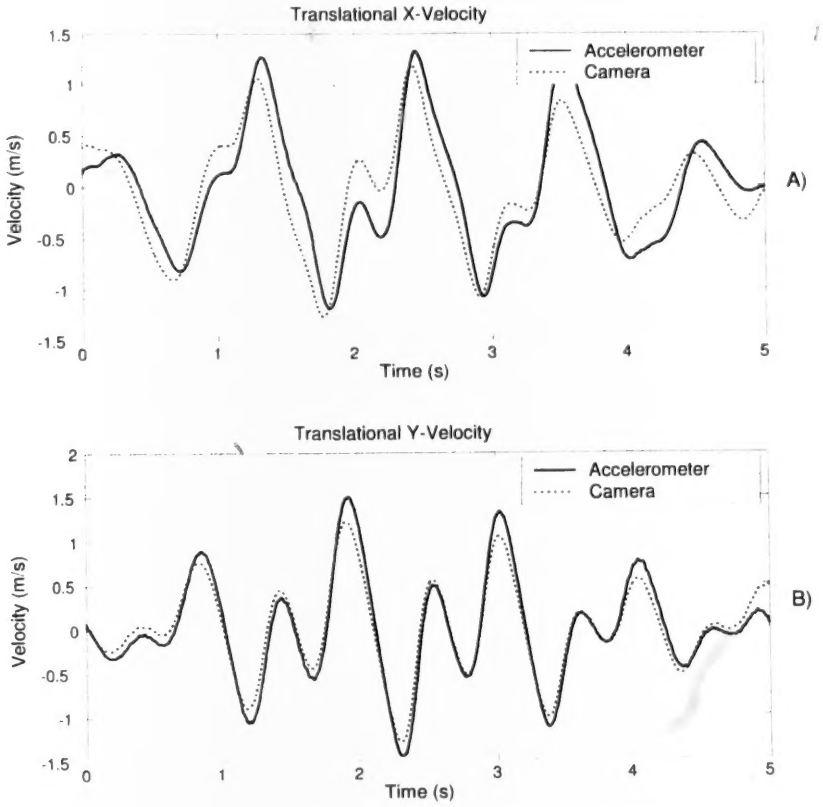

Figure 5.14: Translational X and Y velocities of the extension piece (10 g)

Figure 5.15 plots the X and Y displacements that were obtained from the accelerometer and camera systems. Although the deviation in X-displacement data sets

is more substantial than what was seen in the 2 g tests, the general shape of the signals is similar. The same trend seen in the 2 g derived Y-displacements is also present in the 10 g data. The high-pass filtering being applied appears to be corrupting some of the important frequency components. To determine if this is a filtering issue, the camera derived Y-displacements were passed through the same filter. The results are shown in Figure 5.16.

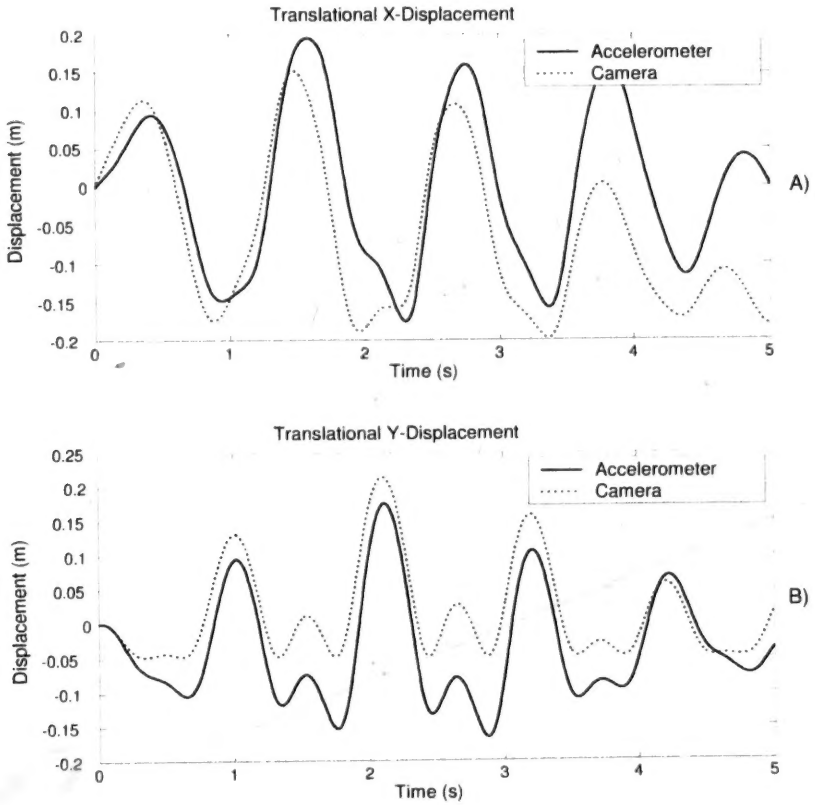

Figure 5.15: Translational X and Y displacements of the extension piece (10 g)

After passing the camera data through the filter, the agreement between the two devices improves substantially. A look at the frequency spectrum showed that the displacement data from that cameras has a DC component, which is removed by the filter. However, this component had to be removed to eliminate drift, and since the underestimation caused by the filter reaches approximately 3cm by 0.5 s, which is worse than what was obtained with the 2 g system, it is within 10% of the entire Y-displacement range. Table 5.5 contains the R's and RMSE's for comparison between

the translational variables determined by the different systems.

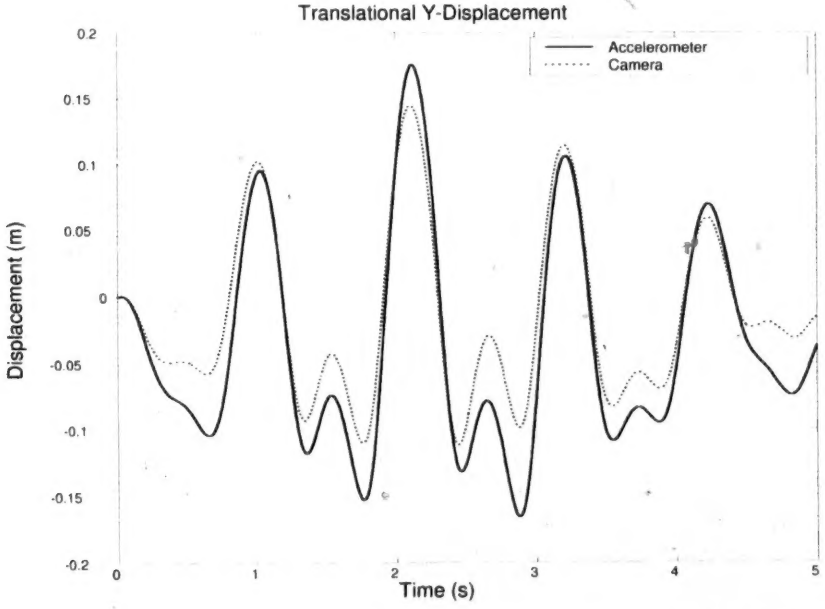

Figure 5.16: Comparison of camera and accelerometer derived Y-displacements passed through a 4th order high pass Butterworth filter with a 0.5 Hz cut-off

Table 5.4: R and RMSE translational coefficients (10 g)

X-Direct (Accel vs. Cam)	**acceleration**	**velocity**	**displacement**
R	0.8478	0.8413	0.6690
RMSE	2.1785 $\frac{m}{s^2}$	0.3053 $\frac{m}{s}$	0.1410 m
Y-Direct (Accel vs. Cam)	**acceleration**	**velocity**	**displacement**
R	0.9682	0.9726	0.9064
RMSE	1.4580 $\frac{m}{s^2}$	0.1359 $\frac{m}{s}$	0.0314 m

The results in the table above show poor correlation for acceleration, velocity and displacement in the X-direction. Underestimation in the final 1.0-1.5 s of data decreased these values. This was determined to be caused by the angular parameters that were used to derive the translational kinematics. Although there is a noticeable dip in the Y-displacement data, the error as a percentage of full range is only 0-9.5%, which is acceptable. Although the decreased system resolution has reduced the accuracy for determination of translational parameters, a noticeable difference is only

present in the Y-displacement data.

5.3 Conclusions

The results obtained in this experiment demonstrate that both 2 g and 10 g accelerometer systems can accurately determine the 2-D kinematics of a translating, rotating object. Although the agreement of the 2 g accelerometers with the encoders and high speed cameras was still better than what was obtained with the 10 g accelerometers, the difference between their performance was not as large as what was seen in the double pendulum experiment. One problem that was encountered with both systems during this experiment was underestimation of angular velocity and displacement in the final second of data, which was attributed to the application of high-pass filtering. However, since it is known that underestimation will occur, sampling for a time period of sufficient length will ensure that the transient effects occur after the period of interest.

A comparison of translational kinematics, determined by both systems, showed only a slight improvement was obtained with the 2 g accelerometers. Although the high-pass filter did not have to be initialized in this study, since the translating pendulum motion starts more gradually, its effects could still be seen. In both 2 g and 10 g trials, the accelerometer derived Y-displacements start in agreement with the cameras, underestimate them from approximately 0.5-4 s, and then move back up to agreement for the final 1s. However, the error for the first 0.5 s of motion, when expressed as a percentage of range, was still only about 10% for both systems, which is a better result than what was obtained with the double pendulum. Improved results were expected since the data acquisition system used had much higher resolution. If possible, a 16-bit data acquisition system should be used in the crash analysis.

Based on the results of this study, the difference between performance of the systems is not significant. Although improved R's and RMSE's were obtained when comparing the 2 g accelerometers with encoders and high speed cameras, the difference was not statistically significant. However, because crash testing involves impact, where accelerations in excess of 2 g's are a possibility, the 10 g accelerometers are a better choice. In the next chapter, accelerometers will be used to determine head and jaw kinematics during simulated rear-impact.

Chapter 6

Crash Test Analysis

In this chapter, the results of measuring the 2-D kinematics of the head and jaw during simulated rear-impact with 10 g accelerometers are reported. Because motion was initiated by impact, the accelerations experienced by the subject were expected to exceed 2 g's. Therefore, only 10 g accelerometers were used in this study. Also, the experiment was under time constraint since the sled was only available for a short period so only one system could be tested. Finally, the results of the translating pendulum tests showed little difference between the systems when measuring simultaneous translation and rotation. Since it was not feasible to instrument the subjects with potentiometers or encoders, verification of the 10 g accelerometer system, for angular and translational measurement, was done with high speed cameras only. The results presented in this section are from a single test where the subject experienced a change in velocity due to impact of 3 $\frac{km}{hr}$.

6.1 Experimental Set-Up

In this experiment, a subject was exposed to rear-impact via a car seat which was attached to a rolling track, and set in motion by a hydraulic ram. Head and jaw movement, which resulted from the impact, were measured with a 10 g accelerometer system. When the accelerometer boards were fixed to the head and jaw it was important that there was no relative motion between the board and the body it was attached to. This was important because the analysis is based on the assumption that the board and either head or jaw are part of the same rigid body. Since preventing relative motion when the accelerometers are attached to soft tissue is difficult, a tooth tray and mounting bracket system was employed. A dental impression tray was fitted with an inverted T-shaped mounting bracket, as seen in Figure 6.1, to which the accelerometers were bolted. To insure accurate 2-D measurements an attachment

jig, which was adjustable in three-dimensions, was used to hold the mounting bracket perpendicular to the tray during attachment.

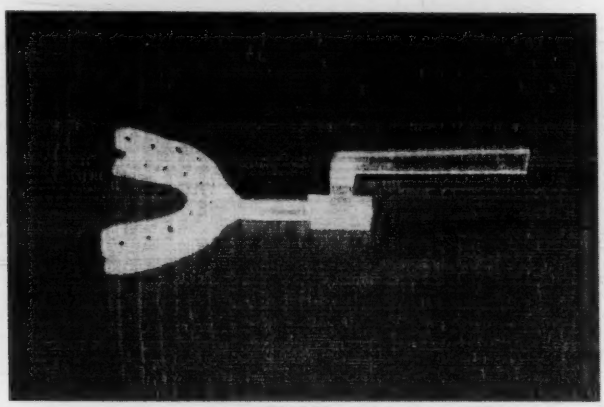

Figure 6.1: Mouth bracket for attachment of accelerometer board and reflective markers

Prior to placing the trays in the subject's mouth, the accelerometer boards were bolted to the brackets. The trays were then adhered to the upper and lower teeth using Polyvinylsiloxane Impression Material, which is normally used to take dental impressions. The boards were powered by a 5 V linear power supply and output from the sensors was relayed to the 12-bit NIDAQ system through 5m ribbon cables and a breakout box. Although a 16-bit systems would have been a better choice, I was unable to get access to one. Special headgear was worn to support the cables, and prevent their weight from affecting head and jaw movement. This is shown in Figure 6.2. Figure 6.3 shows the test set-up.

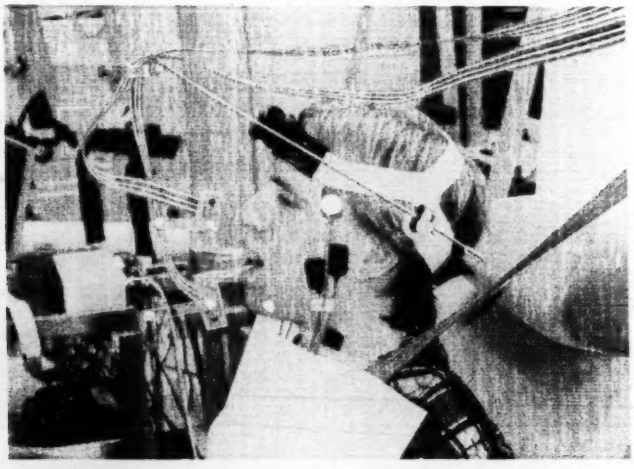

Figure 6.2: Fully instrumented subject

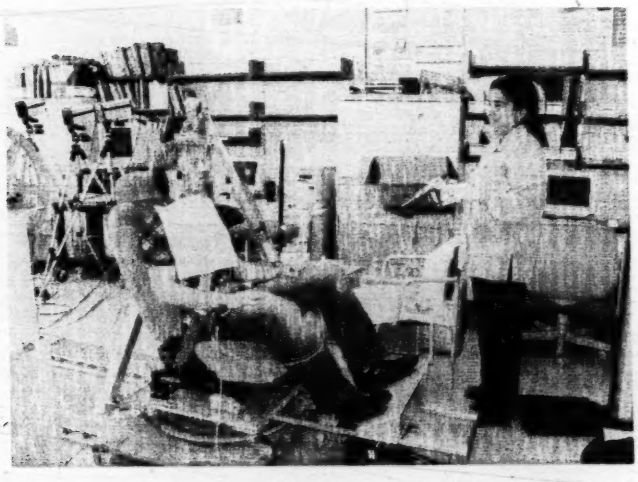

Figure 6.3: Test set-up including: seat, rolling track, high speed camera system and subject

Three high speed cameras, which sampled at 200 Hz, were positioned along the first 2 m of the 5 m test track since that is where the movement of interest was expected to occur. They were calibrated for a 2 m × 2 m × 1 m area to capture the subject's impending motion. Two reflective markers were placed on each mounting bracket, one was placed on the subject's temple, and another was placed on their chin. The position of these markers was used to determine the angular and translational kinematics of the head and jaw.

To begin the test, the instrumented subject was placed in the car seat and the hydraulic pressure was set. Accelerometer and high speed camera data collection was initiated by the firing of the hydraulic cylinder and continued for a 5 s period. Information from the NIDAQ was collected with MATLAB, at a rate of 4000 Hz, while camera output was collected with PCReflex software. A 4000 Hz sampling rate was used to prevent any aliasing as a result of impact. Although 4000 Hz may have been excessive, it was used since there was little restriction on how fast we could sample, while the implications of under-sampling would have caused us to lose important data. The determination of angular and translational parameters, as well as overlaying of data sets and statistical comparison of kinematic parameters obtained from the different systems, was done with MATLAB. The 10 g accelerometer system was set to record 1 s of data prior to the firing of the cylinder, and all data was low-pass filtered down to 15 Hz prior to any data analysis. Although this seems like a low cut-off for an impact study, the impact was not direct and the change in velocity was small. Frequency spectrum and residual analysis was performed to verify the cut-off, however, the plots are not shown. Although a number of trials were performed, only one subject's data will be presented. These results are representative of what was obtained with the system. The results of measuring head and jaw kinematics, with 10 g accelerometers, during low speed rear-impact will now be presented.

6.2 Discussion/Results

In this discussion the performance of the 10 g accelerometers for measuring 2-D angular and translational kinematics during rear-impact will be evaluated. The evaluation is based on comparison with high speed camera measurements. The coordinate system used in this experiment is shown in Figure 6.4.

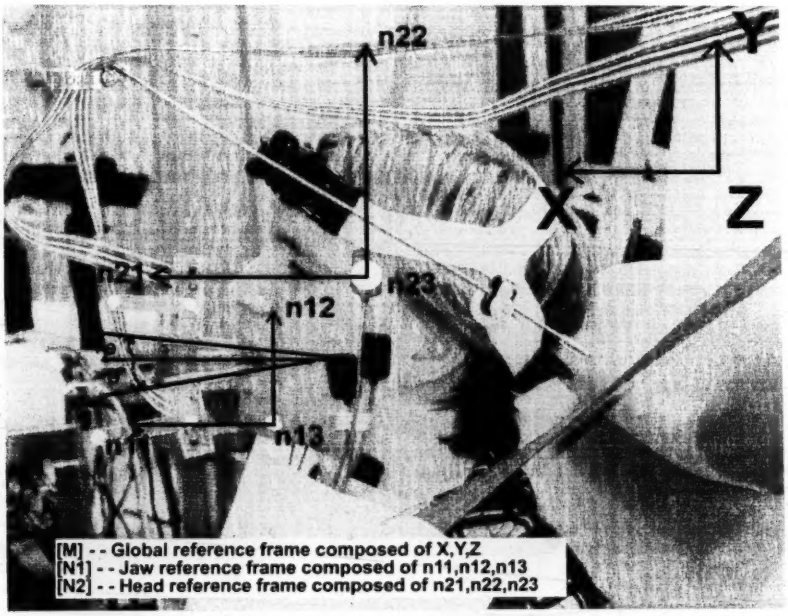

Figure 6.4: Coordinate system for crash test experiment

[**M**] refers to the global reference frame, while [**N1**] and [**N2**] refer to the head and jaw fixed reference frames. In this experiment, translation for the head and jaw is defined relative to the start position of the temple and chin markers, as shown in Figure 6.4. Rotation is defined relative to the horizontal axis, with clockwise rotation being positive.

6.2.1 Head and Jaw Angular Kinematics

As was done in the previous experiments, angular acceleration was measured directly while angular velocities and orientations were found through integration. Since the subject started from rest, the initial conditions for angular acceleration and velocity could be set to zero. However, the initial angular offset had to be determined from camera output to ensure the effects of gravity were removed. The positions of reflective markers, which were recorded with high speed cameras, were converted to orientations and then differentiated to obtain angular velocity and acceleration.

Figures 6.5 and 6.6 show the frequency spectrums for angular accelerations of the head and jaw with the initial value subtracted. Prior to subtraction, DC values similar to those seen in Chapter 4 were present. One noticeable difference in these

frequency spectrums compared to those in the pendulum experiments is that there is no frequency component with a substantially larger magnitude than the others. Also, there is a larger spread in the frequency content, which is mostly due to the frequency leakage that results from windowing.

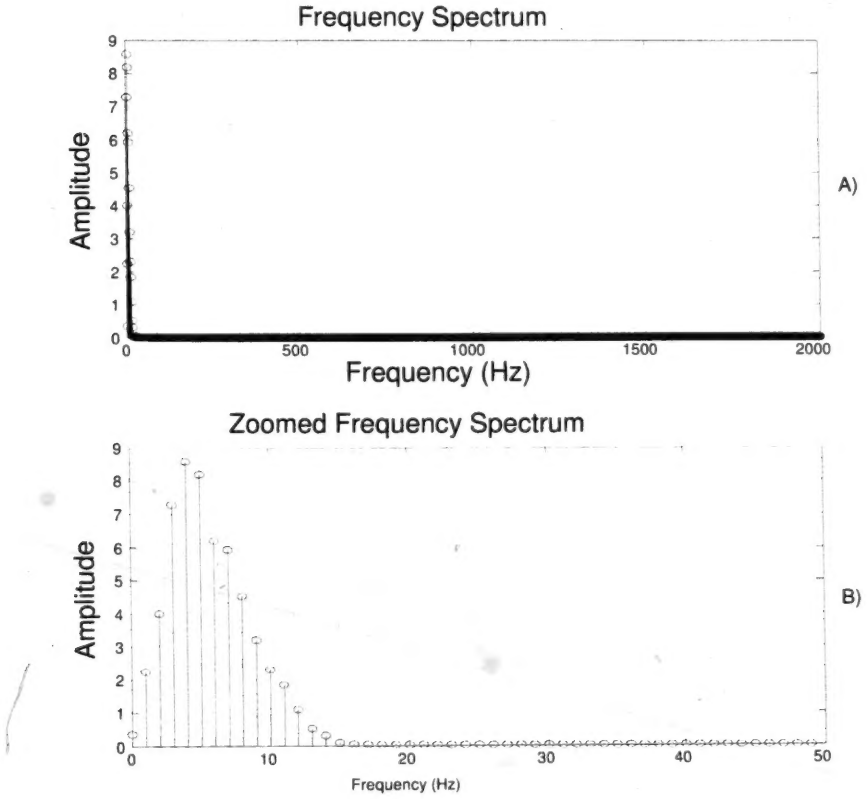

Figure 6.5: Frequency components of the head's angular acceleration

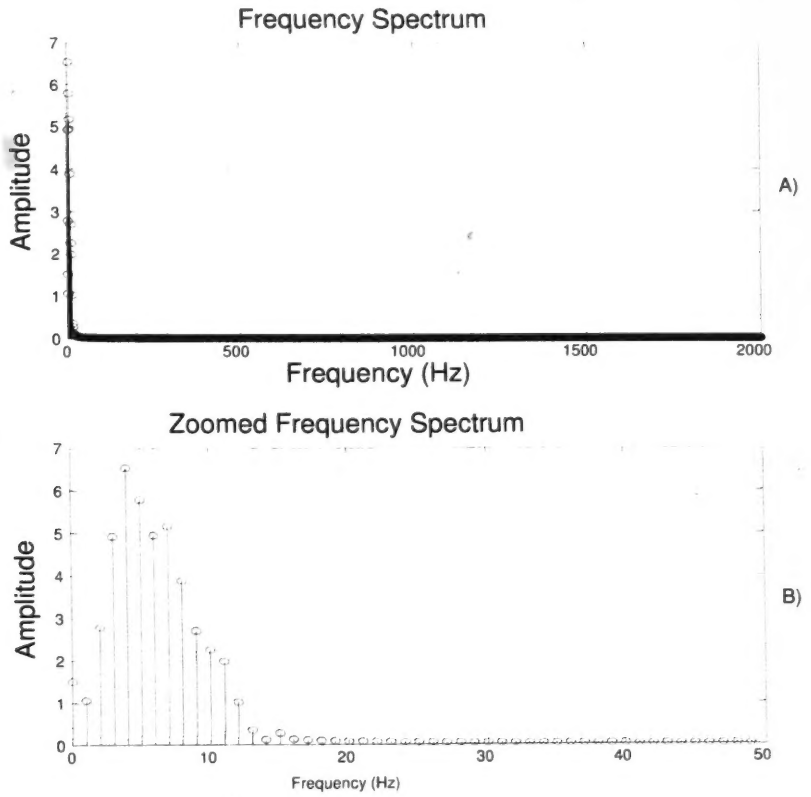

Figure 6.6: Frequency components of the jaw's angular acceleration

A comparison between the angular variables obtained during a velocity change due to rear-impact of 3 $\frac{km}{hr}$, where the subject was not aware of the impending impact, from the two systems will now be presented. Figures 6.7 and 6.8 compare the angular acceleration, velocity and displacement for the subject's head and jaw. The results shown do not appear as good visually as what was obtained in the double and translating pendulum experiments. This is not surprising since there are additional sources of uncertainty that were not present in the previous experiments. In the pendulum experiments, the motion was repetitive and confined to two dimensions resulting in strong frequency components, while impact leads to a broader input frequency range. In this study it was assumed that the majority of motion would occur in two-dimensions, however, since no constraints were placed on the subject some motion out of the plane could occur. This was seen by the high speed cameras which recorded marker position in three dimensions. Also, because of the nature of this study, factors existed that were not present in the pendulum experiments which re-

duced the accuracy of camera measurements. These factors will be discussed next. In the pendulum experiments, the cameras line of sight was never obstructed, while in this study the subject passes through the camera view. As a result, some of the cameras were unable to monitor the markers for the entire experiment and position had to be determined based on measurements from two cameras as opposed to three. Also, there was a reduction in camera resolution since the calibration area had to be made larger to accommodate the subject's movement. Finally, because the markers were placed on soft tissue, some marker movement relative to the head or jaw could occur.

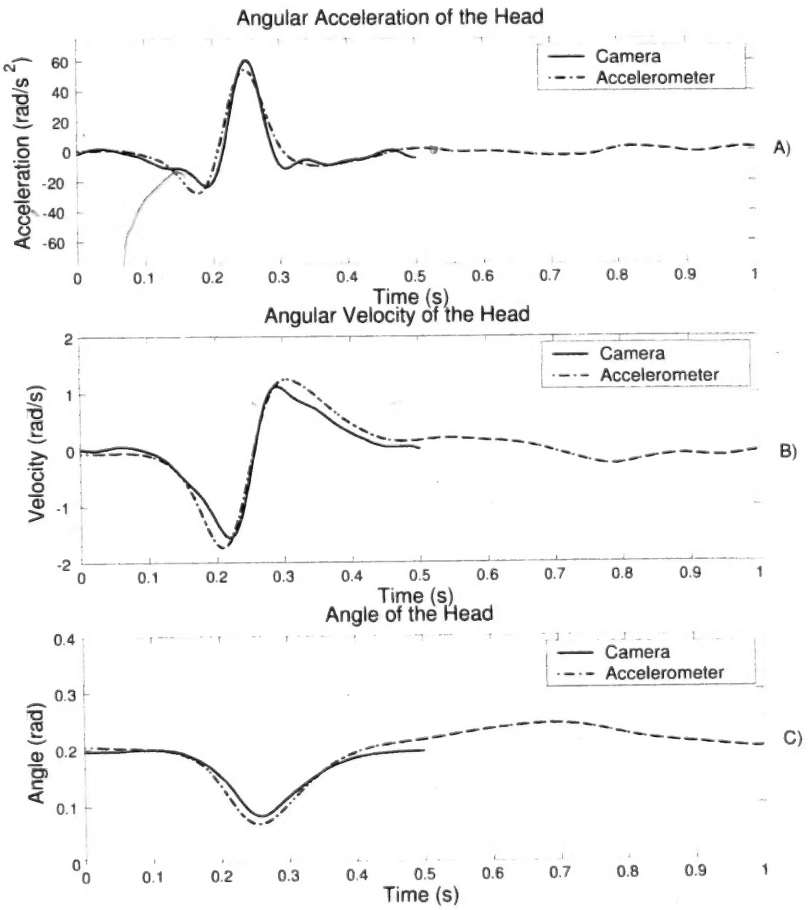

Figure 6.7: Angular kinematics of the subject's head during impact

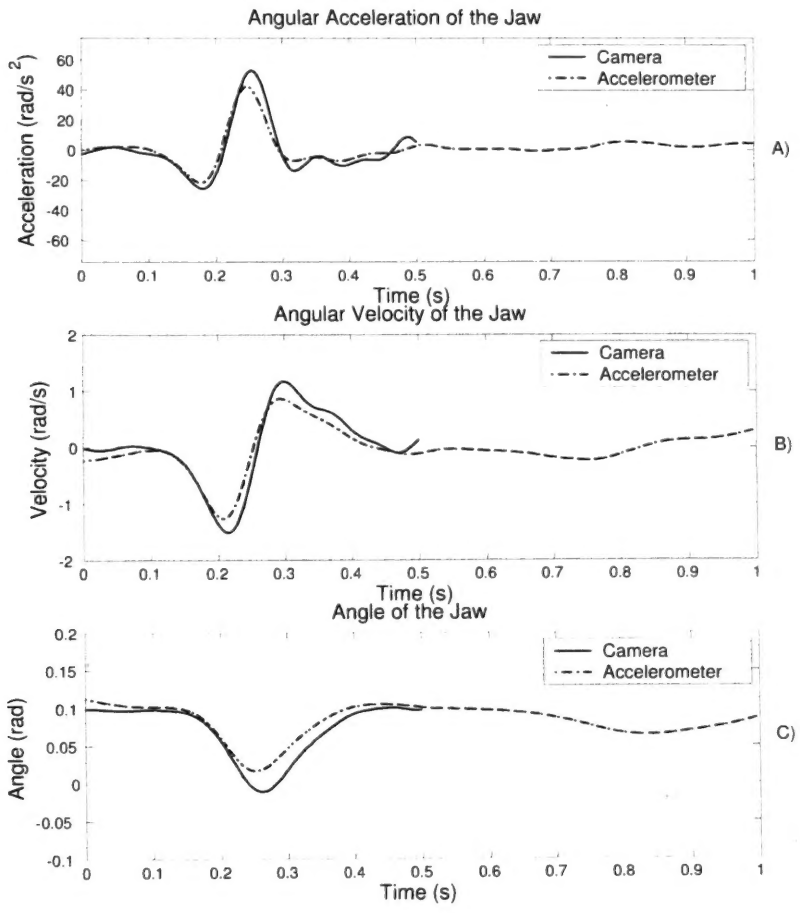

Figure 6.8: Angular kinematics of the subject's jaw during impact

One problem that did not occur, but was expected, was larger effects of filter transients on the integrated data. In the double pendulum experiment, high-pass filter transients corrupted the start of the upper links orientation data set making removal of the angular offset difficult. This was a result of the upper link's large initial movement, which was also expected here since movement was initiated by impact. However, because the impact acted directly on the chair, as opposed to the subject, it was not the case. The initial movement appears to be more gradual similar to what occurred in the translating pendulum experiments. As a result, the filter did not have to be initialized. Even though the results shown above are not as good as what was obtained in earlier experiments, the system error is still less than 10% of full scale. Table 6.1 contains the R's and RMSE's for comparison of the devices for the first 0.5 s.

Table 6.1: R and RMSE angular coefficients for head and jaw

Accel vs. Cam (Head)	**angular acceleration**	**angular velocity**	**angle**
R	0.9454	0.9787	0.9844
RMSE	5.9921 $\frac{rad}{s^2}$	0.1872 $\frac{rad}{s}$	0.0121 rad
Accel vs. Cam (Jaw)	**angular acceleration**	**angular velocity**	**angle**
R	0.9530	0.9677	0.9790
RMSE	5.9637 $\frac{rad}{s^2}$	0.2014 $\frac{rad}{s}$	0.0144 rad

Based on the results shown in the table above, the 10 g accelerometer system agrees well with the high speed camera system for angular measurements. The average error (RMSE) for the variables shown above is within 10% of the full range for each parameter, which is what we were aiming for.

6.2.2 Head and Jaw Translational Kinematics

Determination of 2-D translational kinematics for the head and jaw involved the same procedure that was employed for the double and translating pendulum experiments. Translational acceleration was determined from Equation 2.2

$$\vec{a}_{unknown/N} = \vec{a}_{known/N} + \vec{\alpha}_N \times \vec{r}_N + \vec{\omega}_N \times (\vec{\omega}_N \times \vec{r}_N),$$

where $\vec{a}_{unknown/N}$ refers to the acceleration vector at the temple for head kinematics, or the point on the chin for jaw kinematics (shown in Figure 6.4) in a fixed body frame. Also, $\vec{a}_{known/N}$ is two dimensional vector output of an accelerometer attached to either body, while $\vec{\alpha}_N$ and $\vec{\omega}_N$ are the angular acceleration and velocity vectors for the head and jaw and $\vec{r}$ is the vector from known to unknown acceleration (accelerometer to temple or chin), which was derived from high speed camera output. Translational velocities and displacements were determined through single and double integration of the acceleration vectors. Since the subject started from rest, and we were interested in movement relative to the bodies start position, the start values for velocity and displacement are both zero. The rotation matrix, which was derived in Chapter 2, was used to convert body fixed kinematics to the global reference frame. Output from accelerometers 1 was used as the point of known acceleration for the head, while accelerometer 3 was used as the point of known acceleration for the jaw.

Figures 6.9 and 6.10 overlay plots of X and Y accelerations for the head and jaw. The agreement between the devices is not as good as what was seen in the pendulum experiments, when overlaying acceleration signals, but the same general trends can be

seen in both data sets. Also, the difference between the signals, as a percentage of full range, is within the accepted value of 10% for both X and Y data sets. A statistical comparison between the devices will be presented later in this section.

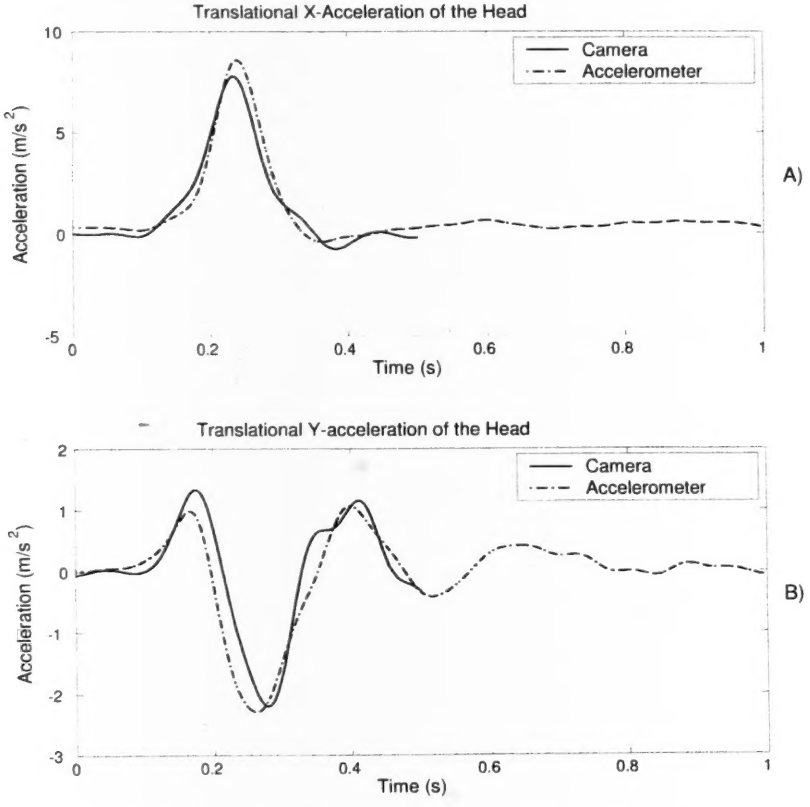

Figure 6.9: Translational X and Y accelerations for the subject's head

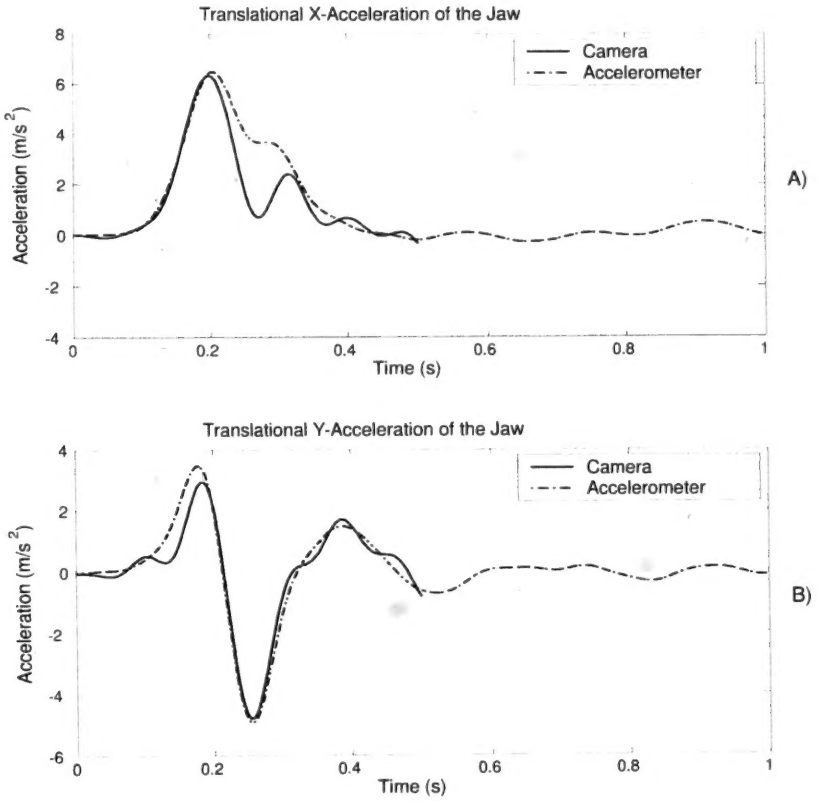

Figure 6.10: Translational X and Y accelerations of the subject's jaw

Figures 6.11 and 6.12 compare head and jaw velocities obtained from the accelerometer and camera systems. The X-velocities, which were obtained from accelerometer output, for the head and jaw appear to underestimate the camera output while no consistent pattern can be seen in the Y-velocities.

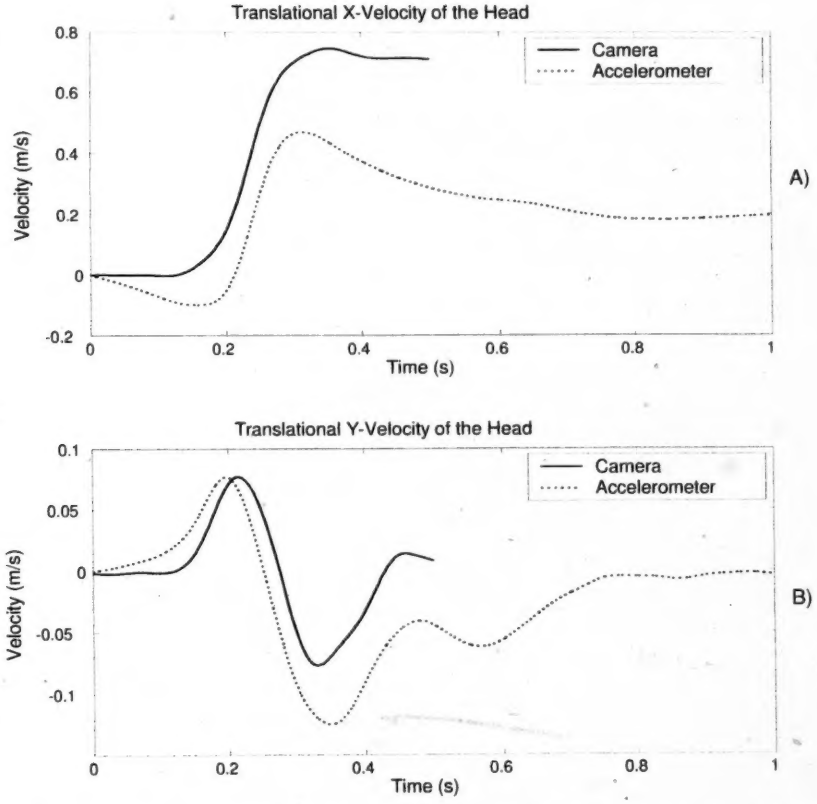

Figure 6.11: Translational X and Y velocities of the subject's head (high-pass Butterworth filter with 0.5Hz cut-off)

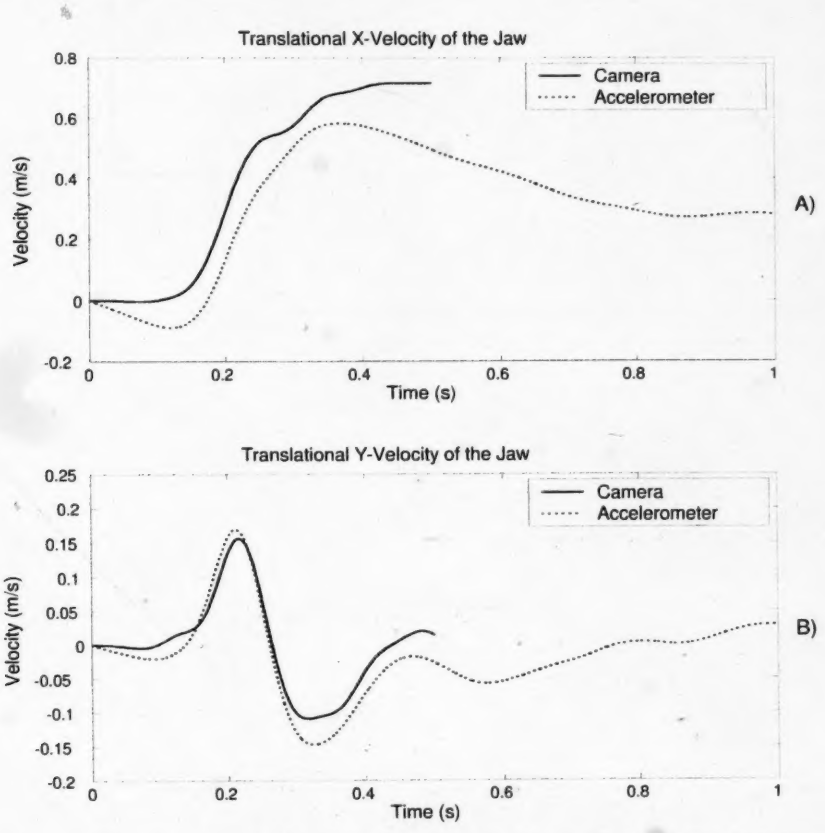

Figure 6.12: Translational X and Y velocities of the subject's jaw (high-pass Butterworth filter with a 0.5 Hz cut-off)

The data shown in Figures 6.11 and 6.12 are the results of passing the integrated acceleration vector through a 4^{th} order high-pass Butterworth filter with a 0.5 Hz cut-off. Although this filter was used in the translating and double pendulum experiments and system agreement was acceptable, the results obtained here are not adequate for our application; therefore, a different approach must be taken. The shape of the X-velocity data in the crash testing experiment was expected to be different than what was seen in the previous chapters. Because pendulum motion is repetitive, the velocity is constantly changing as the pendulum swings. However, in this study, since the velocities were measured in the global reference frame, and chair velocity could not be subtracted since it was not measured, the X-velocity appears to increase and holds until it leaves the view of the cameras. This is a low frequency movement. Since design of a stable filter with a lower cut-off than 0.5 Hz is difficult, a Fast Fourier Transform approach, which can eliminate specific frequencies from a data set, was

applied. Figures 6.13 and 6.14 show the results.

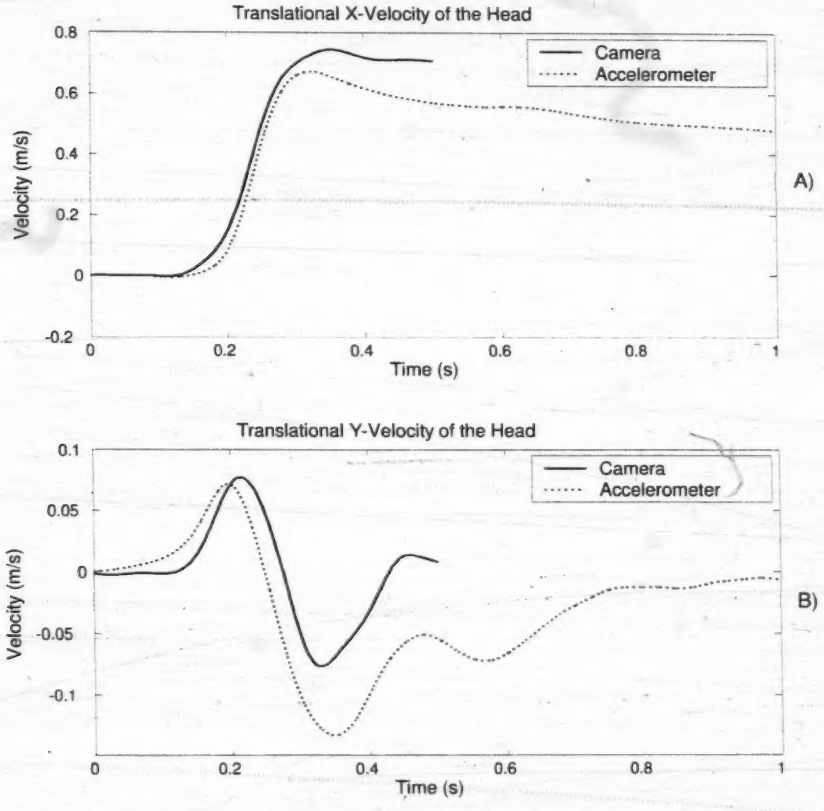

Figure 6.13: Translational X and Y velocities of the subject's head (Fast Fourier Transform filter)

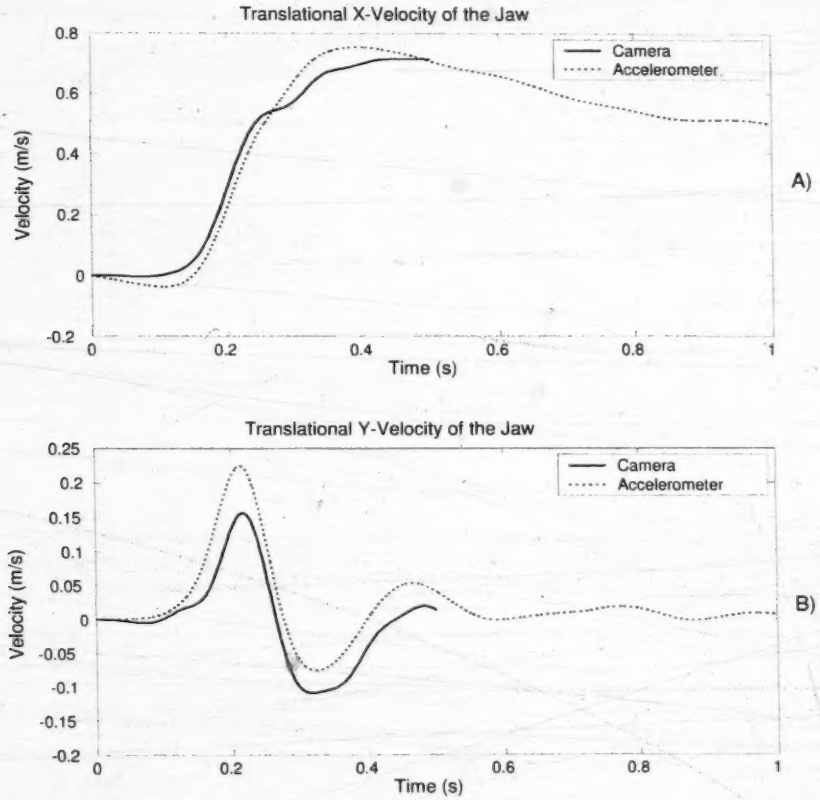

Figure 6.14: Translational X and Y velocities of the subject's jaw (Fast Fourier Transform filter)

In the X-velocity signal, the frequency components from 0-0.3 Hz were removed. Although this is close to the Butterworth cut-off, the roll-off of that filter could be seen up to 1.5 Hz. Based on the range of velocities in the X and Y directions, the difference between the systems is not substantial. The uncertainties in translational velocity, based on static measurement, from Chapter 3 were 0.132 $\frac{m}{s}$ in the X-direction and 0.090$\frac{m}{s}$ in the Y-direction. Although the results in the figure above are based on dynamic measure, where higher uncertainty is expected, the difference between the systems is close to the static uncertainty.

Figures 6.15 and 6.16 compare the X and Y displacements, which were obtained from accelerometers and cameras, for the head and jaw. Figure 6.15, which compares head displacements, shows poor agreement between the devices. Because the change in X-displacement for the head and jaw is essentially drifting, application of

a high-pass filter would not have improved the results. The integration process has magnified the low frequency components, which need to be reduced in order to accurately reproduce the motion, however, a filter would remove them entirely which would not be an improvement. The maximum value for X-displacement in Figure 6.16A was less than 0.2 m, and the error in accelerometer measurements exceeds the expected range of 0.002 m to 0.019 m. However, since we were unable to apply any high-pass filtering, for the reasons stated earlier, no drift could be removed causing an increase in uncertainty with time. In the Y-direction, the maximum displacement measured by the cameras was 5 mm. However, it was shown in Chapter 3 that the uncertainty associated with accelerometer derived displacements was expected to be between 7 mm and 2.3 cm, which is much larger than the actual motion seen here. Therefore, the movements experienced here were too fine for the system to accurately measure. The results from the jaw were better. A comparison of X-displacements showed good agreement, and the Y-displacements only begin to deviate after 0.3 s, which is after the majority of movement. Tables 6.2 and 6.3 show the R's and RMSE's for comparison of translational kinematic variables obtained from the accelerometers and cameras.

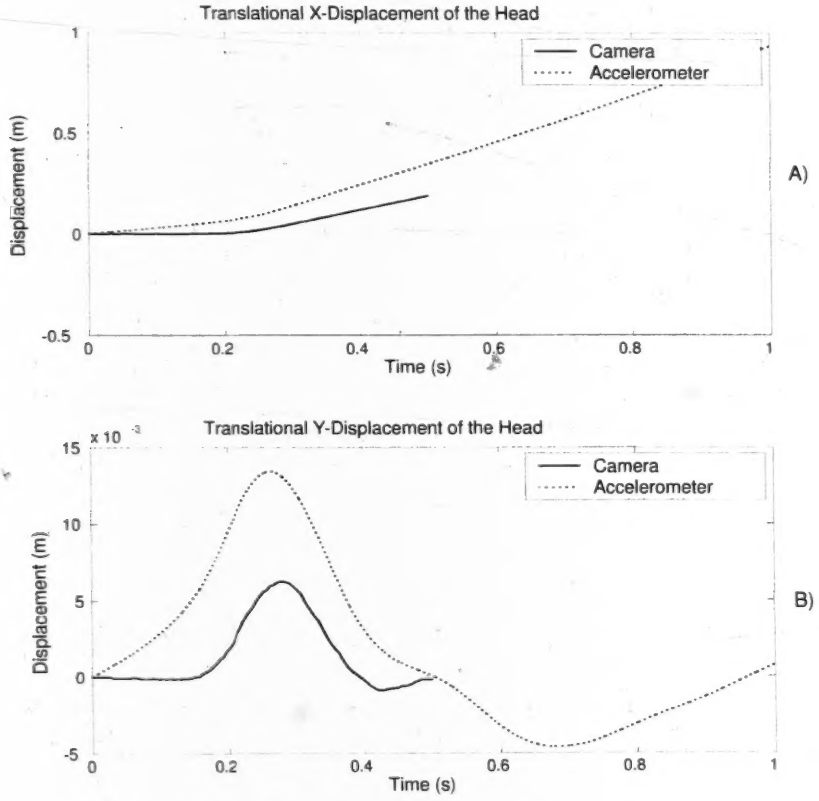

Figure 6.15: Translational X and Y displacements of the subject's head

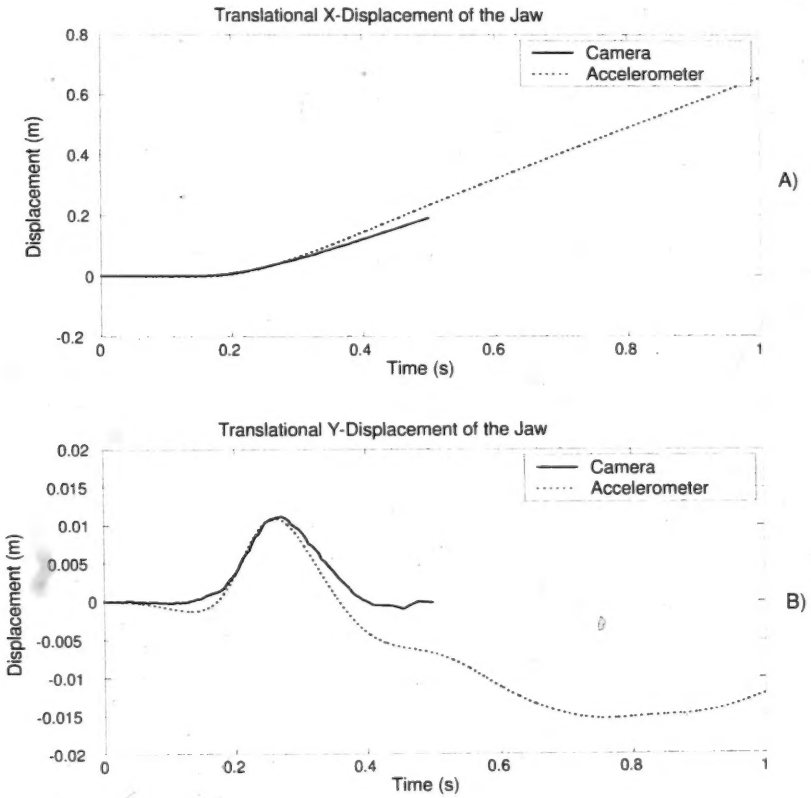

Figure 6.16: Translational X and Y displacements of the subject's jaw

Table 6.2: R and RMSE translational coefficients for the head

X-Direction (Head)	**acceleration**	**velocity**	**displacement**
R	0.9866	0.9963	0.9870
RMSE	0.4690	0.0702	0.0897
Y-Direction (Head)	**acceleration**	**velocity**	**displacement**
R	0.9045	0.8451	0.9060
RMSE	0.4460	0.0468	0.0047

With the exception of Y-displacement of the head, the relationship between all parameters is good based on the R values. The RMSE values for Y-displacements of the head and jaw are nearly the same, however, visually the jaw data appears better. The maximum Y-displacement of the head was approximately 5 mm, while the maximum Y-displacement for the jaw was approximately 12 mm. Based on the uncertainty analysis in Chapter 3, the uncertainty in displacement measurements

Table 6.3: R and RMSE Translational coefficients for the jaw

X-Direction (Jaw)	**acceleration**	**velocity**	**displacement**
R	0.9234	0.9957	0.9996
RMSE	0.8842 $\frac{m}{s^2}$	0.0439 $\frac{m}{s}$	0.0161 m
Y-Direction (Jaw)	**acceleration**	**velocity**	**displacement**
R	0.9715	0.9644	0.7660
RMSE	0.5796 $\frac{m}{s^2}$	0.0414 $\frac{m}{s}$	0.0049 m

with the 10 g system is 3 mm, which is too high to distinguish the movement here. Although the magnitude information was shown to be inaccurate, the peaks of head Y-displacement signals line up well. This could be useful to researchers who are more interested in when peak movement occurs as opposed to the magnitude of motion.

6.3 Conclusions

Based on the results obtained during this experiment, the 10 g system could be used to study head and jaw movements during low speed rear-impact. The agreement between accelerometer and camera derived angular accelerations, velocities and displacements for the head and jaw was very good, which was evidenced by high correlation coefficients and low root mean square errors. The difference between the systems was within 10% of the full range for angular variables. This was expected since the accelerometers performed well in this area during the pendulum experiments, however, accurate determination of translational parameters was more difficult. Since the motion associated with crash testing involved a less defined and wider spread frequency spectrum than what was seen in the pendulum experiments, a different filtering procedure was required for translational X-velocity and displacement. The 4^{th} order high-pass Butterworth filter, applied to X-velocities, was replaced by a Fast Fourier Transform that removed the frequency components from 0-0.3 Hz. For X-displacement, no filtering was applied since it would not have improved the results.

The agreement between accelerometers and cameras for some kinematic variables was better for the jaw than it was for the head. This was shown to be caused by lack of system resolution and the increased range of the jaw, based on uncertainties determined in Chapter 3. Although magnitude information was unreliable for Y-displacement, there was good agreement between peaks, thus, peak timing could still be achieved. This is important to researchers interested in correlating actions, such as when maximum jaw deflection occurs etc. Overall, the results of these tests were promising. The system could definitely be used to determine angular kinematics and,

provided the motion is large enough, also to determine translational kinematics. Since the accelerations measured were much lower than expected, 2 g accelerometers could have been used, and had more time been available they would have been tested.

Chapter 7

Conclusions and Recommendations

7.1 Summary

In this thesis, a sensor based system for measurement of head and jaw movement during low-speed rear impact was developed and tested. The system was capable of measuring two-dimensional kinematics through the use of low-cost accelerometers and MATLAB based data acquisition and analysis software. Prior to impact testing, the system was tested by monitoring double and translating pendulum motion.

In the double pendulum experiment, both 2 g and 10 g accelerometer systems successfully measured the kinematics of a rigid body in pure rotation. For the most part, accelerometer derived angular and translational kinematic parameters agreed very well with the verification devices. Because the first movement when the pendulum was released was large, initialization of the high-pass filter was required when determining angular and translational displacements of the upper-link. Without initialization the start of the data sets were distorted which made removing offsets impossible based on start values alone. The 2 g accelerometers did produce better translational displacements than the 10 g accelerometers, but for all other parameters the systems were considered interchangeable.

Translating pendulum tests were used as verification of the 2 g and 10 g systems ability to measure the kinematics of a rigid body that was translating while rotating, and the accelerometers performed very well. As was the case in the double pendulum experiment, good agreement was achieved between the devices for angular and translational parameters. Although no initialization of the high-pass filter was required, since the motion of the pendulum started more gradually, some effects could

still be seen. Underestimation, which occurred in the final second of the data set, was attributed to high pass filtering. This was solved by ensuring that the duration of sampling exceeded the time period of interest. No statistically significant difference existed between the results obtained with the 2 g and 10 g systems.

A 10 g accelerometer system was used to measure head and jaw movements during low speed rear-impact. Accelerometer derived angular accelerations, velocities and displacements, for both head and jaw, agreed well with the high speed cameras, however, accurate determination of translational parameters, using the accelerometer based system, was more difficult. Because the motion associated with crash testing had some characteristics which were not present during pendulum motion, some of the filters omitted important components of the signal. By applying more appropriate filtering, substantial improvement in the agreement between systems was achieved. Some translational kinematic parameters derived for the jaw showed noticeably better agreement than those obtained for the head. This was deemed to be a result of the uncertainty being larger than the parameter that was being measured. Only 10 g accelerometers were tested since the accelerations were expected to exceed 2 g's and the time we were allotted to use the test apparatus was limited.

7.2 Conclusions and Contributions

The goal of this thesis was to design a sensor based system that could be used to measure head and jaw kinematics during low-speed rear-impact. Although extensive research has been done with motion analysis systems for measuring head and torso movement during rear-impact, no studies were found where head and jaw movements were monitored. Also, the systems employed in these studies typically measured in three-dimensions which involves more computation, higher cost and, for optic systems, unrestricted view of the subject. In this thesis, the two-dimensional accelerometer based system was shown to adequately measure the majority of head and jaw kinematic parameters during low velocity rear-impact. The use of low cost accelerometers reduced the expense of the system, and because it is sensor based, it does not require an unrestricted view. Taking a two-dimensional approach reduced computation without significantly affecting the kinematic parameters of interest. Some ideas for improved performance will be discussed next.

7.3 Improved Performance/Future Work

A system based on four biaxial accelerometers was proposed and shown to work relatively well when compared to more sophisticated motion analysis techniques. However, there is still a lot of room for improvement.

1. One major problem encountered during this thesis was filter transients. Although the high-pass filters applied did remove drift from velocity and displacement data sets, in some cases the transients that resulted caused distortion of the signal. This distortion was much more significant for displacement than it was for velocity. One possible solution to this problem would be to incorporate a gyroscope into the design. This was not done because the angular velocities due to impact were expected to exceed the range of a typical gyro, but this was not the case. Also, since a gyroscope could be used to determine angular acceleration by differentiating its output, the number of biaxial accelerometers required by the system could be reduced from 2 to 1. Determination of angular displacement would still require integration, but since it will only be single integration, significant filtering problems are not anticipated.

2. Initial angular offsets were obtained from verification devices, since large bias errors present in 10 g accelerometer data prevented determination of the angle from static measurements. Since this system is meant to be employed independently, it must be capable of determining initial angular offsets on its own. The addition of a tilt sensor to the system would make this possible. These devices are inexpensive and offer good reliability and repeatability. A more expensive alternative would be to use a higher resolution data acquisition system.

3. The tooth trays that were used during the impact tests interfered with proper jaw movement, and prevented the subject from fully closing their mouth. These trays were necessary to attach the circuit boards, which contained the accelerometers, to either the head or jaw. An alternative approach would be to cement a bracketing system to the teeth (similar to the approach taken by Flavel [48]). This requires redesign of the circuit boards to reduce their size, but would eliminate the bulk of the tray and allow proper movement of the jaw. Because the circuit boards used in this experiment were not designed specifically for this application, they contained extra sensors that were not required. Therefore, reducing their size should not be difficult.

4. The head and jaw kinematics reported during the impact tests were measured relative to the ground. A better representation of the subjects movement would have been to take measurements relative to the chair, since this would better represent the motion of the head inside a vehicle. By adding an additional channel to measure chair

acceleration and placing a reflective marker on the chair, the head and jaw kinematics could be measured, and verified, relative to the chair.

5. Translational jaw data showed noticeably better agreement than translational head data for some variables. This was a result of inadequate accelerometer sensitivity and system resolution. Use of more sensitive accelerometers, such as the 2 g versions, and a higher resolution data acquisition system would reduce uncertainty in these measurements.

Appendix A

Additional Equipment Theory

A.1 Accelerometer Theory

An accelerometer is a device which converts the effects of mechanical motion into an electrical signal that is proportional to its acceleration. This can be achieved in a few different ways, but only those accelerometers based on spring mass systems will be discussed. The theoretical basis for this design comes from Hooke's law which states that a spring will exhibit a restoring force proportional to the amount it has been stretched or compressed ($F = kx$), and Newton's second law of motion which states that a force operating on a mass that is accelerated will exhibit a force with a magnitude $F = ma$. Figure A.1 shows graphic representation of accelerometer theory.

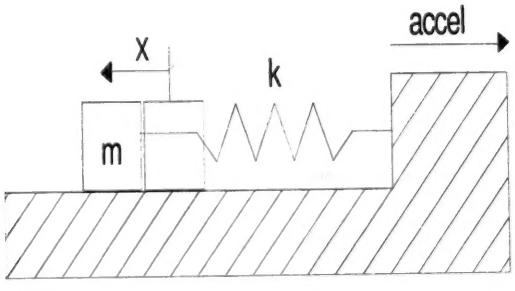

Figure A.1: Simplified accelerometer model

When this system experiences acceleration a resultant force equal to ma will cause either compression or expansion of the spring under the constraint $F = ma = kx$. Therefore, the acceleration can be determined from $a = \frac{kx}{m}$ provided the displacement is known. This changes the focus of the problem from determining acceleration to determining displacement of the mass.

The ADXL 202/210 accelerometers used in this study work in a similar way. The mass, which is a micromachined polysilicon structure, is suspended above a silicon wafer by polysilicon springs, which provide resistance to acceleration forces. Measurement of mass displacement is accomplished with a differential capacitor. A capacitor, which is composed of two parallel plates, is an electrical component that stores charge. The capacitance of these devices is governed by $C = \frac{k}{x_0}$, where k is a property of the material between the plates, and x_0 is the distance between them. Therefore, through knowledge of capacitance and k the distance between the plates can be determined. The differential capacitor used by the ADXL accelerometers combines two simple capacitors as shown in Figure A.2.

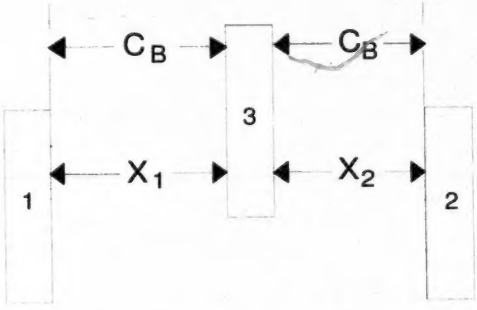

Figure A.2: Differential capacitor

Plates 1 and 2 are fixed while plate 3, which is attached to the mass, is free to move. When the device is at rest both x_1 and x_2 are equal to x_0 and each capacitor displays a capacitance of $C = \frac{k}{x_0}$. When the sensor experiences motion, plate 3 moves and the differential capacitance, which is defined as the difference between the output from the two capacitors, changes proportionally to the acceleration. Application of closed-loop feedback, which involves applying voltage across the capacitor to hold the mass in place, improves linearity by using the electrostatic forces to keep the mass in place. In closed-loop feedback the applied voltage is used to determine acceleration.

A.2 Camera Theory

ProReflex MCU 240 cameras will be used with Qualisys' PC Reflex software for verification of accelerometer derived kinematics. The cameras, which were also developed by Qualisys, are capable of monitoring high speed motion and delivering high precision measurements. The theory behind their operation involves a group of infrared light emitting diodes, which are mounted around the lens, flashing at an integer fre-

quency that is set between 1 and the maximum capable frequency of the camera (for the MCU 240 the maximum is 240 Hz). The infrared light hits reflective markers which return the energy to the lens, in the form of reflected light, and the 2-D image of the marker, which has been reflected onto the CCD (charged couple device) of the camera, is digitized and processed in real-time by the capture device. Marker size and centroid are determined through a sub-pixel interpolation algorithm. Although the actual resolution of the camera is 658 (horizontal) × 496 (vertical) pixels, Qualisys sub-pixeling technology claims to increases these numbers to 60000 (horizontal) × 45000 (vertical) sub-pixels, which allows tracking of much smaller movements. Based on this resolution the cameras are capable of detecting movements as small as 0.03mm in a 2 m×2 m×2 m measurement volume. Once the 2-dimensional coordinates of each marker are calculated they are output in real-time to a host computer through a serial port. Multiple cameras, which are linked together, can sample simultaneously and their combined output can be used to determine the 3-D position of each marker in view. Tables 1 and 2 show examples of the accuracy that can be obtained with different marker sizes at two different measuring distances.

Table A.1: Camera accuracy from a distance of 1m

Marker Diameter (mm)	**240 Hz**
4	0.03 mm
7	0.02 mm
12	0.02 mm
19	-

Table A.2: Camera accuracy from a distance of 5m

Marker Diameter (mm)	**240 Hz**
4	0.33 mm
12	0.20 mm
19	0.22 mm
30	0.14 mm

These values have been taken from Qualisys' ProReflex MCU brochure. In this study 7 mm diameter markers will be used and the measurement distance will not exceed 2 m. One thing to note is that in our testing we were only able to obtain a maximum resolution of approximately 0.5 mm for a 7 mm marker. Resolution was based on the standard deviation obtained from the calibration procedure.

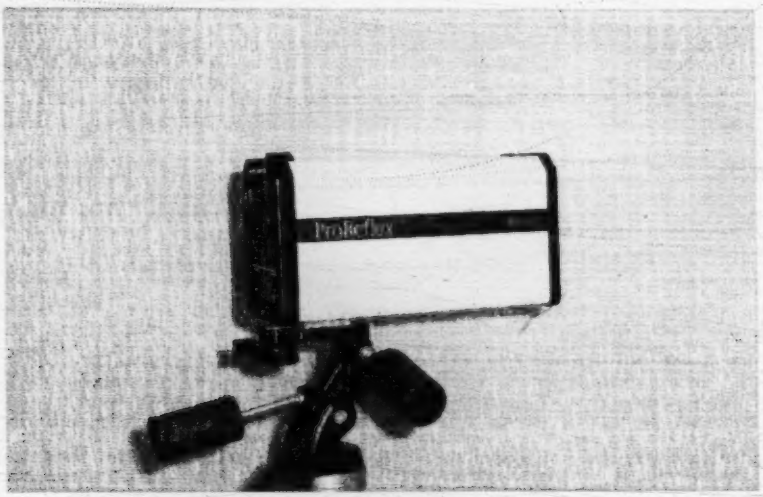

Figure A.3: ProReflex MCU 240 high speed camera

A.2.1 Camera System Set-Up

In this study 3 ProReflex MCU 240 cameras will be used to determine 3-D marker positions. Although only two dimensional measure is required, since the accelerometers only measure planar movement, previous experience showed that the camera system was more stable when three cameras were employed and 3-dimensional measurements were taken. The main motion capture device will be directly connected to the data acquisition unit while subsequent cameras are linked together with rj-45 connectors. This set-up can be seen in Figure A.4. Accurate measurement requires the cameras be placed on non-moving objects, such as tripods, and that they be positioned so that all reflective references are in view of at least two of the cameras during calibration and that the volume where motion will be occurring is in view of all cameras. External triggering can be achieved by inputting a 5 V signal to the cameras through a serial port, or activation of the camera can be used to trigger a separate data acquisition system by running a line out from the camera which produces a 5 V signal coinciding with each exposure initialization.

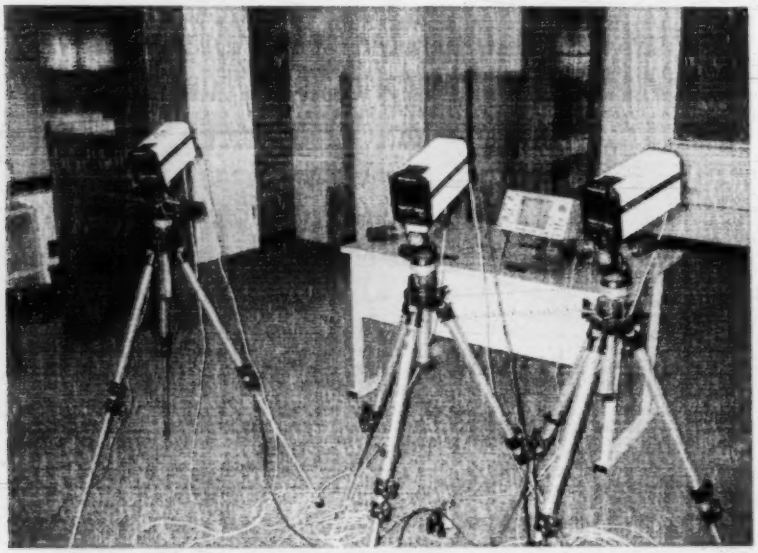

Figure A.4: High speed camera set-up

Software

Before any measurements are taken the correct camera linearization files must be loaded. This is important since location of the reflective markers on the CCD is affected by camera lens type, focus setting, lens mounting alignment over the CCD and lens distortion, which the linearization process corrects. Also, the correct COM port, which tells the computer where the data is coming from, and the correct baudrate, which is the speed that data is collected from the cameras, must be input. PC Reflex software is used to record and interpret data collected by the high speed cameras. Some features within the program include adjustment of the number of markers tracked, time period of the recording, frequency of data collection and external trigger activation. Also, there is a buffering mode which allows measurement data to be stored in each camera's buffer which will not be requested by PC Reflex until the entire measurement is finished. This prevents data loss by giving the cameras more time to perform calculations as opposed to sending the data directly to PC Reflex during measurement itself, which occurs if this option is not used.

Calibration

Prior to calibration all reflective surfaces in the test area should be removed or covered since they will interfere with the process. Calibration begins by placing the L-shaped frame, which can be seen in Figure A.5, so that the reference structure appears in the middle of all the camera's fields of view. Although calibration can be performed with the reference in the view of only two camera, placing it where all cameras can see it increases accuracy. In the calibration program the X-axis should be defined as the direction of horizontal movement, the Y-axis should be defined as vertical movement and the Z-axis should be defined in the direction out of the plane. During calibration the wand, which can be seen in Figure A.6, should be moved in all three directions. A suitable duration to ensure good calibration for all cameras should be 20-30 s long. During this time period the wand should be moved through the entire measurement volume in the X,Y and Z directions focussing on the area where most motion is expected to occur. Calibration should occur at the same sampling rate that will be used during testing.

Figure A.5: Calibration frame

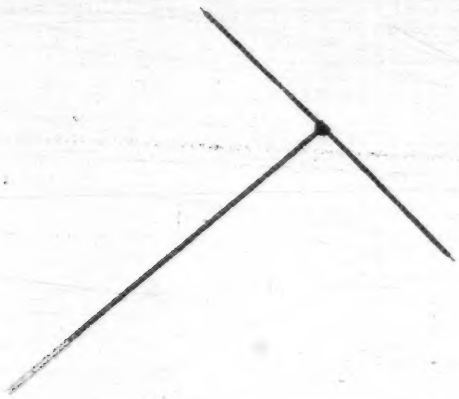

Figure A.6: Calibration wand

A.3 Potentiometer Theory

A variable resistor is a device used to alter the current that flows through a circuit. This is done by passing a voltage through a resistive element and a movable wiper blade. Depending on the position of the wiper blade along the element, a different resistance will be present in the circuit, thus, the current can be altered. Potentiometers are based on the same idea, but they incorporate an additional terminal so varying the wiper position causes changes in voltage as opposed to current. Figure A.7 shows a simplistic model of potentiometer operation.

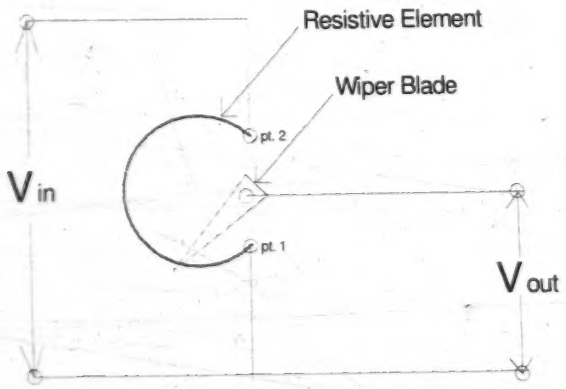

Figure A.7: Potentiometer diagram

In a potentiometer a constant voltage is applied across a resistive element. Since the resistance of the circuit increases from pt.1 to pt. 2, measurement of the voltage through the circuit formed by the wiper blade will vary. This changing voltage can be used to determine at what location along the element the wiper blade is positioned. In this thesis a potentiometer will be used to measure the angle of a double link pendulum where the device will be calibrated so that the voltage output corresponds to the angle of the link.

A.4 Encoder Theory

An encoder is a rotary device that outputs digital pulses corresponding to incremental angular motion. This is achieved through the use of a wheel organized in tracks of clear and opaque strips. An infrared beam, which is detected by optical sensors, is interrupted by the opaque strips on the disk as it rotates. These interruptions produce the digital pulses used to determine angular motion. There are two main types of rotary encoders: absolute and incremental. Absolute encoders produce a unique digital word at each position of the shaft, which requires more bits for higher resolution, while incremental encoders use digital pulses obtained during rotation to determine the shafts relative position. In this thesis an incremental encoder will be used for verification of translating pendulum motion.

An incremental encoder is simpler in design than an absolute encoder. The 2-bit system, which consists of two tracks and two sensors, can distinguish as many positions as slots on the track while an absolute encoder, employing the same number of bits, can distinguish only four positions. As the incremental encoder shaft rotates pulses occur on both channels at a frequency proportional to the speed of the shaft, while direction of rotation is determined based on the phase relationship between the signals. Through knowledge of the number of pulses and resolution of the disk, angular motion can be assessed. In some cases a third index channel is used as a reference for the zero position and to keep track of full revolutions. Figure A.8 illustrates the code disk pattern and output signals.

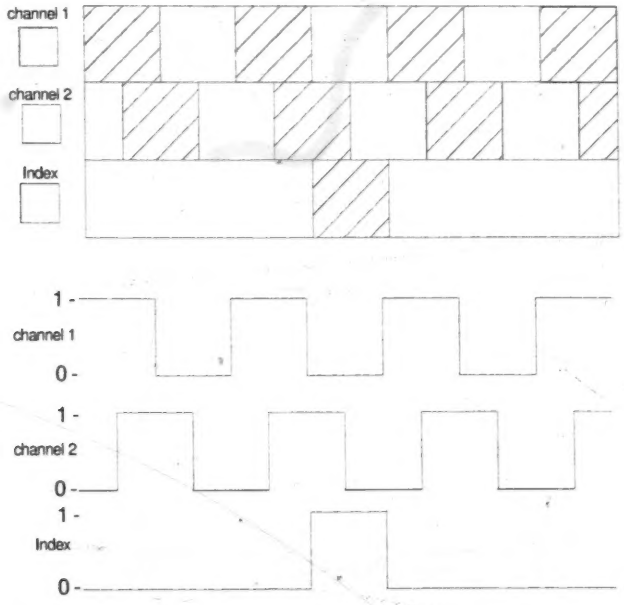

Figure A.8: Encoder code disk pattern and output signals

As shown in the above figure, a value of 1 on channel 2 during a transition from high to low on channel 1 will occur during clockwise rotation, while the opposite will occur during counterclockwise rotation. This phase relationship is used to determine the direction the encoder shaft is rotating.

Appendix B

Filter Cut-off Selection

In this appendix, the frequency spectrum as well as residual analysis plots will be shown for accelerometer and high speed camera data from the double pendulum experiment. The purpose of these plots is to demonstrate how the 15 Hz low-pass filter cut-off was selected.

B.1 Frequency Cut-off Analysis

One way to determine a frequency cut-off is through harmonic analysis. The signal can be viewed in the frequency domain as harmonic components by performing a Fourier transform. This involves resolving a time series into a series of numbers that characterize the relative amplitude and phase components of the signal as a function of frequency. Another technique is determining the residual [57] between a filtered and unfiltered signal over a wide range of cut-off frequencies. Figure B.1 shows the Fourier transform of an accelerometer signal from the double pendulum experiment, while Figure B.2 plots the residual at a number of cut-off frequencies using a 5^{th} order Butterworth filter.

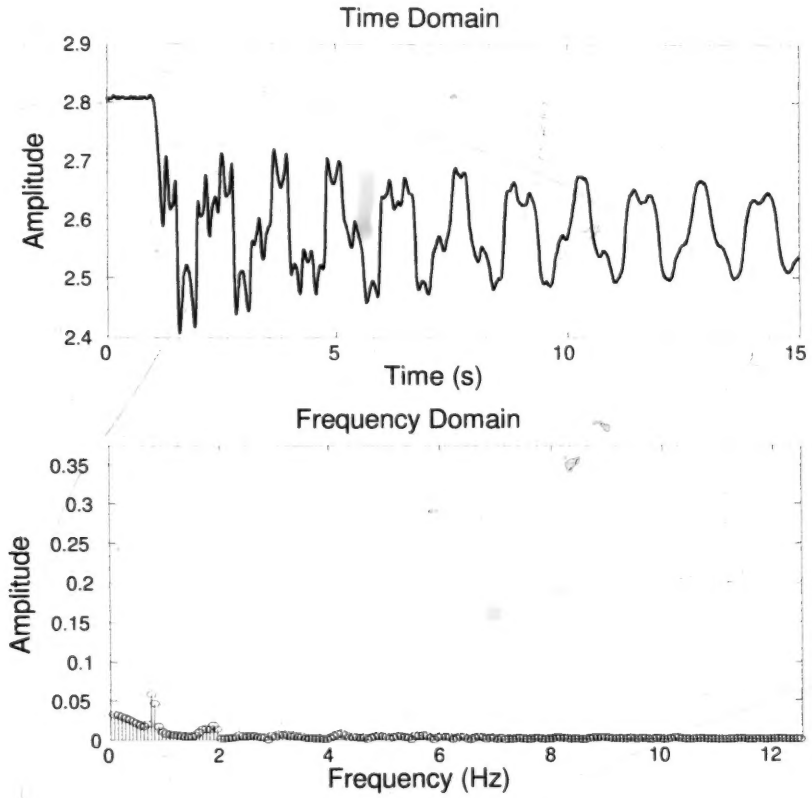

Figure B.1: Frequency spectrum for a raw accelerometer signal. Amplitude is in Volts.

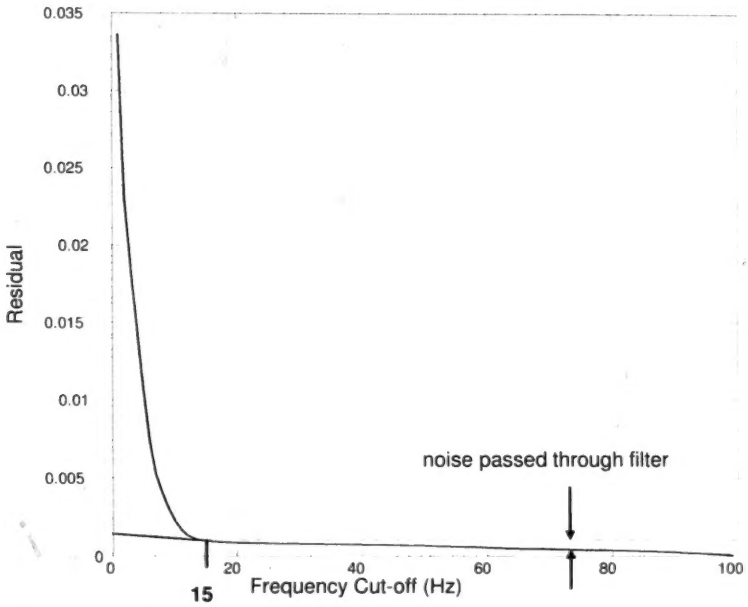

Figure B.2: Residual for an accelerometer signal based on a wide range of cut-off frequencies

The frequency spectrum in Figure B.1 shows no significant components after approximately 2 Hz, however, 15 Hz was used as the cut-off so the system is not limited to applications where only very low frequencies are present. Figure B.2 shows that a 15 Hz cut-off is in the flat region of the residual plot, which means minimal noise will pass through the filter. Figures B.3 and B.4 show the same plots generated from high speed camera data.

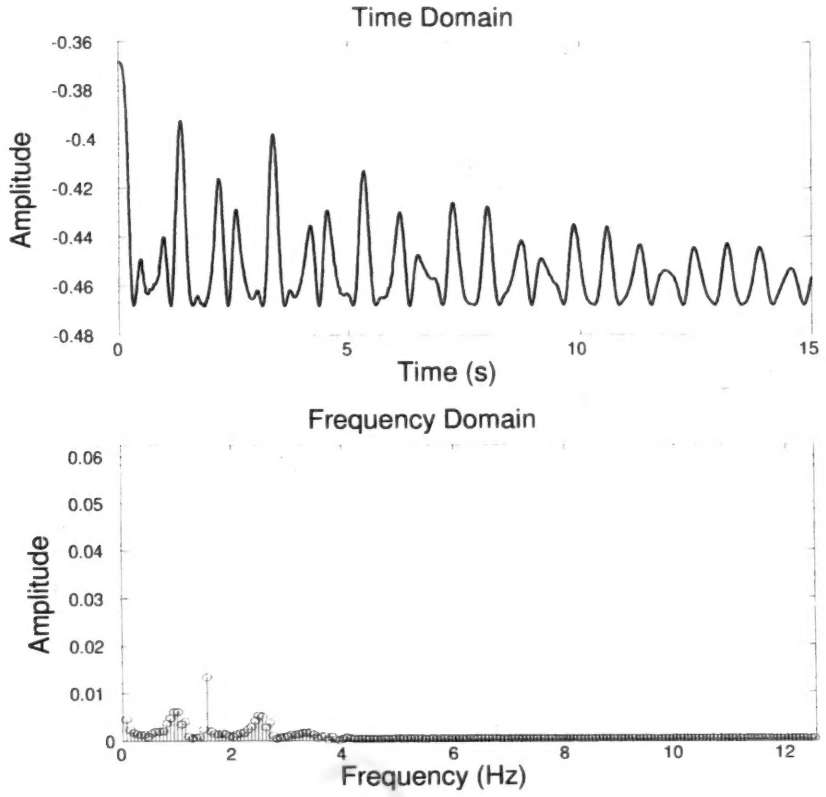

Figure B.3: Frequency spectrum for high speed camera position data

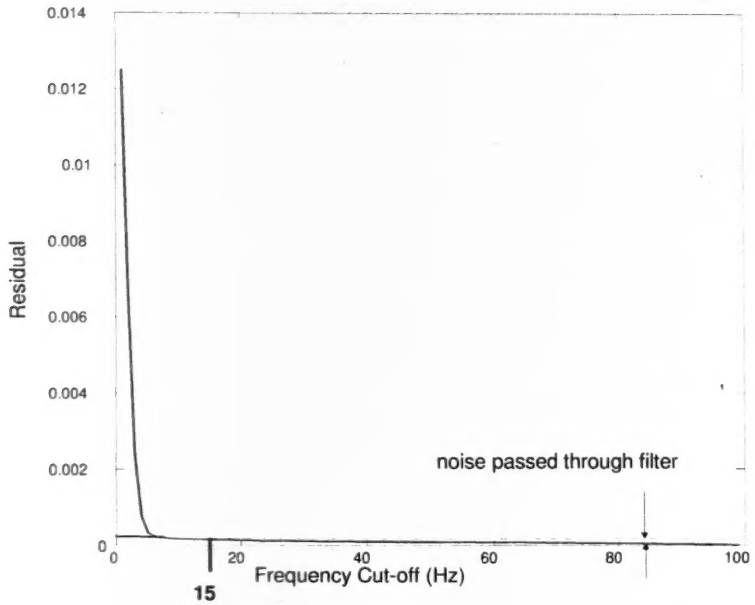

Figure B.4: Residual for high speed camera displacement data based on a wide range of cut-off frequencies

Figure B.3, which plots the amplitude of frequency components present in high speed camera position data, shows no significant frequency components above approximately 3 Hz. Also Figure B.4, which plots the residual, shows very little noise passing through the filter with a 15 Hz cut-off. Based on these results, use of a 15 Hz cut-off should adequately remove noise while not limiting the system to low frequency measurement.

Bibliography

[1] Insurance Bureau of Canada, "*IBC, Memorial University of Newfoundland (MUN) launch course on whiplash and back injury,*" **2002** http://www.insurance-canada.ca, section: professional, sub-section: claims

[2] Lubin,S.,Sehmer,J.,"*Are automobile head restraints used effectively,*" Canadian Family Physician 39,**1993**,pp.1584-1588

[3] Yogandan,N.,Pintar,F.A.,Larson,S.J.,Sances,A Jr (Eds.),"*Frontiers in Head and Neck Trauma: Clinical and Biomechanical,*" IOS Press, Amsterdam, Netherlands. **1998**

[4] Castro, W.H., Schilgen, M., Meyer, S., Weber, M., Peuker, C., Wortler, K., "*Do "whiplash injuries" occur in low-speed rear impacts?,*" European Spine Journal 6, **1997**, pp.366-375

[5] Kasch H, Hjorth T, Svensson P, Nyhuus L, Jensen TS., "*Temporomandibular disorders after whiplash injury: a controlled, prospective study,*" J Orofac Pain **2002**

[6] Garcia R Jr, Arrington JA., "*The relationship between cervical whiplash and temporomandibular joint injuries: an MRI study,*" Cranio **1996**; 14(3):233-9.

[7] Wienburg,S.Lapointe,H.,"*Cervical extension-flexion injury (whiplash) and internal derangement of the temporomandibular joint,*" Journal Oral Maxillofacial Surgery: 45, **1987**, pp.653-656

[8] McKay DC, Christensen LV., "*Whiplash injuries of the temporomandibular joint in motor vehicle accidents: speculations and facts,*" J Oral Rehabil **1998**; 25(10):731-46

[9] Weinburg, S., Lapointe, H., "*Cervical whiplash injuries to the neck,*"JAMA **1953**, pp.152-169

[10] Mertz, H.J.,"*Kinematics and Kinetics of Whiplash,*" Doctoral Dissertation, Wayne State University, Detroit Michigan, **1967**

[11] Veltink,P.H.,Tijsmans,R.,Franken,H.M.,Boom,H.B.K.,"*Identification of Electrically Stimulated Quadriceps - Lower Leg Dynamics - The use of Accelerometers for Estimating Knee Joint Acceleration and Quadriceps Torque.*" IEEE Transaction, **1992**, pp.1339-1340

[12] Nusholtz, G.S., Molinaro,R.,"*Force Deflection Curves For Air Bag Response.*" Experimental Techniques, April/May **1991** pp. 33-35

[13] Morris, J.R.W, "*Accelerometry - A Technique For the Measurement of Human Body Movements.*" J. Biomechanics, **1973**, Vol.6, pp.729-736

[14] Becker, E., Willems, G., "*An Experimentally Validated 3-D Inertial Tracking Package for Application in Biodynamic Research.*", Proceedings 19th Stapp CAr Crash Conf, **1975**

[15] Bridwell, K., "*Anatomical Planes of the Body,*" **2001,** http://www.spineuniverse.com/displayarticle.php/article1023.html

[16] Kane,T.R.,Hayes,W.C., Priest, J.D., "*Experimental Determination of Forces Exerted in Tennis Play,*" Biomechanics IV, University Park Press, Baltimore, MD, 898-904 **1974**

[17] Hayes,W.C., Gran,J.D.,Nagurka,M.L.,Feldman,J.M.,Oatis,C., "*Leg Motion analysis during gait by multiaxial accelerometry,*" J biomech Engg 105, **1983**, pp. 283-289

[18] Padogaonkar, A.J, Krieger, K.W, and King, A., "*Measurement of Angular Acceleration of a Rigid Body Using Linear Accelerometers.*" J. Appl. Mech, **1975**, pp.552-556

[19] Liu, Y.K.,"*Discussion of Angular Acceleration of a Rigid Body Using Linear Accelerometers.*"Journal of Applied Mechanics, Vol. 42, June **1976**, pp.277-278

[20] Mital,N.K.,King,A.I.,"*Computation of Rigid-Body Rotation in Three-Dimensional Space From Body-Fixed Linear Acceleration Measurements.*" Journal of Applied Mechanics, Vol.46, December **1979,** pp.925-930

[21] Chou,C.C.,Sinha,S.C.,"*On the Kinematics of the Head using Linear Acceleration Measurements.*" Journal of Biomechanics, Vol.9, **1979**, pp. 607-613

[22] Cholewicki,J.,Panjabi,M.M.,Nibu,K.,Babat,L.B.,Grauer,J.N.,Dvorak,J.,"*Head Kinematics During In Vitro Whiplash Simulation.*" Accid. Anal. and Prev. Vol. 30, No. 4, **1998**, pp. 469-479

[23] Nusholtz, G.S, "*Geometric Methods in Determining Rigid-body Dynamics.*" Experimental Mechanics, June **1993**, 153-158

[24] Viano,D.C.,Melvin,J.W.,McCleary,J.D.,Madeira,R.G.,Shee,R.T.,Horsch,J.D.,"*Measurement of Head Dynamics and Facial Contact Forces in the Hybrid III Dummy,*" General Motors Research Labs, Biomedical Science Department, Warren MI., **1989**, pp.269-289

[25] Shea, R.T.,Viano,D.C., "*Computing Body Segment Trajectories in the Hybrid III Dummy Using Linear Accelerometer Data.*" Journal of Biomechanical Engineering, Vol. 116, February **1994**, pp.37-43

[26] Smidt,G.L.,Deusinger,R.H.,Arora,J.,Albright,J.P.,"*An Automated Accelerometry System for Gait Analysis.*" Journal of Biomechanics, Vol. 10, **1977**, pp.367-375

[27] LaFortune, M.A.,"*Three Dimensional Acceleration of the Tibia During Walking and Running.*", Journal of Biomechanics, Vol.24, No.10, **1991**, pp.877-886

[28] Kumar,S.,Narayan,Y.,Amell,T.,"*Analysis of low velocity frontal impacts.*" Clinical Biomechanics 18, **2003**, pp.694-703

[29] Angeles,J.,"*Computation of Rigid-Body Angular Acceleration From Point-Acceleration Measurements.*" Transactions of ASME, Vol.109, June**1987**, pp.124-127

[30] Yoganandan,N.,Pintar,F.A.,Cusick,J.T.," *Biomechanical analyses of whiplash injuries using an experimental model.*" Accident Analysis and Prevention 34, **2002**, pp. 663-671

[31] Ladin,Z.,Flowers,W.C.,Messner,W.,"*A Quantitative Comparison of a Position Measurement System and Accelerometry.*" Journal of Biomechanics, Vol. 22, **1989**, pp. 295-308.

[32] Willemson,A.T.,Van Alste,J.A.,Boom,H.B.K.,"*Real-Time Gait Assessment Utilizing a New Way of Accelerometry.*",Journal of Biomchanics, Vol.23, **1990**, pp.859-863

[33] Tong, K.,Granat,M.H.,"*A practical gait analysis system using gyroscopes.*" Medical Engineering and Physics 21, **1999**, pp.87-94

[34] Ladin.Z.,Wu,G.,"*Combining Position and Acceleration Measurements for Joint Estimation.*", Journal of Biomechanics,Vol.24, **1991**, pp. 1173-1187

[35] McConnell, W.E.,Howard,R.P.,Poppel,J.V.,Krause,R.,Guzman,H.M.,Bomar,J.B., Raddin,J.H.,Benedict,J.V.,Smith,H.L.,Hatsell,C.P."*Human Head and Neck Kinematics After Low Velocity Rear-End Impacts - Understanding "Whiplash".*", Society of Automotive Engineers inc., **1995**, pp 215-233

[36] Heyn,A.,Mayagoita,R.E.,Nene,A.V.,Veltink,P.H.,"*The Kinematics of The Swing Phase Obtained From Accelerometer and Gyroscope Measurements.*" 18^{th} Annual Conference of the IEEE Engineering in Medicine and Biology Society Amsterdam,**1996**, pp.463-464

[37] Mayagoita,R.E.,Nene,A.V.,Veltink,P.H.,"*Accelerometer and rate gyroscope measurement of kinematics: an inexpensive alternative to optical motion analysis systems.*" Journal of Biomechanics **2002**, Vol. 35, pp. 537-542

[38] Wu, G.,Ladin,Z.,"*The Study of Kinematic Transients in Locomotion Using the Integrated Kinematic Sensor.*" IEEE trans. rehab. engg, Vol.4, No.2, **1996**, pp.193-200

[39] McConnell, W.E.,Howard,R.P.,Guzman,H.M.,Bomar,J.B.,Raddin,J.H.,Benedict,J.V., Smith,H.L.,Hatsell,C.P.,"*Analysis of Human Test Subject Kinematic Responses to Low Velocity Rear End Impacts.*" Society of Automotive Engineers inc., **1991**, pp 21-30

[40] Siegmund,G.P.,Sanderson,D.J.,"*The Effects of Perturbation Acceleration and Advance Warning on the Neck Postural Responses of Seated Subjects.*" Experimental Brain Research, 144, **2002**, pp.314-321

[41] Siegmund,G.P., Sanderson,D.J.,Myers,B.S.,Inglis,T,"*Rapid neck muscle adaptation alters the head kinematics of aware and unaware subjects undergoing multiple whiplash-like perturbations.*" Journal of Biomechanics 36, **2003**, pp. 473-482

[42] Hannam,A.G.,DeCou,R.E.,Scott,J.D.,Wood,W.W.,"*The Kinesiographic Measurement of Jaw Displacement.*" The Journal of Prosthetic Dentistry, Vol.44, Number 1, July **1980**, pp.88-93

[43] Plesh,O.,Bishop,B.,McCall,W.D.Jr.,"*Kinematics of Jaw Movements During Chewing at Different Frequencies.*" Journal of Biomechanics, Vol. 26, No. 3, **1993**, pp.243-250

[44] Miles,T.S.,Wilkinson,T.M.,"*Limitations of Movement by Antagonist Muscle Stiffness During Unloading of Human Jaw Closing Muscles.*" Expmerimetal Brain Research, 46, **1982**, pp.305-310

[45] Luschei, E.S., Goodwin, G.M.,"*Patterns of Mandibular Movement and Jaw Muscle Activity During Mastication in the Monkey,*" J. Neurophysiol 37, 1974, pp.954-966

[46] Ostry,D.J.,Flanagan,J.R.,"*Human Jaw Movement in Mastication and Speech.*" Archives of Oral Biology, Vol.34, No.9, **1989**, pp.685-693

[47] Wilding,R.J.C.,Lewin,A.,"*A Computer Analysis of Normal Human Masticatory Movements Recorded With a Sirognathograph.*" Archives of Oral Biology, Vol.36, No.1,**1991**, pp.65-75

[48] Mongini, F., Tempia-Valenta, G., Benvegnu, G., "*Computer-based assessment of habitual mastication,*" Journal of Prosthetic Dentistry, 55, 1986, pp.638

[49] Agrawal K.R., Lucas P.W., Bruce I.C.,"*The effects of food fragmentation index on mandibular closing angle in human mastication,*" Arch Oral Biol. **2000** Jul;45(7):577-84

[50] Flavel,S.C.,Nordstrom,M.A.,Miles,T.S.,"*A simple and inexpensive system for monitoring jaw movements in ambulatory humans.*" Journal of Biomechanics **2002**, pp. 573-577

[51] Hannam,A.G., Matthews,B.,Yemm,R.,"*The Unloading Reflex in Masticatory Muscles of Man,*" Archives of Oral Biology 13, 1968, pp.361-364

[52] Miles, T.S., Poliakov, A.V., Nordstrom, M.A., "*Responses of Human Masseter Motor Units to Stretch,*" Journal of Physiology 483, 1995, pp.251-264

[53] Wang, K., Svenson, P., Arendt-Neilsen, L., "*Effect of tonic Muscle Pain on Short Latency Jaw-Stretching Reflexes in Humans,*" Pain 88, 2000, pp.189-197

[54] Leader,J.K.,Boston,J.R.,Debski,R.E.Rudy,T.E.,"*Mandibular Kinematics Represented by a Non-Orthogonal Floating Axis Joint Co-ordinate System.*" Journal of Biomechanics 36, **2003**, pp.275-281

[55] Wagner,A.,Seeman,R.,Schicho,K.,Ewers,R.,Piehslinger,E.,"*A comparative analysis of optical and convenetional axiography for the analysis of temporomandibular joint movements.*", The Journal of Prosthetic Dentistry, November **2003**, pp.503-509

[56] Patient UK, "*Skull (diagram),*" **1997,** http://www.patient.co.uk/showdoc/21692496/Skull

[57] Winter,D.A.,"*Biomechanics and Motor Control of Human Movement,*" 2nd Edition, New York: Wiley **1990**

[58] Howell, D.C., "*Fundamental Statistics for the Behavioral Sciences,*" 4th edition, **1998** http://www.uvm.edu/~dhowell/StatPages/Fundamentals/Glossary.html

[59] Stockburger, D.W., "*Introductory Statistics: Concepts, Models and Applications,*" Correlation **1998**

http://www.psychstat.smsu.edu/introbook/sbk17.html